BULGARIAN CHEMICAL COMMUNICATIONS

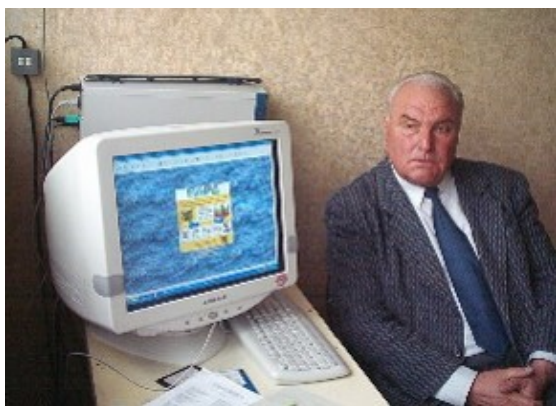# IN MEMORIAM

To the memory of Prof. DSc. Christo Boyanov Boyadjiev (1936-2022)

This year we lost our dear colleague and teacher Prof. Christo Boyanov Boyadjiev. He was born in 1936 in Sliven. He has graduated the High Institute of Chemical Technology-Sofia in 1960. He defended a PhD thesis at the Institute of Chemical Machinery Construction, Moscow in 1968.

He was promoted as Associate Professor at the Institute of General and Inorganic Chemistry-BAS in 1970 and was elected as Full Professor in 1984. During the years of his scientific career, Prof. Boyadjiev has had successful international collaborations with various universities and institutes such as Ben-Gurion University-Beer Sheva, Technion University-Haifa, Tel Aviv University-Tel Aviv, Israel; Russian Academy of Sciences, Institute of Thermophysics. He was also a member of Union of Scientists in Bulgaria, Union of Chemists in Bulgaria, Bulgarian Society of Chemical Engineering, European Federation of Chemical Engineering, member of the Editorial Board of the Russian Journal "University Communications. Energetics", vice-editor-in-chief of the Russian Academy of Sciences Journal "Transactions of Academenergo".

Professor Christo Boyadjiev was the founder of the Laboratory "Process Systems Engineering" in the Institute of Chemical Engineering at Bulgarian Academy of Sciences.

He was the founder and chairman of the Organizing Committee of regular workshops on "Transport Phenomena in Two-Phase Flows".

He has significant contributions in the creation of a theory of the diffusion boundary layer in two-phase systems with moving phase boundaries, which is a basis for modeling mass transfer processes in two-phase industrial systems. He also contributed to the theory of non-linear mass transfer and hydrodynamic stability in systems with intensive interphase mass transfer, which provides a basis for intensification of interphase mass transfer in industrial processes. He has created methods of process systems engineering, allowing modeling and simulation of chemical-process systems, methods for waste gases purification from sulfur dioxide using criterion models for simulation the absorption of sulfur dioxide in a Venturi-type scrubber, as well as methods for parameters identification and for solving incorrect inverse problems.

In recent years, Prof. Christo Boyadjiev has developed a new approach for two-steps modeling of mass transfer in a column apparatus using convective-diffusion type models and average-concentration models, allowing solution of a large range of chemical engineering problems. The created approaches allow the modeling of industrial processes in column apparatuses in the case of simple and complex chemical reactions, physical and chemical absorption in co-current and counter-current apparatuses, physical and chemical adsorption of solid adsorbents, catalytic reactions of a solid catalyst in physical and chemical adsorption. The obtained theoretical results were included in three patents and two utility models, which allow the creation of an absorption-adsorption method and apparatus for waste gases purification from sulfur dioxide.

He was an author and co-author of over 230 papers, published in prestigious international journals, 12 patents registered, of which two have been implemented. Professor Christo Boyadjiev was an author of 9 monographs and 5 book chapters in specialized issues published by Elsevier and Springer.

Prof. Christo Boyadjiev delivered lectures on "Modeling and simulation in chemical engineering" in the University "Prof. Dr. Assen Zlatarov" – Bourgas.

He was also the supervisor of many PhD students who successfully defended their theses and some of them continued their scientific careers in the Institute of Chemical Engineering at the Bulgarian Academy of Sciences.

Professor Chr. Boyadjiev's high professionalism, dedication and broad scientific interests will be remembered and appreciated by his colleagues and friends.

We shall remember Prof. Christo Boyadjiev as a remarkable Bulgarian scientist in the field of chemical engineering and as a best colleague and teacher.

The team of the Institute of Chemical Engineering
Bulgarian Academy of Sciences

Application of response surface methodology for the optimization of copper (II) adsorption in aqueous solution using rambutan peel powder biosorbent

N. L. Wei, S. R. B. Hassan*

Faculty of Bioengineering and Technology, Universiti Malaysia Kelantan, Malaysia
Advance Industrial Biotechnology Cluster, Universiti Malaysia Kelantan, Malaysia

In this study acid-treated rambutan peel was used as a low-cost agricultural waste-derived biosorbent to remove copper (II) from aqueous solution. Central composite design (CCD) of response surface methodology (RSM) was applied to study the optimization of adsorption capacity and removal efficiency through analyzing the parameters (initial copper (II) concentration, pH and biosorbent dosage) by using Design-Expert software. The optimum conditions of adsorption capacity of copper (II) were: biosorbent dosage = 0.05 g, initial copper (II) concentration = 60 mg/L, pH = 5 whereas for removal efficiency they were: biosorbent dosage = 0.1 g, initial copper (II) concentration = 35 mg/L, pH = 5. The highest adsorption capacity and removal efficiency obtained were 25.33 mg/g and 95.24 %, respectively. Pseudo-first and -second order models and intra-particle diffusion model were applied to study adsorption kinetics. The kinetic data fitted well the pseudo-second order model with R^2 of 99.28 %. Characterization of raw and acid-treated rambutan peel biosorbent before and after adsorption was performed with FTIR, SEM and EDS.

Keywords: Adsorption, characterization, biosorbent, copper (II), kinetic studies.

INTRODUCTION

The significant water pollution issue has been identified to threat humans and aquatic animals due to discharging inorganic chemicals without being properly purified. This issue could trigger toxicity to living organisms that accidentally consumed over permitted level. The industrial activities in agricultural field and petroleum effluents discharged massive amounts of effluents containing heavy metals into the drainage water stream which can lead to severe environmental effects and potential human exposure. High contents of heavy metal effluents to the environment can cause contamination to the groundwater and surface water with an increase in biochemical oxygen demand (BOD) and chemical oxygen demand (COD) levels that could disturb living of aquatic animals and diminish the crop yields. Barreto *et al.* [1] stated that the discharging of heavy metal effluents in sedimentation of freshwater credited to the deposition of metal elements that altered chemical configuration of anthropogenic impacts and supplementation of aquatic plants. Lead poisoning may lead to damage of nervous system which can trigger irritability, headache, loss of memory and poor attention spam to humans [2]. Copper is the third most necessary trace element following iron and zinc which functions as a catalyst to speed up heme synthesis and adsorption of iron by human body. Copper is categorized as a metal with high electrical and thermal conductivity. It is also less corrosive and has the properties of alloying and malleability [3]. Copper can be used as a therapeutic mediator which has the advantage to treat Alzheimer's disease and Parkinson's disease when used in the correct approach of treatment [4]. Therefore, heavy metals like copper are essential in development and redox chemistry in the living organisms in acceptable quantities which are non-toxic. Excessive intake of copper by the human body can trigger Wilson's disease [5]. It is an uncommon autosomal recessive disorder which occasions in toxicity to liver and brain damage. Drinking water that is obtained from contaminated water source is the major reason for copper toxicity in the human body. Moreover, the serum copper absorption was scaled up to nearly 1.5 mg/L for a health-giving person [3].

Environmental pollution regarding the discharging of toxic heavy metals from industrial effluents to the environment has been greatly concerned by the public. Hence, effective actions should be taken to guarantee the prospect of mankind protection. Ahmad [6] stated that all metals have the properties of bio-availability and solubility at low pH, which are more critical in acidic environment. Heavy metals like chromium, lead and mercury have carried toxicity and harmful effects to the living organisms when transmitted into the environment.

Copper (II) composites are widely applied in various commercial activities, for instance the leather tanning and textile dyeing processes in the

---

* To whom all correspondence should be sent:
E-mail: roshayu.h@umk.edu.my

industry. Copper (II) can act as a fundamental nutrient for various living organisms in regulated amounts. High level of copper (II) contents can lead to poisonous and mutagenic effects. Moreover, excessive consumption of lead can cause kidney damage which affects the effectiveness of kidney and leads to renal failure in human body. The highest acceptable toxicity of inorganic lead is identified to scale from 0.04 to 0.198 mg/L depending on the different conditions [7]. Even though there are many techniques for the removal of heavy metals, they are mostly still in laboratory scale and only few are successfully applied to the industrial level. Therefore, effective methods are required to preserve the aquatic environment from pollution of heavy metals. The adsorption using wastes generated from agricultural and food industry can efficiently remove heavy metal ions as the heavy metals will attach to the surface of the biological materials. Biological resources with high metal binding ability are beneficial in adsorption process. The significance of bio-waste products in removing heavy metals ions from the wastewater is essential.

A biosorbent is a natural resource that can be used to eliminate toxic heavy metals from wastewater sources. A cost-effective biosorbent has the advantages of needing little processing procedures and is originally obtained from wastes that are beneficial in reducing environment pollution problems. Therefore, it is essential to study on new sources of bio-sorbents to remove heavy metals in industrial effluents. The rambutan peels have been used to effectively remove malachite green dyes in the form of activated carbon. There still not many studies on the rambutan peels as a biosorbent to remove heavy metals. The previous research study only investigated the removal of malachite green dyes using activated carbon from rambutan peels [8, 9].

MATERIALS AND METHOD

Biosorbent

The collected raw rambutan (*Nephelium lappaceum*) peel samples were rinsed with water, air-dried, cut into smaller size and acid-treated with 0.1N sulfuric acid. The acid-treated sample was dried, grinded and sieved. The raw and acid-treated rambutan peel powder samples were kept in separated zip bags.

Experimental design

Central composite design (CCD) of the response surface methodology (RSM) was used for the experimental design. Table 1 shows the experimental runs generated from CCD to study the

adsorption of copper (II) by the biosorbent. The 'low' and 'high' in the table indicates the lower limit and higher limit of tested parameters, respectively. The pH, initial copper (II) concentration and biosorbent dosage were designed as the variables A, B, and C, respectively. The ranges used were taken after preliminary testing carried out for each variable. The 20 sets of experimental runs which were designed and generated from CCD according to Table 2 were used to carry out the adsorption studies to determine the removal of copper (II) by the biosorbent. The removal percentage and adsorption capacity of copper (II) were calculated using eq. (1) and eq. (2), respectively, and Design-Expert software to obtain the optimum conditions for removal of copper (II).

Table 1. Experimental runs for adsorption studies.

Variables	Units	Low (-1)	High (+1)
A: X_1		2	8
B: X_2	mg/L	10	60
C: X_3	g	0.05	0.15

Table 2. Experimental design for adsorption studies using CCD.

No.	A	B (mg/L)	C (g)
1	8	10	0.05
2	8	10	0.15
3	2	10	0.05
4	5	10	0.1
5	2	10	0.15
6	5	35	0.15
7	5	35	0.1
8	5	35	0.05
9	2	35	0.1
10	5	35	0.1
11	8	35	0.1
12	5	35	0.1
13	5	35	0.1
14	5	35	0.1
15	5	35	0.1
16	5	60	0.1
17	2	60	0.05
18	8	60	0.15
19	8	60	0.05
20	2	60	0.15

Optimization of adsorption

The acid-treated rambutan peel powder was used as biosorbent to optimize the adsorption of copper (II). Constant were kept the agitation speed (150 rpm), temperature (30 °C), volume of copper (II) solution (100 ml) and contact time (45 minutes). The effects of pH, initial copper (II) concentration and biosorbent dosage on removal percentage and adsorption capacity of copper (II) were studied. 20 runs of adsorption studies were carried out according to Table 2 which was generated using the Design

Expert software. The absorbance readings were obtained by UV-Vis spectrophotometry at 580 nm. The reacted mixture from each set of adsorption studies was filtered using a filter paper to obtain a clear solution. Three replicates were obtained from each of the 20 sets of adsorption studies in order to increase the accuracy of the results. The concentration of copper (II) was controlled by means of a standard calibration curve. The adsorption capacity at equilibrium, q_e, was calculated using eq. (1):

$$q_e \left(\frac{mg}{g}\right) = \left[\frac{C_i - C_e}{m}\right] V \tag{1}$$

where C_i is the initial concentration of copper (II) in aqueous solution, C_e is the final concentration of copper (II) in aqueous solution (mg/L), m is the mass of biosorbent (g), and V is the volume of solution (L). The removal percentage efficiency was calculated using eq. (2):

$$R(\%) = \left[\frac{C_i - C_e}{C_i}\right] \times 100 \tag{2}$$

where C_i is the initial concentration of copper (II) in aqueous solution, C_e is the final concentration of copper (II) in aqueous solution (mg/L).

Kinetic studies

The mathematical models used in this study for describing the kinetics of adsorption were determined by using pseudo-first and -second order kinetics, as well as intra-particle diffusion model. The kinetic studies are of significance to study the behavior of the adsorption to optimizing the adsorption properties. The pseudo- first and -second order models and intra-particle diffusion model were applied using eq. (3), eq. (4) and eq. (5), respectively. Eq. (3) shows the linearized pseudo-first-order model:

$$\log(qe - qt) = \frac{k_1}{2.303} t \tag{3}$$

where, q_e is the amount of biosorbent at equilibrium (mg/g), q_t is the amount of biosorbent at equilibrium (min) and k_1 is the rate constant (1/min). The pseudo-second order model was applied using eq. (4). Eq. (4) shows the linearized form of pseudo-second order model:

$$\frac{t}{q_t} = \frac{1}{k_2 q_e^2} + \frac{1}{q_e} t \tag{4}$$

where, q_e is the amount of biosorbent at equilibrium (mg/g), q_t is the amount of biosorbent at equilibrium (min) and k_2 is the rate constant (mg/g). The intra-particle diffusion model was applied using eq. (5). Eq. (5) shows the linearized form of the intra-particle diffusion model:

$$Q_t = K_{id} t^{0.5} + C \tag{5}$$

where, Q_t is the amount absorbed at time t and $t^{0.5}$ is the square root of the time, C is the intercept and K_{id} (mg g^{-1} min$^{-0.5}$) is the rate constant of intra-particle diffusion.

Analysis and characterization

The characterization of rambutan peel powder was carried out using Fourier transform infrared spectroscopy (FTIR). scanning electron microscopy (SEM) and energy dispersive X-ray spectroscopy (EDS) which were used to study the major functional groups, composition and topography of biosorbent and semi-quantitative elemental materials on specific sites within the observed area of rambutan peel biosorbent.

RESULTS AND DISCUSSION

Characterization of rambutan peel biosorbent

Surface morphology and elemental composition analysis. From Fig 1(A) it is seen that acid-treated rambutan peel biosorbent has obtained additional pores on the surface compared to raw rambutan peel biosorbent, though it did not demonstrate a consistent structure of biosorbent surface. The surface of acid-treated rambutan peel biosorbent after adsorption displayed more porous structure compared to before adsorption. After acid treatment, the rambutan peel biosorbent displayed to be more heterogeneous and multiplex compared to raw rambutan peel biosorbent with a relatively smooth surface.
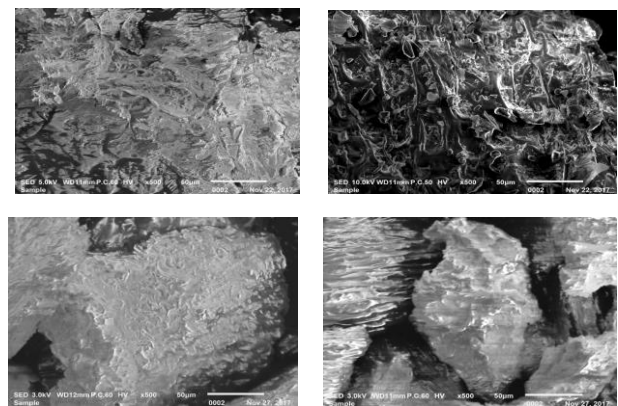
Figure 1. SEM image of acid-treated rambutan peel powder before adsorption (a), acid-treated rambutan peel powder after adsorption (b), raw rambutan peel powder before adsorption (c), and raw rambutan peel powder after adsorption (d).

From the results of SEM analysis it followed that acid-modified biosorbent after adsorption was composed of hollow and favorable porous carbon fibers encircled with masses of carbon composites

[10]. However, the raw rambutan peel biosorbent did not display an obvious metamorphosis before and after adsorption process. Moreover, it can also be monitored that adsorption is a surface spectacle. This is due to the fact that smaller biosorbent particle sizes provide a moderately greater and additionally available surface area with additional pores acquired [11]. In consequence, a better adsorption mechanism can take place at equilibrium. EDS analysis was carried out to determine the chemical composition available on the surface of rambutan peel biosorbent. Both acid-treated and raw rambutan peel biosorbent displayed a low distinct peak of copper (II) loaded before adsorption (see Fig. 2 (A) and (B)), whereas the spectrum has clearly displayed incidence of copper (II) present for both raw and acid-treated rambutan peel biosorbent surfaces after adsorption (Fig. 2 (C) and (D)). The peak of copper appeared to be greater after the adsorption process as compared to raw rambutan peel biosorbent before adsorption which indicates that an adsorption process of copper (II) took place at the surface of rambutan peel biosorbent. Moreover, the increased peak of copper (II) in acid-treated rambutan peel biosorbent after adsorption in Fig. 2 (D) describes the chemical composition appeared on the surface of acid-treated rambutan peel biosorbent. As estimated, EDX spectra proved that the carbon content has highest percentage in the existence of diatoms. Nonetheless, oxygen, calcium, phosphorus and silicon are also present in each spectrum. This may be due to the precipitated compounds present, dissolved substances and salts present during the adsorption process of copper (II) [12]

Fourier transform infrared spectroscopy (FTIR) analysis. FTIR spectrum clarifies the functional groups available in the adsorption of copper (II) by rambutan peel biosorbent. The model of adsorption of copper (II) is due to the presence of active functional groups. Presence of distinct peaks at 1317.00 cm^{-1} and 1613.14 cm^{-1} in Fig. 3 (A) specified the presence of C-O stretch in carboxylic acids and N-H bends in amine groups for the adsorption process. The existence of C-C triple bond of alkynes at the peak 2296.03 cm^{-1} clearly specifies the contribution of alkynes in adsorption of copper (II). Thus, it is obvious that carboxylic acids, amines and alkynes are involved in the adsorption of copper (II).

The multiplex spectra of acid-treated rambutan peel biosorbent in Fig. 3 (B) after adsorption display some strong adsorption bands. The broad peak at 1017.74 cm^{-1} represents the existence of C-F stretch of C-bonded in alkyl halides. The alteration of this peak after adsorption points at the contribution of C-

F groups from alkyl halides. The disappearance of the peak at 1316.42 cm^{-1} after adsorption (see Fig. 3 (B)) is a proof of the contribution of C-H stretch in alkene group.
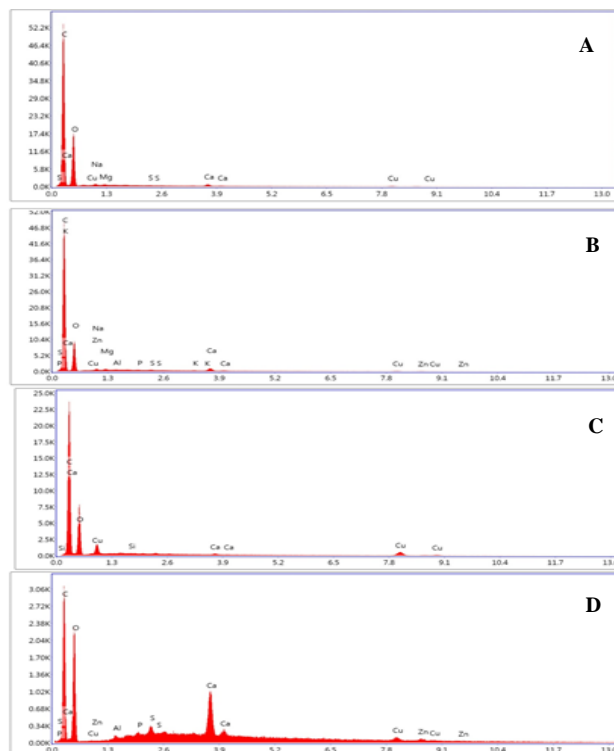
Figure 2. EDS image of acid-treated rambutan peel powder before adsorption (a), raw rambutan peel powder before adsorption (b), raw rambutan peel powder after adsorption (c) and acid-treated rambutan peel powder after adsorption (d).
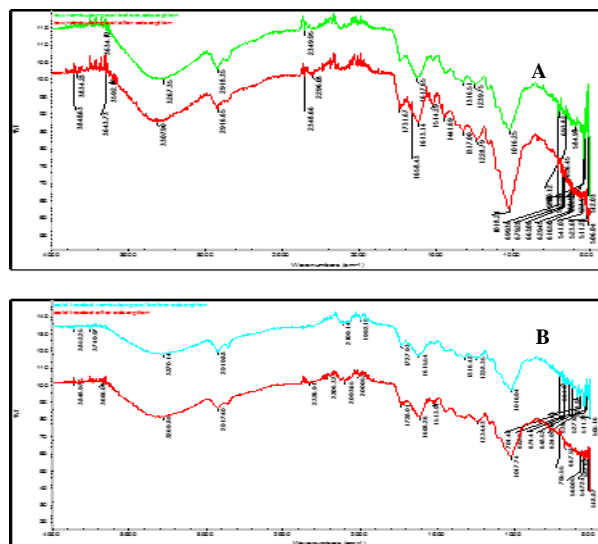
Figure 3. FTIR spectra for raw rambutan peel powder before and after adsorption (a) and acid-treated rambutan peel powder before and after adsorption (b)

The peak at 3749.97 cm^{-1} corresponds to acetylenic C–H stretch of alkyne group and the decline of the peak to 3666.05 cm^{-1} after adsorption

means that the alkyne group has affected intensely the adsorption of copper (II). The peak at 2206.03 cm^{-1} specifies the existence of C-C triple bonding stretch in alkyne groups which also affected the adsorption of copper (II). In Fig. 3 (B), a definite peak at 1016.94 cm^{-1} before adsorption relates to S=O stretch in sulfoxide group and its decline after adsorption of copper (II) specifies the contribution of particular groups in adsorption process [13]. The peak at 683.63 cm^{-1} is a suggestion for contribution of C-Cl stretch in alkyl halide groups for adsorption of copper (II). Consequently, the major functional groups of acid-treated rambutan peel biosorbent that affected the adsorption of copper (II) are found to be alkyl halides, alkenes, carboxylic acids, alkynes and sulfoxide groups.

Response surface methodology

Removal efficiency. Response surface methodology creates an empirical model articulated through a second-order polynomial equation in terms of the coded factors. This relationship reflects the correlation between variables concerning the response. The coefficient with one factor indicates the consequence of specific variable, therefore the coefficient with two factors together with the second-order term will affect the correlation between these two factors, as well as the quadratic effect, correspondingly.

Through pertaining multiple regression evaluation on the design matrix and response, the equation of the removal percentages of copper (II) in terms of coded factors is as shown below:

Removal percentages = 90.52 – 3.06A – 2.19B + 0.75C – 2.5AB – 0.97AC + 0.56BC – 1.97A^2 + 1.32B^2 – 9.16C^2   (6)

where, A is the initial copper (II) concentration, B is the biosorbent dosage and C is the pH.

A plot of observed percentage probability of the residuals to the predicted probability is represented in Fig. 4. The observed percentage probability of the residuals represents approximately no significant interruption of the expectations underlying the studies. It authorizes the normality expectations composed in advance, as well as the independence of the residuals through presenting a fitting normal distribution. There is an adequate relationship between the observed probability and the predicted probability of the copper (II) removal percentage as shown in Fig. 4. The points assembled around the sloping line on the graph represents a good fit of the quadratic model, subsequently the deviation among the observed and predicted values was lower [14, 15].

The outcomes of the second-order response

surface model in the formula of investigation of variance (ANOVA) are presented in Table 3. The statistical significance of the model equation was evaluated by the F-test ANOVA. The significance of each coefficient was regulated by F-values and P-values. It is seen from Table 3 that the coefficients for the main and square effects are highly significant (P < 0.0001) in comparison with interaction effects. Table 3 displays ANOVA for the response surface quadratic model.
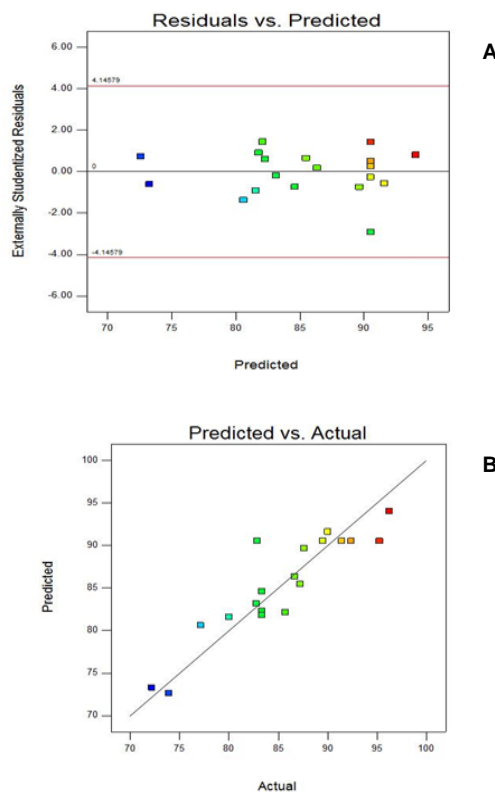
Figure 4. Plot of residuals to predicted probability (A) and plot of actual probability to predicted probability (B)

Table 3. Regression analysis using central composite design

| Factor	Coefficient estimation	df	Stand. error	F-value	P-value
Intercept	2.99	1	0 .87	11.99	0.0003
A	6.49	1	0.80	65.33	<0.0001
B	-2.69	1	0.80	11.22	0.0074
C	0.01	1	0.80	0.00	0.9891
AB	-2.39	1	0.90	7.08	0.0238
AC	0.61	1	0.90	0.46	0.5115
BC	-0.28	1	0.90	0.10	0.7633
A^2	1.85	1	1.53	1.46	0.2550
B^2	0.29	1	1.53	0.04	0.8521
C^2	4.01	1	1.53	6.88	0.0255

The F-value (65.33) for factor A with a low probability value (P < 0.0001) demonstrates a high

significance for the regression model. The goodness of the fit of the model was also checked *via* the multiple correlation coefficient (R^2). In this study, the value of the multiple correlation coefficient was 0.8313, which means that this regression is statistically important and 16.87% of the complete variations is not described *via* the quadratic model. The value of predicted multiple correlation coefficient (pred. R^2 = 0.3733) is not equally adjacent to the compact in conjunction with the value of the adjusted multiple correlation coefficient (adj. R^2 = 0.6794). Simultaneously, a comparatively inferior value of the coefficient of variance (CV = 4.32%) specifies an improved accuracy and dependability of the tests conducted.

Effect of pH and initial copper (II) concentration. An upsurge of removal efficiency of copper (II) through increasing the initial copper (II) concentration is a consequence of the enhancement in the impelling cause of concentration gradient, moderately increasing in the initial copper (II) concentration. As the initial copper (II) concentration is greater, the active sites of the rambutan peel biosorbent would be encircled with high amount of copper (II) ions, hence the adsorption process can be conducted more frequently and adequately to reach the optimization of the adsorption process. Consequently, the gradual increae of the pH value and initial copper (II) concentration up to the optimized conditions will effectively enhance the adsorption process. Moreover, some researchers have also studied the effect of pH with initial copper (II) concentration for adsorption of heavy metals using different kinds of biosorbent and the results agreed with this study. Cekim *et al.* [16] stated an increased adsorption efficiency (qe) from synthetic water through tobacco leaf absorbent on increasing the initial copper (II) concentration with the reading of greatest qe (10.66 mg/g) with initial copper (II) concentration of 50 mg/L. In a study of the adsorption of copper using *tamarindus indica* fruit nut testa as biosorbent, maximum adsorption level was achieved at pH 5 for copper and the effect of pH can be interpreted on the basis of the structure of biosorbent and speciation of copper [17].

Effect of biosorbent dosage and pH. The effect of pH and biosorbent dosage on the removal efficiency of the copper (II) is displayed in Fig. 6. It was found that the removal efficiency of copper (II) decreased with increasing biosorbent dosage from 0.05 to 0.15 g and its optimum value was recorded as 0.1 g. The actual factor of initial concentration recorded was 35 mg/L. In order to explain based on the experimental researching, increasing biosorbent dosage can be

194

recognized as a contribution to the increasing of the surface area for the adsorption of copper (II), as well as the accessibility of additional adsorption sites. Nonetheless, the removal efficiency will decrease with the increasing of biosorbent dosage. This is due to the reason that the initial factor describing the situation is that adsorption sites stay unsaturated throughout the adsorption process and the amount of active sites accessible for adsorption increased through the enhancing of biosorbent dosage.
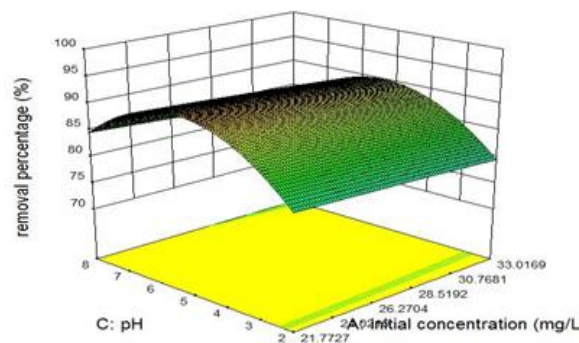
Figure 5. Response surface plot of the effect of pH and initial copper (II) concentration.
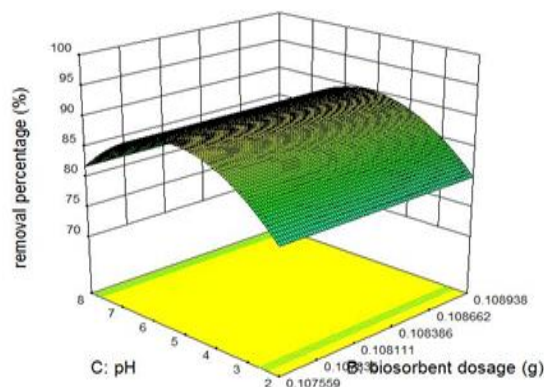
Figure 6. Response surface plot of the effect of biosorbent dosage and pH

Validation of regression model equation

For the development of a regression model equation, three variables were considered as independent process variables. Their discrete and interactive properties on the removal efficiency of copper (II) as a response were studied using central composite design. A quadratic polynomial model was applied in order to regulate the correlation between the process factors and its corresponding response. No transformation was needed and the quadratic model was selected to fit the data as

recommended by the Design Expert 10.0.7 software. The expedient alternative of central composite design is the face-positioned design which is a three-level design for response surface studies to be carried out. It will map out the shapes of quadratic surface and show results in optimization of the variables to the removal percentages. This design is located at axial points of the centers of cube faces as shown in Fig. 7 which has k= 3 factors. The variation of central composite design was applied due to the requirement of three levels of factors.
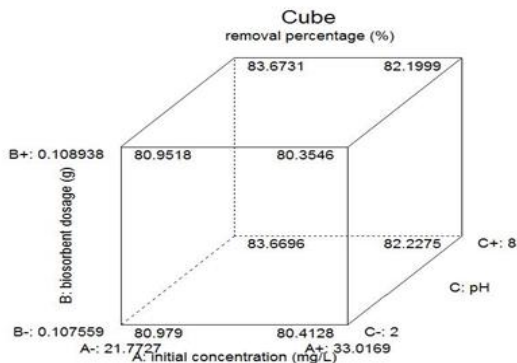
Figure 7. Face-centred central composite design for k=3.

Absorption capacity

Effect of pH and initial copper (II) concentration. The effects of pH and initial copper (II) concentration on the adsorption capacity by acidic treated rambutan peel biosorbent can be observed in Fig. 8. The adsorption capacity of copper (II) increased with the increase in initial copper (II) concentration of 10 to 60 mg/L together with pH ranging from 2 to 8. The highest adsorption capacity of copper (II) was determined to be 24 mg/g. Hence, the excessive pH condition will reduce the adsorption capacity of copper (II). When the initial copper (II) concentration increases, there will be an increase in the adsorption capacity due to the driving force of the copper (II) concentration gradient. As the same situation, the more copper (II) ions present in the adsorption, the active sites of biosorbent would be encircled with high concentration of copper (II). In consequence, the adsorption capacity would be more efficient [18]. The adsorption capacity increased when the pH condition increased. The adsorption capacity achieved maximum at greater pH values and decreased as the pH condition was further excessive. The pH condition will equally affect surface binding sites and chemical properties on the biosorbents [19].
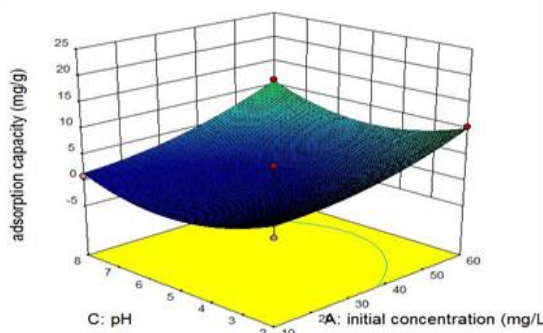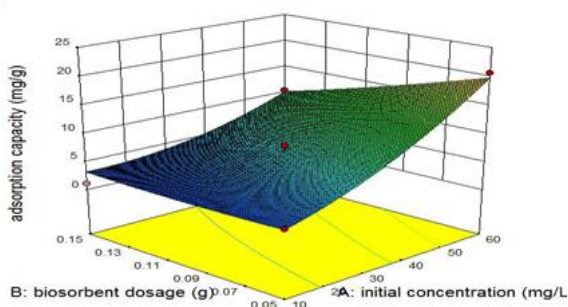

Figure 8. Response surface plot of effect of pH and initial copper (II) concentration.
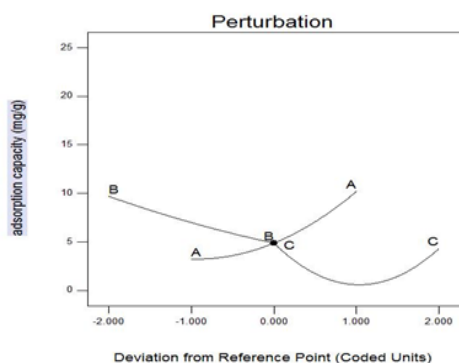
Effect of initial copper (II) concentration and biosorbent dosage. The effects of initial copper (II) concentration and biosorbent dosage on the adsorption capacity by acidic treated rambutan peels biosorbent can be observed in Fig. 9. The adsorption capacity of copper (II) increased with the increased of initial copper (II) concentration of 10 to 60 mg/L together with biosorbent dosage ranged from 0.05 to 0.15 g. The highest adsorption capacity of copper (II) was determined to be 24 mg/g. With the lower biosorbent dosage and higher initial copper (II) concentration, there is a higher adsorption capacity recorded. This is due to the higher ratio of biosorbent surface binding sites to the copper (II) concentration presented during the adsorption mechanism. From Fig. 9, the biosorbent dosage increased with the decreasing of adsorption capacity of copper (II) per unit mass of biosorbent (q_e) [20]. The increasing of biosorbent surface active binding sites and accessibility of more adsorption active sites are interdepended to the increasing in biosorbent dosage in the study. Yet the adsorption capacity (q_e) will decrease with increasing of biosorbent dosage, as seen from Fig. 9. As a result of the situation, the adsorption active binding sites of biosorbent will be maintained unsaturated during the adsorption mechanisms although the quantity of active sites obtainable for adsorption increased with increased biosorbent dosage.

Perturbation plot

Perturbation plot illustrations of the function of particular actual factors countered as the level of particular factor altered while the other factors were stable at optimum conditions. The steeper slope in the perturbation plot represents the sensitivity of response factors.

Figure 9. Response surface plot of the effect of initial copper (II) concentration and biosorbent dosage.

Figure 10. Perturbation plot of the adsorption capacity of copper (II) with actual factors, A: initial copper (II) concentration, B: biosorbent dosage and C: pH.

Therefore, perturbation plot of adsorption capacity of copper (II) was applied to evaluate the consequences of respective factors on the adsorption capacity of copper (II). From Fig. 10, the biosorbent dosage decreases while the initial copper (II) concentration and pH values increases as the adsorption capacity of copper (II) was increased. Hence, it indicated that factors such as initial copper (II) concentration and pH would significantly impact on the adsorption capacity of copper (II). Through analyzing the slope of each factor from Fig 10, initial copper (II) concentration (A) and biosorbent dosage (B) are the major influential factors for the adsorption capacity of copper (II) as compared to pH (C). The adsorption capacities obtained for factor A and B were comparatively higher than for factor C. The relations of these factors have important effect on the responses [21].

Kinetics studies on adsorption

Adsorption process through biosorbent can be regulated with various types of mechanisms, for instance chemical reactions, diffusion control, and particle diffusion. Several adsorption models for

196

adsorption were utilized to interpret the experimental data obtained. Pseudo-first and -second order reaction kinetic models and intra-particle diffusion model were considered and fitted with the experimental data obtained. Figs. 11 and 12 display the plots of pseudo-first and -second order kinetic models for the adsorption of copper (II) through rambutan peel biosorbent, respectively. Experimental and hypothetically analyzed adsorption capacities at equilibrium (q_e) values and coefficients associated to kinetic plots are listed in Table 4. It can be observed from Table 4 that the linear correlation coefficients for pseudo-first order model are not well fitted with R^2 of 92.43 % compared to pseudo-second order model with R^2 of 99.28. These findings recommend that adsorption of copper (II) by rambutan peel biosorbent is not fitting to pseudo first-order reaction with lower R^2 value. It is apparent from the findings for correlation coefficients for pseudo-second order model that the adsorption of copper (II) is comparatively high with R^2 value of 0.9928 and the experimental and hypothetical adsorption capacities values are fitted well. Hence, the adsorption of copper (II) by rambutan peel biosorbent obeys the pseudo-second order model with R^2 of 99.28 %.
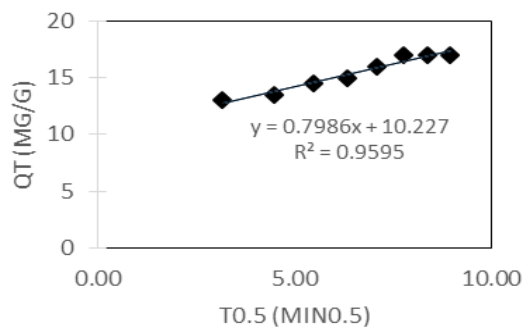
Furthermore, the intra-particle diffusion model predicts that overall adsorption rate is regulated by the rate of copper (II) diffusion within biosorbent pores [22]. It also determines the rate-limiting phase in adsorption of copper (II) in this study. Fig. 13 displays that adsorption of copper (II) is described by a linear graph which indicates that there is better agreement in the adsorption process. Adsorption mechanism is a multi-step progression as it develops two zones. In the first zone there is immediate adsorption whereas the second zone is steady adsorption phase [23]. The immediate adsorption is also known as external adsorption process which occurs at the external surface of biosorbent. The R^2 value of intra-particle diffusion model on adsorption of copper (II) was determined to be 95.95 % which means that 4.05 % of variation was not described by this model.
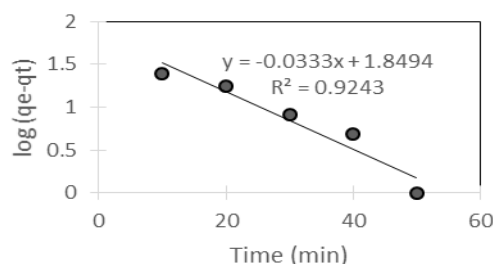
Figure 11. Pseudo-first order model plot for adsorption of copper (II) by rambutan peel biosorbent.
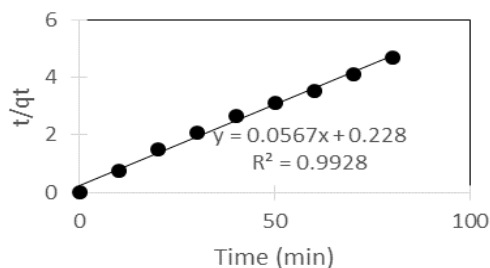
Figure 12. Pseudo-second order model plot for adsorption of copper (II) by rambutan peel biosorbent

Figure 13. Intra-particle diffusion model plot for adsorption of copper (II) by rambutan peel biosorbent.

Table 4. Adsorption kinetic model rate constants of copper (II) removal by rambutan peel biosorbent

Kinetics	Pseudo-first order model	Pseudo-second order model	Intra-particle diffusion model
Q_e (mg/g)	70.697	17.637	
K (1/min)	0.0767	0.0141	
R^2	0.9243	0.9928	0.9595
Y-intercept			10.227
K_{id}			0.7986

CONCLUSION

The current study has determined that acid-treated rambutan peel biosorbent has adsorption capability towards copper (II) in aqueous solution. The parameters in terms of initial copper (II) concentration, biosorbent dosage and pH affected the removal efficiency of copper (II) from aqueous solution. From the 3D plots generated by RSM using Design-Expert software, it can be concluded that removal efficiency in terms of percentage increased as initial copper (II) concentration and pH increased, whereas it decreased as biosorbent dosage increased. The optimum condition for acid-treated rambutan peel biosorbent in adsorption of copper (II) was determined to be 35 mg/L initial copper (II) concentration, pH 5 and 0.1 g of biosorbent dosage that gives removal efficiency as high as 95.24 %. Optimal adsorption capacity of copper (II) of 25.33 mg/g was obtained with RSM using Design-Expert software. Adsorption capacity of copper (II) increased along with increased initial copper (II) concentration and it decreased as biosorbent dosage and pH increased.

Pseudo-first and -second order model and intra-particle diffusion model were applied to study the adsorption kinetics of copper (II). The kinetic study models on adsorption of copper (II) were verified through the values obtained for determination (R^2). Kinetic study on adsorption of copper (II) was performed to follow pseudo-second order model with R^2 of 99.28 % as compared to pseudo-first order model with R^2 of 92.43 % and intra-particle diffusion model with R^2 of 95.95 %. The value of R^2 with 99.28 % represents that 0.72 % of variation was not described by the pseudo-second order model. The consequence of the study indicated that acid-treated rambutan peel biosorbent is a potential biosorbent for the adsorption of copper (II) in aqueous solution. The kinetic study of adsorption of copper (II) described that both adsorption studies and intra-particle diffusion methods were applicable in adsorption of copper (II) using acid-treated rambutan peel biosorbent.

REFERENCES

1. W. J. Barreto, S. R. G. Barreto, I. S. Scarminio, F. Inoue, *Analytical Letters*, **43(5)**, 814 (2010), https://doi.org/10.1080/00032710903486278
2. F. Fernández-luqueño, F. López-Valdez, P. Gamero-Melo, S. Luna-Suarez, E. N. Aguilera-González et al., *African Journal of Environmental Science and Technology*, **7**, 567 (2013), https://doi.org/10.5897/AJEST12.197
3. J. R. Turnlund, *Am. J. Clin. Nutr.*, **67**, 960 (1998).
4. F. Harris, L. Pierpoint, *Medicinal Research Reviews*, **29(6)**, 1292 (2012), https://doi.org/10.1002/med
5. P. G. Georgopoulos, A. Roy, J. Yonone-Lioy, R. Opiekun, P. J. Lioy, *Journal of Toxicology and Environmental Health: Critical Reviews*, **4(4)**, 341 (2001). https://doi.org/10.1080/15287390500196230
6. M. A. Ahmad, R. Alrozi, *Chemical Engineering Journal*, **168(1)**, 280 (2011), https://doi.org/10.1016/j.cej.2011.01.005
7. M. R. Tayab, Environmental Impact of Heavy Metal Pollution in Natural Aquatic Systems. A Thesis Submitted for the Degree of Doctor of Philosophy

(Environmental Pollution Science), Brunel, The University of West London, 1991.

8. M. A. Ahmad, R. Alrozi, *Chemical Engineering Journal*, **171(2),** 510 (2011), https://doi.org/ 10.1016/j.cej.2011.04.018

9. P. Phuengphai, Th. Singjanusong, N. Kheangkhun, A. Wattanakornsiri, *Water Science and Engineering*, **14** (4), 286 (2021).

10. S. T. Ramesh, N. Rameshbabu, R. Gandhimathi, P. V. Nidheesh, M. Srikanth Kumar, *Applied Water Science*, **2(3),** 187 (2012), https://doi.org/ 10.1007/s13201-012-0036-3

11. V. O. Njoku, K. Y. Foo, M. Asif, B. H. Hameed, C*hemical Engineering Journal*, **250,** 198 (2014), https://doi.org/10.1016/j.cej.2014.03.115

12. H. J. Park, S. W. Jeong, J. K. Yang, B. G. Kim, S. M. Lee, *J. Environ. Sci.* (China), **19(12),** 1436 (2007), https://doi.org/10.1016/S1001-0742(07)60234-4

13. B. Kiran, N. Rani, A. Kaushik, *International Journal of Phytoremediation*, **6514**, 1067 (2016), https://doi.org/10.1080/15226514.2016.1183577

14. K. Yetilmezsoy, S. Demirel, R. J. Vanderbei, *Journal of Hazardous Materials*, **171(1–3),** 551 (2009), https://doi.org/10.1016/j.jhazmat.2009.06.035

15. L. Brahmi, F. Kaouah, S. Boumaza et al., *Applied Water Science,* **9**, 171 (2019), https://doi.org/ 10.1007/ s13201-019-1053-2

16. M. Çekim, S. Yildiz, T. Dere, *Journal of Environmental Engineering and Landscape Management*, **23(3),** 172 (2015), https://doi.org/ 10.3846/16486897.2015.1050398.

17. M. Farhan, A. M. Salem, N. H. Al-Dujaili, M. Awwad, *American Journal of Environmental Engineering*, **2(6),** 188 (2012), https://doi.org/ 10.5923/j.ajee.20120206.07

18. F. Ghorbani, H. Younesi, S. M. Ghasempouri, A. A. Zinatizadeh, M. Amini, A. Daneshi, *Chemical Engineering Journal,* **145(2),** 267 (2008), https://doi.org/10.1016/j.cej.2008.04.028

19. V. O. Njoku, K. Y. Foo, M. Asif, B. H. Hameed, *Chemical Engineering Journal*, **250**, 198 (2014), https://doi.org/10.1016/j.cej.2014.03.115

20. S. Rangabhashiyam, M. S. G. Nandagopal, E. Nakkeeran, R. Keerthi, *Desalination and Water Treatment,* **3994**, 1 (2016), https://doi.org/10.1080/ 19443994.2016.1163514

21. R. O. Cristóvão, A. P. M. Tavares, J. M. Loureiro, R. A. R. Boaventura, E. A. Macedo, *Environmental Technology,* **29(12),** 1357 (2008), https://doi.org/ 10.1080/ 09593330802379615

22. F. C. Wu, R. L. Tseng, R. S. Juang, *Chemical Engineering Journal*, **153**(1–3), 1 (2009), https://doi.org/10.1016/j.cej.2009.04.042

23. Y. Bulut, Z. Tez, *Journal of Environmental Sciences* (China), **19**(2), 160 (2007), https://doi.org/10.1016/ S1001-0742(07)60026-6.

Modeling pore blocking of nanofiltration and reverse osmosis membranes during NaCl removal

M. Bchiti[1], M. Igouzal[2*], S. El-Ghzizel[1], A. El Midaoui[1]

[1] Laboratory of Advanced Materials and Process Engineering, Department of Chemistry, Faculty of Science, Ibn Tofail University, BP1246 Kenitra, Morocco
[2] Laboratory of Electronic Systems, Information Processing, Mechanics and Energy,Department of Physics, Faculty of Science, Ibn Tofail University, BP1246 Kenitra, Morocco

Moroccan surface water and groundwater mark an increase of salt concentrations in the authorized drinking water levels. Membrane processes are a helpful technology to minimize these concentrations and to achieve high water quality in the distribution systems. However, the performance of a given membrane is found to be degraded due to membrane fouling and hence it results into a significant decline in the permeate flux. Membrane fouling is mainly associated with the deposition of solute molecules on the membrane surface. Therefore, it is necessary to interpret the fouling mechanism in order to predict the permeate flux evolution. In this paper, the permeate flux decline with time through two nanofiltration (NF) membranes (NF90, NF270) and one reverse osmosis (RO) membrane (BW30LE4040) was studied at a laboratory pilot scale using synthetic water doped with NaCl. Then, the mechanism of membrane fouling was studied through describing four pore-blocking models such as Complete Pore Blocking, Standard Pore Blocking, Intermediate Pore Blocking and Cake Formation. Parameters of these models were evaluated using a mathematical optimization procedure. The accuracy of the fitted model was judged using thestatistical parameters: regression coefficient, root mean square error (RMSE), normalized root mean square error (NRMSE) and Nash-Sutcliffe efficiency (NSE). Results show that the Complete Pore Blocking Model was the best representation of pore blocking and permeate flux decline of RO and NF membranes in filtration operations.

Keywords: Nanofiltration, Reverse osmosis, Fouling, Permeate flux, Pore blocking model.

INTRODUCTION

Morocco is enduring water shortage and a wide variation of rainfalls which will worsen over the next few years. The concentration of inhabitants and consequently the industrial and agricultural activities along the coastal zone have led to an increase in drinking water demand along this area. Seawater and groundwater desalination can provide a solution to this problem. Hence, many desalination plants were built using RO /NF membranes in water applications.

NF and RO are technologies being increasingly employed to enhance the quality of purified water, increase the productivity of existing plants, and design smaller, yet more effective purification processes.

Choosing the most appropriate membranes for a given water treatment project is decisive [1-4]. Membrane performances must be studied first in a pilot scale, especially for situations where process uncertainties are potentially high in term of membranes performance and total operation cost [5-7]. Unfortunately, a barrier to a breakthrough of the technology is the increased operational cost due to fouling and membrane replacement. Simulation studies with rigorous process models are a powerful tool to increase the understanding of the process and its decisive characteristics in order to design optimal processes and efficient operational strategies. The membrane fouling is affected by several factors, e.g., pore blocking and/or pore constriction, cake formation, solute adsorption, and concentration polarization [8-11]. Initially, foulants smaller than the pore size of membrane deposit or adsorb onto the pore walls, thereby leading to pore constriction. This induces a significant reduction in the cross-sectional area available to the filtrate flow. In contrast, larger foulants deposit or adsorb onto the pore entrances, resulting in a marked increase in the filtrate flow resistance. In either case, pore constriction and pore plugging are followed by the formation of a filter cake accumulating on the membrane surface, thus severely increasing the filtration resistance. Therefore, it is essential to elucidate the underlying mechanism controlling the membrane fouling such as pore constriction, pore plugging, and cake formation during the course of membrane filtration.

Simulation studies with rigorous process models are a powerful tool to increasethe understanding of the process and its decisive characteristics in order to design optimal processes

*To whom all correspondence should be sent:
E-mail: mohammed.igouzal@uit.ac.ma

and efficient operational strategies.

Different models have been proposed in the literature to explain the flux decline. Prominent amongst these are the Standard Blocking Model, Intermediate Blocking Model, Cake Formation Model and Complete Blocking Model [12]. In the Standard Blocking Model, particles get accumulated inside the membrane on the pore walls and the resulting constriction of pores reduces the membrane's permeability. Intermediate Blocking Model assumes that a portion of particles seal some of the pores while the rest accumulate on the top of the deposited particles. The Complete Blocking Model isbased on the premise that the particles are larger than the pore size of the membrane and this results in the particles sealing off the membrane and preventing the flow. Finally, the Cake Formation Model assumes particle accumulation on the membrane surface in a permeable cake of increasing thickness. These mechanisms have been used individually, as well as in combination to explain experimental observations [12].

Earlier works of our laboratory [13] have shown that the permeate flux decreases overtime, due to fouling, so an increase in feed water pressure is operated to ensure a constant permeate flow. Also, improvement in permeate flow rate is accompanied by an enhancement of fouling. In addition, the improved hydraulic performance of the plant occurs immediately after cleaning the fouled membranes.

On the other hand, samples of membrane and fouling were analyzed using a scanning electron microscope (SEM). Results showed that the fouling layer is mainly composed of calcium carbonate [14].

Therefore, in the present study, the permeate flux temporal evolution through two NF membranes (NF90, NF270) and one RO membrane (BW30LE4040) is studied by analyzing various pore blocking models for NaCl removal.

The fouling process is characterized through four pore blocking models as described above. It was found that the Complete Pore Blocking Model exhibited better fit with the experimental data with a reasonably high value of the regression coefficient ($R^2 \approx 0.95$).

MATERIAL AND METHODS

Pilot used

Experiments were performed in an NF/RO pilot plant (E 3039) supplied by TIA Company (Technologies Industrielles Appliquées, France). The pressure applied over the membrane can be varied from 5 to 70 bars with manual valves (Fig. 1). The pilot is equipped with two identical spiral-wound modules operating in series. Each module contains one element. The pressure loss is about 2 bars corresponding to 1 bar of eachmodule. Table 1 gives the characteristics of the commercial membranes. Feed water salinity is 2 g L^{-1}. The treatment pilot is operated in semi-batch mode, i.e. the permeate is recovered, and the retentate is continuously recycled in the feed tank. This option allows continuous water treatment and approximates industrial conditions. The pressure was set for each membrane at 8 bar in order to have the same operating conditions in terms of pressure for the three studied membrane (BW30, NF90 and NF270) and the experiments were performed at 20°C. Samples of permeate were collected and thewater parameters were determined analytically following the standard.
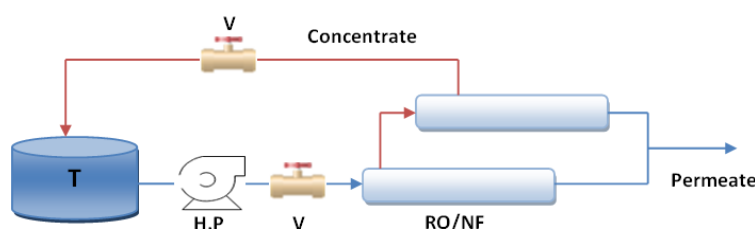
Fig. 1. Schematic diagram of the nanofiltration/reverse osmosis pilot plant. T: tank; H.P: High pressure pump; V: pressure regulation valve.

Table 1. Characteristics of the membranes

Membrane	Surface (m^2)	P$_{max}$ (bars)	Feed pH	Max. T (°C)	Material	Manufacturer
BW30LE4040	7.6	41	2-11	45	Polyamid	Filmtec
NF90	7.6	40	3-10	45	Polyamid	Filmtec
NF270	7.6	40	3-10	45	Polyamid	Filmtec

Mathematical model

Flux decline for a constant pressure dead-end filtration can be described by the following mathematical expression [12]:

$$\frac{d^2t}{dV^2} \left(\frac{dt}{dV}\right)^n \qquad (1)$$

where t is the filtration time, V is the total filtered volume and n is an exponent that depends on the fouling model (n = 2 for complete pore blockage, n = 1.5 for pore constriction, n = 1 for intermediate blockage and n = 0 for cake formation) (Fig. 2).
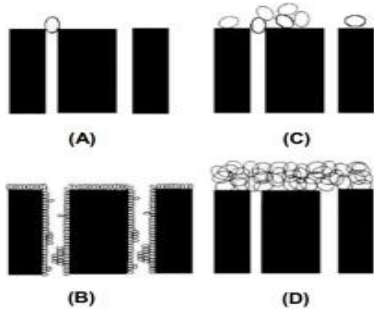
Figure 2. Schematic drawing of the assumed fouling mechanisms: (A) complete blocking; (B) internal pore blocking; (C) intermediate blocking; (D) cake formation [15].

For n=2 (Complete Blocking Model), the size of the particles is larger than that of the membrane pore; particles deposit on the membrane surface and block the entrances of membrane pores completely with no overlapping particles.

For n=1.5 (Standard Blocking Model), the internal volume of the pores decreasesproportionally to the permeate volume due to deposition or adsorption of microsolutes on the pore walls. Material not rejected by the pore entrance is adsorbed or trapped on the pore wall or in the membrane support, thus leading to a decrease in pore volume.

For n=1 (Intermediate Pore Blocking Model), each particle arriving at the membrane settles on another particle, which had arrived previously and was already blocking some pore, or directly blocks some membrane area;

For n=0 (Cake Formation Model), each particle locates on others that have already arrived and are blocking some pores and there is no room for directly obstructing any membrane area.

The permeate flux is presented as [16]:

$$J = \frac{1}{A}\frac{dV}{dt} \qquad (2)$$

which can be written as:

$$\frac{dt}{dV} = \frac{1}{A.J} \qquad (3)$$

Taking the derivative of Eq. 3 with respect to t and substituting in Eq. 1, we obtain the governing equation of flux decline with time as follows [16]:

$$\frac{dJ}{dt} = -\alpha J^{3-n} \qquad (4)$$

where α is a constant and n is a general index which depends on fouling mechanism. The analytical solutions of Eq. 4 for each n value, as well as the linear forms of flux expressions are listed in Table 2, where J_0 is initial flux and K_b, K_s, K_i and K_c are model parameters [16].

Optimization and statistical analysis

To identify the fouling mechanism, the parameters K_b, K_s, K_i and K_c were estimated according to the nonlinear regression optimization procedure. The sum of the squares of the residuals between numerical predictions and experimental data was minimized [17]. Optimization runs were performed sequentially for each set J × t by assigning (n = 0, 1.0, 1.5, 2.0).

Additional statistical parameters were examined, as root mean square error (RMSE), normalized root mean square error (NRMSE) and Nash-Sutcliffe efficiency (NSE) coefficient. The RMSE is the distance, on average, of a data point from the fitted line. The NRMSE calculates theresidual variance. The NSE is a normalized statistic that determines the relative magnitude of the residual variance (noise) compared to the measured data variance (information).

RESULTS AND DISCUSSION

Calculated model parameters of flux decline for all membranes are summarized in Table 3.

Fig. 3 shows good fit between observed and calculated flux. However, according to statistical results in Table 3, the Complete Blocking Model was the mathematic modelthat best represented flux decline with time for BW30L E4040, NF270 and NF90, as R^2 is above 0.95 for this model. Table 3 also shows that the cake formation model was the farthest away from the experimental data, showing that cake formation was discrete, or did not occur at all, in the membranes.

Table 4 shows the results of the statistical analysis, for the Complete Blocking Model, as described in the Material and methods section. The RMSE coefficient obtained has a small value, the NRMSE function is less than unity and the NSE coefficient is close to 1. This result demonstrates the

good performance of this model and of the optimization procedure. Also, the permeate flux decline *versus* time for the three membranes is presented in Fig. 3. According to the figure, the observed permeate flux is continually reduced due to concentration polarization and fouling phenomena.

Fig. 4 shows the cumulative permeate volume per unit membrane surface *versus* time. It indicates a continuous increase of the current flux with time that is wellrepresented by the Complete Blocking Model.

Table 2. Solutions of Eq. 4 for different n values

Model	(a) Complete blocking	(b) Standard blocking	(c) Intermediate blocking	(d) Cake formation
$\dfrac{d^2t}{dv^2} = k\left(\dfrac{dt}{dv}\right)^n$	n = 2.0	n = 1,5	n = 1	n = 0
J=f(t)	$J = J_0\exp(-K_b t)$	$J = \dfrac{J_0}{(\frac{K_S J_0}{2}t + 1)^2}$	$J = \dfrac{1}{K_i t + \dfrac{1}{J_0}}$	$J = \dfrac{J_0}{(1 + 2K_C J_0^2 t)^{\frac{1}{2}}}$

Table 3. Calculated mathematical parameters for the three membranes

	BW30LE4040	NF270	NF90
Complete Blocking model	K_B=0.000313 $R^2 = 0.95$	K_B=0.00011 $R^2 = 0.95$	K_B=0.00026 $R^2 = 0.96$
Standard Blocking model	K_S =16.26 $R^2 = 0.92$	K_S =3.29 $R^2 = 0.92$	K_S =10.49 $R^2 = 0.93$
Intermediate Blocking model	K_i =17.94 $R^2 = 0.91$	K_i =3.29 $R^2 = 0.91$	K_i =11.80 $R^2 = 0.90$
Cake Formation model	K_C =1025196.70 R^2 =0.90	K_C =111467.48 R^2 =0.90	K_C =524237.33 R^2 =0.90

Table 4. Results of the statistical analysis for the Complete Blocking Model

Membrane	RMSE (%)	NRMSE(-)	NSE (-)
NF270	0.025	0.031	0.95
NF90	0.029	0.041	0.97
BW30LE40	0.027	0.059	0.98
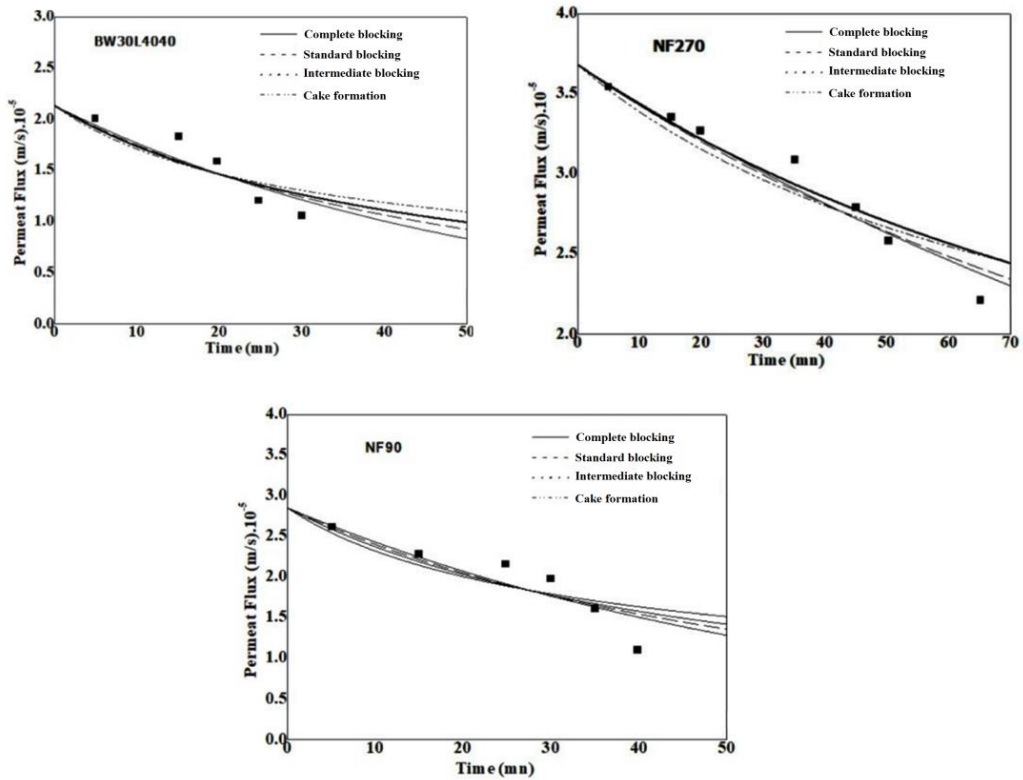
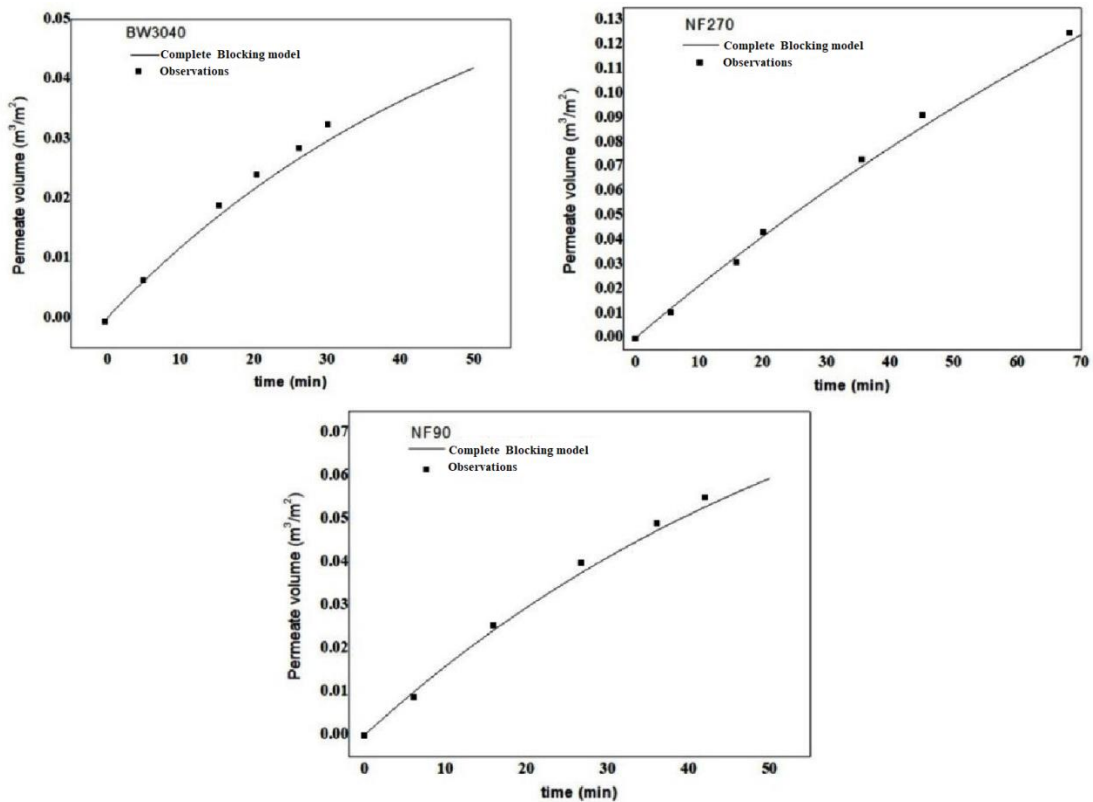**Figure 3**. Permeate flux decline *versus* time for BW30L4040, NF270 and NF270.

Figure 4. Cumulative permeate volume per unit membrane surface *versus* time for BW3040, NF270 and NF90.

CONCLUSION

In this paper, four models were applied to describe the flux decline with time in NF and RO membranes due to fouling phenomena during desalination process: Complete Blocking Model, Standard Blocking Model, Intermediate Blocking

Model and Cake Formation Model. Results show that the Complete Blocking Model was the best representation of pore blocking for NF and RO membranes.

The given data are certainly not sufficient to verify the distinct influence of each of the proposed phenomena. This would require custom designed, more demanding experiments. Still, the example shows that the resulting model is capable of predicting the filtration decline.

REFERENCES

1. A. Shokri, *Bulg. Chem. Commun.*, **50**, 21 (2018).
2. A. Shokri, *Bulg. Chem. Commun.*, **50**, 27 (2018).
3. A. Shokri, M. N. Shoja, *Bulg. Chem. Commun.*, **50**, 1 (2018).
4. A. Shokri, *Iran. J. Chem. Chem. Eng.*, **38**, 5 (2019).
5. M. Bchiti, M. Igouzal, F. El Azhar, H. Oudda, A. El Midaoui, *Bulg. Chem. Commun.*, **51**, 625 (2019).
6. N. Zouhri, M. Igouzal, M. Larif, M. Hafsi, M. Taky, A. Elmidaoui, *Desal. WaterTreat.*, **120**, 41 (2018).
7. M. Igouzal, F. El Azhar, M. Hafsi, M. Taky, A. Elmidaoui, *Desal. Water Treat.,* **93**, 30 (2017).
8. E. Iritani, *Drying Tech.*, **31,** 146 (2013).
9. G. L. Salinas-Rodriguez Amy, J. C. Schippers, M. D. Kennedy, *Desalination*, **365**, 79 (2015).
10. E. Iritani, S. Tachi, T. Murase, *Colloid Surface A*, **89**, 15 (1994).
11. V. L. Vilker, *AIChE Journal*, **27**, 632 (1981).
12. J. Hermia, *Trans. Inst. Chem. Eng*. **60**, 183 (1982).
13. S. El-Ghzizel, H. Zeggar, M. Tahaikt, F. Tiyal, A. Elmidaoui, M. Taky, *J. WaterProcess. Eng.,* **36**, 1 (2020).
14. El-Ghzizel, H. Jalte, H. Zeggar, M. Zait, S. Belhamidi, F. Tiyal, M. Hafsi, M. Taky, A. Elmidaoui, *Membr. Water Treat.,* **10,** 277 (2019).
15. W. R. Bowen, J. I. Calvo, A., Hernández, *J. Membrane Sci.*, **101**, 153 (1995).
16. C. Rai, P. Rai, G. C. Majumdar, S. De, S. DasGupta, *Food Bioprocess Tech.*, **3**, 545(2010).
17. S. T. D. Barros, C. M. G Andrade, E. S. Mendes, L. Peres, *J. Membrane Sci.*, **215**, 213 (2003).

Optimal synthesis and management of supply chains for production and utilization of biogas

E. Ganev*, V. Beschkov

Process Systems Engineering Laboratory, Institute of Chemical Engineering, Bulgarian Academy of Sciences, Sofia 1113, Bulgaria

The continuous increase in greenhouse gas emissions due to the rapid development of world economy, as well as the growing demand for electricity require serious attention to the so-called "green energy" to meet permanently the needs of modern human society in conditions of sustainability. The present research focuses on studying biogas production technologies, evaluating raw materials and products, carefully studying and evaluating all possible flows of raw materials and products, and assessing the environmental impact of this activity. Based on the above study, an optimization model is created through mixed integer linear programming (MILP) to determine potential locations and optimal parameters, as well as transport flows of existing and potential activities.

Keywords: integrated biogas supply chain; optimal design; life cycle analysis; greenhouse gases emissions; solid waste use; economic, environmental and social criteria

INTRODUCTION

Owing to the natural processes in the Earth flora and fauna, even without human intervention, significant amounts of gases (e.g. methane) are generated with the most serious greenhouse effect. On the other hand, as a result of human activity, biodegradable waste is generated both from everyday life and from industry, i.e. from agriculture, forestry, animal husbandry, municipal wastewater treatment plants, etc. These activities reinforce the generation of putrefactive gases on an extremely large scale and promote the need to create technologies and optimally design the flows in order to achieve sustainable development in modern conditions. On the other hand, the fossil energy resources of the Earth are limited and therefore there is a growing need for putting into operation of renewable resources. This is why the social, economic and environmental impacts of biofuels have become an important research topic in the last decade. The exhaustion of the crude oil reserves and the significant levels of environmental pollution encourage researchers and industrials to seek and find solutions in this direction [1]**.**

The massive industrial production of biogas began at the turn of the last century, while in China and India this technology was applied much earlier on a domestic scale. More than 78 biogas plants were built in Japan until 2012 and more than 40 million households of anaerobic digesters were built in China from 2003 to 2013. The US market of biogas is undergoing a rapid expansion and about 2000 biogas plants were operating in the US until soon. The EU is the world leader in biogas electricity production, with more than 10 GW installed and 17,400 biogas plants, in comparison to the global biogas capacity of 15 GW in 2015. European policy on the use of biomethane as a fuel for vehicles or for injection into the natural gas network makes Europe the world's leading producer, with 459 plants producing 1.2 billion cubic meters in 2015 and 340 plants fed on the gas network, with a capacity of 1.5 million cubic meters [2].

Globally, some countries have adopted policies to enhance the bioenergy integration into their economies. For example, the Indian government in 2009 adopted a policy for the production of about 14,105 t/y of biofuels, which is the use of non-edible raw materials extracted from non-agricultural land in order to prevent food and fuel market conflicts [3].

The planning and operation of such an initiative requires special attention to be paid to regional regulation of resource management and spatial energy planning in order to avoid possible tensions and to maintain strict sustainability limits for the use of biomass [4].

The problem with the location of biodigesters is essential for the feasibility of bioenergy projects, as the location can reduce the cost of transporting biomass in combination with environmental standards in compliance with environmental legal requirements. In addition, the many scientific developments on this topic provide grounds for aspects that need to be well studied in order to

---

* To whom all correspondence should be sent:
E-mail: evgeniy_ganev@iche.bas.bg

expand the knowledge about the location of the biodigestor [5]. The social aspect in location models can be considered as an example of this, as this is rarely considered [6]. The mixed-integer mathematical model offers opportunities for optimally locate the hubs (to collect feedstock) and the plants, to minimize the total cost of operating this supply chain system for renewable energy [7]. When developing the model, it is good to pay attention to: represent capital and operational expenditures at the biogas plant; the chain from the farmer to the end market; changes of mass and energy content along the chain by modeling the losses and gains for all processes in the chain [8].

The purpose of this research is to select the optimal technology for biogas production, to evaluate raw materials and products of this technology, to research and evaluate all possible flows of raw materials and products, as well as to make environmental impact assessment resulting of this activity. Based on the above research, an optimization model will be created through mixed integer linear programming (MILP) to determine potential locations and optimal parameters of potential biogas production within the Republic of Bulgaria.

PROBLEM DISCRIPTION

The main elements of supply chain (SC) for biofuels are: farms, storage facilities, commercial sites and transport [9]. Based on this framework, a common framework for the biogas supply chain has been developed (see Figure 1) which includes biomass production sites, biogas production and processing plants, electricity and heat cogeneration sites, compressed gas and transport facilities between the individual nodes. In general, biomass raw materials are transported by trucks from neighboring farms to the biogas plant organized by the farmers' cooperatives. Cooperatives act as a link between producers and buyers. To this end, storage facilities between farms and biogas plants are required. It is also necessary to take into account pre-treatment prior to storage in order to improve the quality of storage and adaptability for further processing.

We introduce the superstructure of the integrated biogas supply chain (IBGSC). It is based on the overall framework of the biogas supply chain (Figure 1) and it is shown in Figure 2. It includes the following elements:

1.　a set of biomass production areas where different types of biomass are used as raw material for biogas plants;

2.　a set of candidate sites for the implementation of biogas plants of several capacity options;

3.　a set of cogeneration zones and sale of compressed biogas, where the final products are sold with certain maximum requirements;

4.　a set of existing biogas plants.

The objective is to determine the number, location, and size of the biogas plants and bioresources to be transported between the various nodes of the designed network so that the overall net present value is minimized while respecting the constraints associated with product demands. This means that biogas plants built on a stage will operate in the next time interval, while allowing renovations to increase capacity to production.
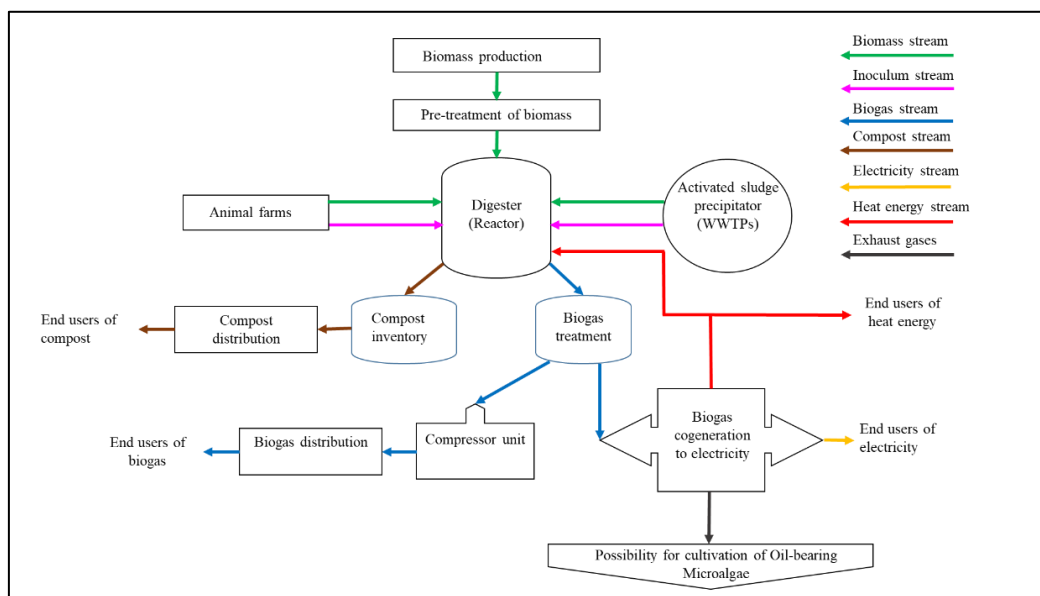
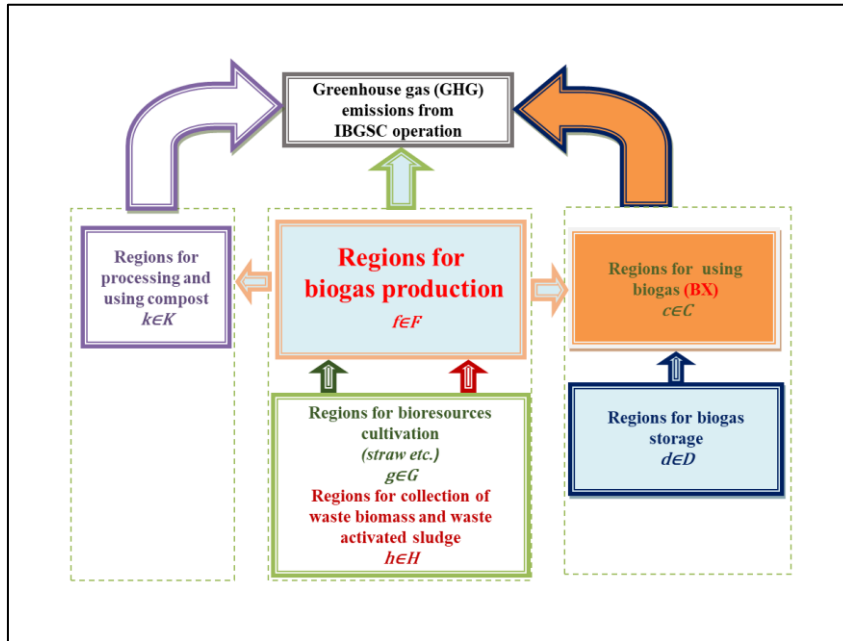**Figure 1.** General framework of the biogas supply chain.

Figure 2. Superstructure of integrated biogas supply chain (IBGSC).

We look at IBGSC for a long planning horizon H (10 years). The whole time horizon H is subdivided in the set of discrete time intervals t. This time interval is divided into several equal time subintervals $t = \{0,1,2,\ldots,T\}$, each of which lasts ∇t. It is assumed that during the planning horizon the value of biogas consumption will change with a predictable value. At the same time, it is assumed that the annual increase in biogas consumption is in accordance with the requirements of Regulation (EU) 2018/1999.

MODEL FORMULATION

This research describes a generic mathematical model to help decision makers in the design and planning of sustainable SC based on the LCA (life cycle assessment) methodology. The model establishes the link with the emission trading scheme to achieve sustainability objectives. Although SC sustainability recognizes the link between the economic, environmental, and social performance, an examination of social performances (labor equity, healthcare, safety) shows that they are dependent on the context of operation of the SC, the government policies, and cultural norms. Thus, without loss of generality, we do not include the social performance in the mathematical formulation [10].

MATHEMATICAL MODEL DESCRIPTION

To start with the description of the MILP model, we first introduce the parameters, that are constant and known a priori, and the variables that are subject to optimization. Then we describe step by step the

mathematical model by presenting the objective function and all the constraints. First of all, we introduce the set of time intervals of the horizon of planning $t = \{0,1,2,\ldots,T\}$. The subscript t indicates the variable or parameter corresponding to the t th interval of the planning [10].

BASIC RELATIONS FOR THE PROBLEM

The analysis related to the production and distribution of biogas will be performed according to three criteria, economic, environmental and social. The optimal solution would be a compromise between these three criteria (Figure 3).
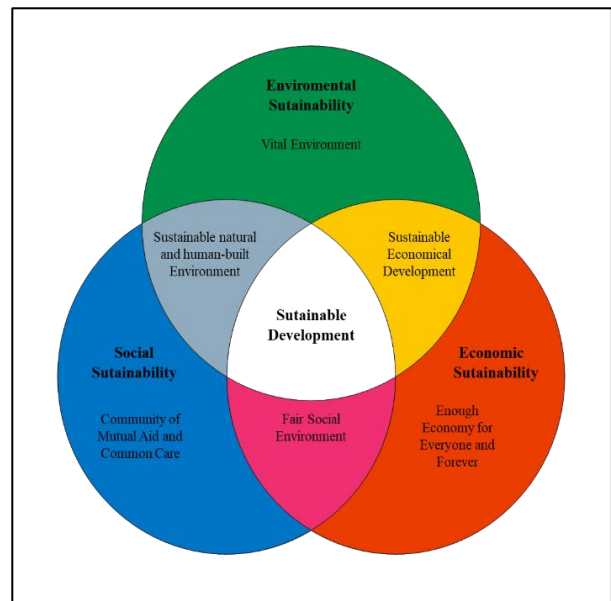

Figure 3. Sustainable development and management concept of IBGSC.

A) Basic relations for total environmental impact TEI_t, $[kg_{CO_2eq}/d]$

Among the different approaches available to assess the environmental impact of processes and organizations, the LCA method seems to be the most promising. It aggregates the results of different aspects of environmental studies including greenhouse gas (GHG) emissions that are recognized as the most harmful elements to the environment and responsible for climate change. The environmental impact of the IBGSC is measured in terms of total GHG emissions $[kg_{CO_2eq}]$, stemming from SC activities and the total emissions are converted to carbon credits by multiplying them with the carbon price (per kg_{CO_2eq}) in the market.

The environmental impact of IBGSC is assessed on the basis of total annual GHG emissions, such as carbon dioxide (CO_2), methane (CH_4) and nitrogen oxide (N_2O) resulting from supply chain activities. The greenhouse gases are grouped in a common indicator in terms of equivalent carbon dioxide emissions $[kg_{CO_2eq}/y]$ using their respective global warming potentials (GWPs) based on the recommendation of the Intergovernmental Panel on Climate Change (IPCC, 2007) [11] for a 100-year time horizon as follows: 1 for CO_2, 25 for CH_4 and 298 for N_2O.

An environmental objective is to minimize the total annual GHG emission resulting from the operations of the biogas supply chain. The formulation of this objective is based on the life cycle analysis, which takes into account the following stages of the fuel life cycle (Figure 4):

➢ The biomass production stage consists of different stages depending on the feedstock type and the subsequent use of it.

➢ The biomass transport stage refers to the supply of biomass to the conversion plant.

➢ The biomass conversion stage to biogas.

➢ The biogas transportation stage of facilities to the costumers zones and the cogeneration.

➢ The biofuel end-use stage is the stage where the biofuel is introduced in the cogenerator and burnt to provide electricity and heat energy.

➢ Environmental assessment criteria will be understood as the overall environmental impact during the operation of the IBGSC by the resulting greenhouse gas emissions at each time interval $t \in T$. These emissions are equal to the sum of the environmental impacts of each stage of the life cycle. Greenhouse gas emissions are usually determined as follows for each time interval $t \in T$:

$$TEI_t = ELS_t + ELB_t + ELD_t + ETT_t + ESW_t + ECOG_t, \forall t \qquad (1)$$

where all quantities are measured in $[kg_{CO_2eq}/d]$ as follows:

➢ TEI_t Overall environmental impact of the life cycle of IBGSC;

➢ ELS_t Biomass cultivation;

➢ ELB_t Biogas production;

➢ ELD_t Petroleum diesel production;

➢ ETT_t Raw material and product transportation;

➢ ESW_t Compost utilization (solid waste) for each time interval $t \in T$.
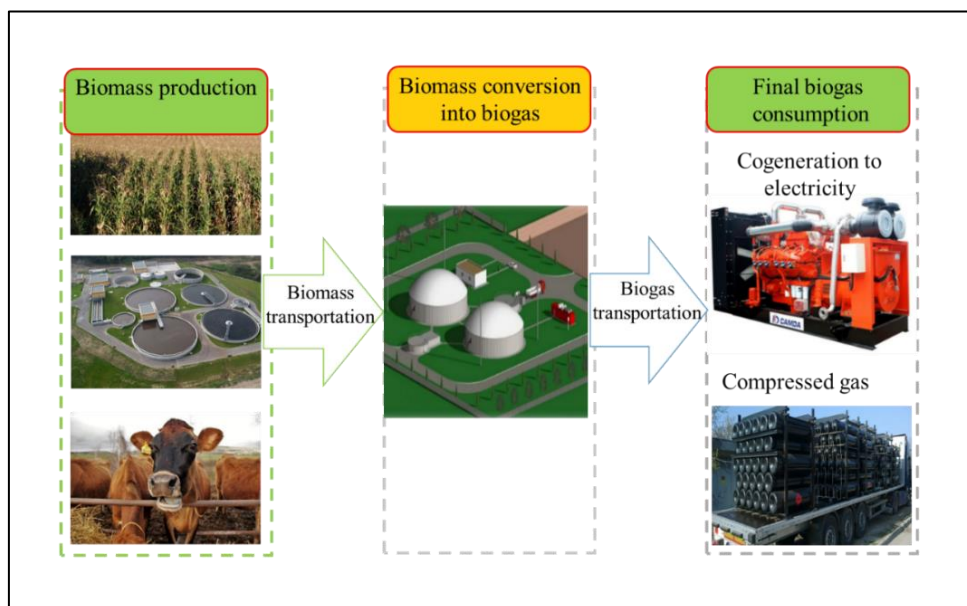
➢ $ECOG_t$ The use of biogas in co-generators.

Figure 4. Biogas life cycle stages.

B)   Basic relations for total cost TDC_t, [$\$/y$]

The annual operational cost includes the biomass feedstock acquisition cost, the local distribution cost of final fuel product, the production costs of final products, and the transportation costs of biomass, and final products. In the production cost, we consider both the fixed annual operating cost, which is given as a percentage of the corresponding total capital investment, and the net variable cost, which is proportional to the processing amount. In the transportation cost, both distance-fixed cost and distance-variable cost are considered. The economic criterion will be the cost of living expenses to include total investment cost of biogas production facilities and operation of the IBGSC [12]. This price is expressed through the dependence for each time interval $t \in T$:

$$TDC_t = TIC_t + TPC_t + TPW_t + TTC_t + TTAXB_t - TL_t - TA_t, \forall t \qquad (2)$$

where all quantities are in [$\$/y$]:

TDC_t IBGSC total expenses for the year;

TIC_T Total investment cost for the production capacity of IBGSC compared to the operating period and the purchase of the plant per year;

TPC_T Production costs for biogas production;

TPW_T Production costs for solid waste disposal to compost;

TTC_T Total shipping costs of IBGSC;

$TTAXB_T$ Carbon tax calculated on the total amount CO_2, generated by the operation of the IBGSC;

TL_t Government incentives for biogas production and consumption;

TA_t Total value of by-products (compost).

C)   IBGSC   Social   Assessment   Model, [*Number of Jobs*]

The IBGSC Social Assessment Model defines the expected total number of jobs created (J_t) as a result of the operation of all elements of the system during its operation:

$$Job_t = NJ1_t + LT_tNJ2_t + LT_tNJ3_t, \ \forall t \qquad (3)$$

where the components of (3) are determined according to the relations at each time interval $t \in T$, [Number of Jobs/y]:

$NJ1_t$ - the jobs created during the installation of biogas facilities and solid waste;

$LTNJ2_t$ - the jobs created during the operation of biogas facilities and solid waste;

$LTNJ3_t$ - the jobs created during biogas production.

Equation (3) represents a simplified model of the social assessment criterion used in [10].

MODEL CONSTRAINTS

For the MILP SC network design model, there are many constraints to be considered. These constraints are of many kinds including the balance constraints of all products, the capacity limit constraints, the minimum capacity occupation constraints, and the demand satisfaction constraint.

DISCUSSION

This study discusses the optimal location of biogas plants and the operation of the IBGSC. The MILP approach developed by us for the design and planning of IBGSC according to economic and environmental criteria is applied [10]. An optimization model has been developed to enable decisions to be made on biogas production infrastructure, including treatment points, volumes and logistics, both from biomass to biogas and to biorefineries to co-generation systems and markets. The development of a flexible optimization model makes it possible to solve a wide range of problems related to biofuels, as this area is changing rapidly (not only in economic but also in other dimensions, such as strategic decisions related to development and progress in this area). All of them can be included very easily in the optimization model, which would lead to significant benefits.

CONCLUSIONS

One of the valuable features of the approach is the ability to identify and solve a wide range of problems at different scales and levels such as the location of facilities and the choice of raw materials. In addition, the model itself could easily be extended to cover strategic planning issues, such as whether or not to invest in new production facilities, their location and the introduction of environmental and other external factors in the calculation of total costs.

The criteria for optimizing the model for each specific case will reflect the objectives of the stakeholder and may include maximum economic efficiency, best environmental behavior, minimum land usage, minimum total costs, etc.

Another feature of the proposed approach is that the model is not unnecessarily complicated and applying it, you can easily solve urgent problems without the need of developing new codes or optimization methods.

REFERENCES

1. T. Mizik, G. Gyarmati, *Clean Technol*., **3**, 19 (2021), https://doi.org/10.3390/cleantechnol3010002.

2. B. R. Sarker, B. Wu, K. P. Paudel, *Appl. Energy,* **239**, 343 (2019), https://doi.org/10.1016/j.apenergy.2019.01.216.

3. J. M. Egieya, L. Čuček, K. Zirngast, A. J. Isafiade, Z. Kravanja, *BMC Chem. Eng.,* **2**, 3 (2020), https://doi.org/10.1186/s42480-019-0025-5.

4. , T. Soha, L. Papp, C. Csontos, B. Munkácsy, *Renew. Sustain. Energy Reviews*, **141**, 110822 (2021), https://doi.org/10.1016/j.rser.2021.110822.

5. L. A. Díaz-Trujillo, F. Napoles-Rivera, *Renewable Energy*, **139,** 1227 (2019), https://doi.org/10.1016/j.renene.2019.03.027.

6. R. H. Gomes de Jesus, J. T. de Souza, F. N. Puglieri, C. M. Piekarski, A. C. de Francisco, *Energy Reports*, **7**, 3998 (2021), https://doi.org/10.1016/j.egyr.2021.06.090.

7. B. R. Sarker, B. Wu, K. P. Paudel, *Applied Energy,* **239,** 343 (2019), https://doi.org/10.1016/j.apenergy.2019.01.216.

8. I. G. Jensen, M. Münster, D. Pisinger, *European Journal of Operational Research,* **262,** 744 (2017), http://dx.doi.org/10.1016/j.ejor.2017.03.071.

9. I. Awudu, J. Zhang, *Renew. Sustain. Energy Reviews,* **16**, 1359 (2012).

10. E. Ganev, B. Ivanov, N. Vaklieva-Bancheva, E. Kirilova, Y. Dzhelil, *Energies,* **14**, 2261 (2021), https://doi.org/10.3390/en14082261.

11. ARC4 Climate Change 2007: Synthesis Report, Intergovernmental Panel on Climate Change (IPCC), Fourth assessment report. **2007**. Available online: https://www.ipcc.ch/assessment-report/ar4/ [Accessed 2022-02-23].

12. A. Ozlem, N. Shah, L Papageorgiou, *Biomass & Bioenergy,* **41**, 57 (2012).

Formation of clusters in water and their distribution according to the number of water molecules

D. Mehandjiev[1], I. Ignatov[2*], N. Neshev[3], F. Huether[4], G. Gluhchev[5], Ch. Drossinakis[6]

[1]*Institute of General and Inorganic Chemistry, Bulgarian Academy of Sciences, Acad. G. Bonchev Str., Bl. 11, Sofia 1113, Bulgaria*
[2]*Scientific Research Center of Medical Biophysics, 32 N. Kopernik Str., Sofia 1111, Bulgaria*
[3]*Sofia University "St. Kliment Ohridski", Faculty of Physics, Sofia, Bulgaria*
[4]*EVODROP AG, Zürich, Switzerland*
[5]*Institute of Information and Communication Technologies, Bulgarian Academy of Sciences, Acad. G. Bonchev Str., Bl. 2, Sofia 1113, Bulgaria*
[6]*IAWG- Internationale Akademie für Wissenschaftliche Geistheilung, Hauptplatz 44, A-2293 Marchegg, Austria*

Measurements of average energies of hydrogen bonds in water droplets evaporating from a hard surface were analyzed with a mathematical model based on a Gaussian distribution of the number of water molecule clusters with the same energy of hydrogen bonds and the same number of water molecules. The model was derived from results of previous research showing that in bulk water, clusters are formed due to hydrogen bonds, having different numbers of water molecules; as the number of water molecules in the clusters increases, the average energy of the hydrogen bonds also increases; with the evaporation of water droplets, the average energy of hydrogen bonds increases. Thus, in bulk water, at the beginning of evaporation, the maximum number of clusters must have average hydrogen bonds energy of $(-E) = 0.1162$ eV and contain 12-13 water molecules.

Keywords: water, hydrogen bonds, energy, clusters, Gaussian distribution

INTRODUCTION

There is ongoing research on the number of molecules in water clusters. In 2021, four of the authors showed a cluster of 20 H_2O molecules with a size of 0.822 nm [1]. The work was based on Antonov's method of measuring the wetting angle during evaporation of water droplets [2-4]. The method is based on a physical effect where, the wetting angle θ decreases discreetly to 0, while the diameter of the base area changes slightly [2, 5, 6].

Luck views the water like consisting of O-H⋯O groups [5]. Most of them are bonded by energy of the connection (-E) and the remaining are free (E=0). It is accepted that E has a negative value.

This is called model of the two states of Luck [6-9]. Each water molecule has two hydroxyl groups. The number of O-H⋯O groups in a certain volume of water is twice as big as the number of the molecules in it.

Part of hydrogen bonds is restructuring in the vicinity of the spherical part of the drop surface and as a result one obtains the dependence between the surface tension δ and the hydrogen bond energy [10-12]:

$$\delta = -kTl\ln[\ 1+\alpha/[\exp(-\beta E)+\alpha]] \qquad (1)$$

Here k is the Boltzman constant, $\beta=1/kT$, T – the absolute temperature, E – the hydrogen bond energy, α is the ratio of two subvolumes of the phase space related to structuring and restructuring of hydrogen bonds, $\alpha = 28\pm8$ and $I=5.03. 10^{18}$ m^{-2} is density of water molecules at the hydrophobic surface layer.

The values of E and α are fixed by a comparison with experiment. Expression (1) explains fraction C of the actual surface tension γ, i.e. $\delta = C\gamma$ [12]. According to [10, 12] the contribution of non-hydrogen bond interaction amounts to 20% of the true value of γ and C=4/5.

Consider the Helmholtz free surface energy $F=\gamma\Sigma$ where Σ is the spherical part of the drop's surface [10].

At the instant of mechanical equilibrium, F should be minimal, i.e. $dF=0=d(\gamma\Sigma)$ [10]

$$0= \gamma\Sigma - \gamma_0\Sigma_0 \qquad (2)$$

The process of evaporation of water drops is at constant temperature 20°C in a hermetic camera [2].

The expressions for Σ_0 and Σ are as follows [10]:

$$\Sigma = \pi D^2/2(1+\cos\theta); \quad \Sigma_0 = \pi D^2/2(1+\cos\theta_0) \quad (3)$$

$$-E/kT = C\gamma/IkT \quad (4)$$

$$E = C\gamma o(1+\cos\theta)/I(1+\cos\theta_0) \quad (5)$$

During the process, the wetting angle changes in discrete steps and characterizes the average energy of hydrogen bonds as follows:

$$\theta = \arccos(-1+bE), \text{ where } b = I(1+\cos\theta_0)/C\gamma o \quad (6)$$

where θ is the wetting angle, E is the average energy of hydrogen bonds, b is a temperature-dependent parameter [13-18]. The development of the method is Non-equilibrium energy spectrum (NES) and Differential non-equilibrium spectrum (DNES) [1, 15, 19, 20]. They are used for research of natural waters and plants [9, 21, 22]. Molecular dynamics simulation is applied to research the wetting behavior of water droplets on the surface of sandstone under different salinities. The system equilibrium configuration was used for the study of its components interaction. The number of hydrogen bonds was calculated [23].

The average weight reduction values of the investigated drops of deionized water during their evaporation and the corresponding values of the wetting angle are shown in Table 1. The average initial height of the droplets was h_i=2.30 mm and their average final height was h_f=0.26 mm. The layering structure of water has a periodicity of 0.30 ± 0.03 nm [24].

Table 1 illustrates the dependence of the wetting angle on the sequential number of the corresponding measurement. This angle decreased from 74 deg to 10 deg and the dependence had a step character.

Table 1. Average weight reduction values of water drops during their evaporation and the corresponding values of the wetting angle.

Wetting angle, (°) θ	Weight, mg
74	48.0
66	37.9
58	29.0
50	21.3
42	14.8
34	9.4
26	5.3
18	2.4
10	0.6

Another previous study of ours has shown that the discrete changes in hydrogen bonds energy of water clusters have the same value and are based on formation of clusters with different numbers of water molecules [25]. There are researches of clusters with different numbers of water molecules according to

the energy of hydrogen bonds among water molecules.

Infrared spectroscopy studies have detected the following clusters: $H^+(H_2O)_{22}$ [26] and $(H_2O)_n$, n=6-22 [27]. In addition, the total interaction energy has been represented by five terms; repulsive, charge–charge, intramolecular relaxation, polarization, and hydrogen bonding with three models for n = 6-20 [28]. Water clusters have also been described with the density functional theory (DFT) for n=2-20 [29].

Extensive *ab initio* calculations with 6-31G(d, p) and 6-311++G(2d, 2p) base sets were used for modeling of possible structures of water clusters $(H_2O)_n$ for n=8-20. The most stable clusters were found in tetramer and pentamer rings. For n = 8, 12, 16 and 20, the derived clusters were cuboid. For n=10 and 15, they were merged into pentamer structures [30]. It has also been found that, for n=20, about 25% of water molecules are structured in such clusters [31].

In general, our previous research on water structure, cluster formation and hydrogen bonds energy leads to the following conclusions [1, 17]:

1. In water, clusters are formed due to hydrogen bonds, having different numbers of water molecules.

2. As the number of water molecules in the clusters increases, the average energy of the hydrogen bonds also increases.

3. With the evaporation of water droplets, the average energy of hydrogen bonds increases.

In this research, the control samples were with deionized water and samples were initially treated with a patented filter EVOdrop [32, 33].

The aim of the present work was to answer the question about what determines the number of water molecules in clusters and about the distribution of clusters in water according to the number of water molecules. In addition, it had to clarify how this distribution changes during evaporation of water droplets from a hard surface.

MATERIALS AND METHODS

The wetting angle θ was measured with a specially designed apparatus which is described in detail in [2-4]. Evaporation of deionized water drops was performed in a hermetic chamber with a stable temperature of 22°C [2, 10]. The drops were placed on BoPET (biaxially-oriented polyethylene terephthalate) foil with 350 μm thickness. Deionized water was initially treated with a patented filter EVOdrop [32, 33].

In order to determine the numbers of water molecules in clusters, as well as the distribution of clusters in bulk water according to these numbers our previous model was used with the following assumptions.

1. The number of clusters of a particular type in bulk water (with equal numbers of water molecules) is related to their average energy of hydrogen bonds.

2. The distribution of the numbers of particular types of clusters is Gaussian.

3. The number of water molecules in clusters (determining their different types) varies from 3 to 22.

To find the distribution of clusters according to the average energy of the hydrogen bond in them, we use the Gaussian function in the following formula:

$$y = [\ 1/s\sqrt{2\pi}\ ]\ .\exp[-\ (x-x_s)^2/2s^2\ ], \qquad (7)$$

where x is the average energy of hydrogen bonds in a particular group of clusters, y is the number of clusters with the same energy of hydrogen bonds and the same number of water molecules, x_s is the average energy of hydrogen bonds for all groups and s is the standard deviation.

RESULTS AND DISCUSSION

The average values of hydrogen bonds energy in water droplets during their evaporation from a BoPET surface, measured with Antonov's method, and the numbers of water molecules are presented in Table 2. The number of order is signed with No. The value (-E) in eV is the energy of hydrogen bonds among water molecules. No(n) stands for the number n of water molecules at order No.

These values stand for x in Eq. (2). As it has been pointed out, the energy (-E) changes stepwise and its increment is always the same and equal to 0.0025 eV [1, 3, 10]. Table 1 also shows the numbers of water molecules that can contribute to these average hydrogen bond energies.

Figure 1. Distribution of the number of clusters with equal energy of hydrogen bonds, on the average energy of
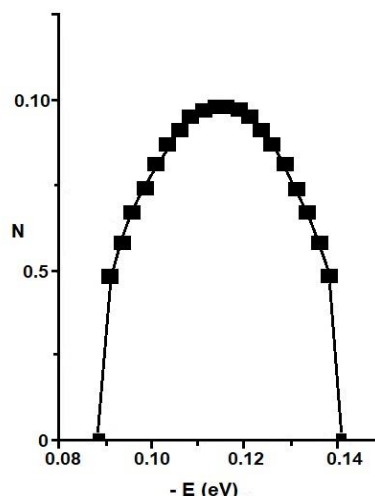
hydrogen bonds

Four energy ranges were considered for cluster formation with particular numbers of water molecules according to the average energy of hydrogen bonds (-E):

Range 1: from 0.0912 to 0.1387 eV;
Range 2: from 0.1062 to 0.1387 eV;
Range 3: from 0.1212 to 0.1387 eV;
Range 4: from 0.1312 to 0.1387 eV.

For each range, the values of y were calculated according to eq. (7).

Fig. 1 represents the distribution of the number of clusters with equal energy of hydrogen bonds (-E) in the measurement range from 0.0912 to 0.1387 eV.

The distribution of the number of clusters with equal numbers of water molecules, on the number of water molecules in them is shown in Fig. 2.

Table 2. Average values of hydrogen bonds energy in water droplets during their evaporation from a BoPET surface

No	-E (eV)	n	No	-E (eV)	n	No	-E (eV)	n
1.	0.0912	3	8.	0.1087	10	15.	0.1262	17
2.	0.0937	4	9.	0.1112	11	16.	0.1287	18
3.	0.0962	5	10.	0.1137	12	17.	0.1312	19
4.	0.0987	6	11.	0.1162	13	18.	0.1337	20
5.	0.1012	7	12.	0.1187	14	19.	0.1362	21
6.	0.1037	8	13.	0.1212	15	20.	0.1387	22
7.	0.1062	9	14.	0.1237	16			

*No - number of order; n - number of water molecules
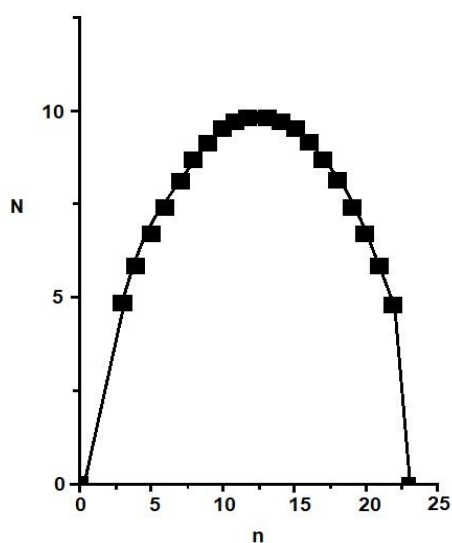
Figure 2. Distribution of the number of clusters with equal numbers of water molecules, on the number of water molecules in them.

If the Gaussian distribution takes place the maximum number of clusters must have average hydrogen bonds energy (-E) of 0.1137 eV or (λ=10.91 μm; $\tilde{v}$=917 cm^{-1}). The research shows that $\tilde{v}$ =917 for the hydrogen-bonded molecules [34]. Assuming that the first type of clusters contains three water molecules and all the rest have one more molecule compared to the previous type as shown in [24], then the next type of clusters will have four molecules, etc. These values are presented in Table 1 and, consequently, the maximum number of clusters have to contain 12-13 water molecules.

The results for the other three ranges are shown in Fig. 3.

As expected, the maxima of these curves are shifted towards higher hydrogen bonds energy (-E). For Range 2, the maximum is at 0.1212 eV or (λ=10.23 μm; $\tilde{v}$=978 cm^{-1}), for Range 3 it is at 0.1287 eV or (λ=9.63 μm; $\tilde{v}$=1038 cm^{-1}) and for Range 4 it is at 0.1362 eV or (λ= 9.10 μm; $\tilde{v}$=1099 cm^{-1}). The same dependence on the number of water molecules is shown in Fig. 4.

It should be pointed out that, during experiments in 2020 with EVOdrop filtration of tap water, local (-E) maxima were measured at 0.1112; 0.1212; 0.1287; 0.1362; 0.1387 eV [33].

During evaporation of droplets, clusters with increasing numbers of water molecules are present. The clusters that are maximum in number in the different ranges have the following composition: Range 2 – 15, Range 3 – 18 and Range 4 – 21 water molecules.
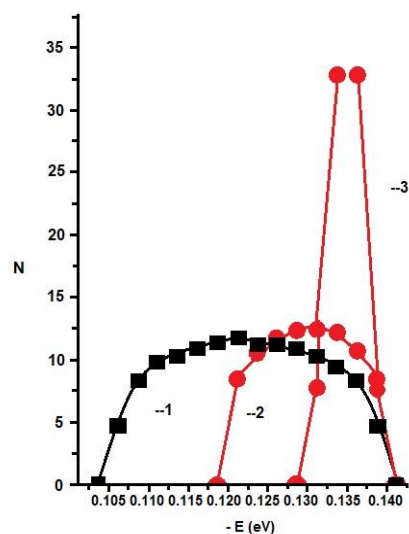
Figure 3. Distribution of the number of clusters with equal hydrogen bonds energy (-E), on the average hydrogen bonds energy in the corresponding ranges. Curve 1 – Range 2 (average hydrogen bonds energy from 0.1062 to 0.1387 eV), Curve 2 – Range 3 (average hydrogen bonds energy from 0.1212 to 0.1387 eV), Curve 3 – Range 4 (average hydrogen bonds energy from 0.1312 to 0.1387 eV).
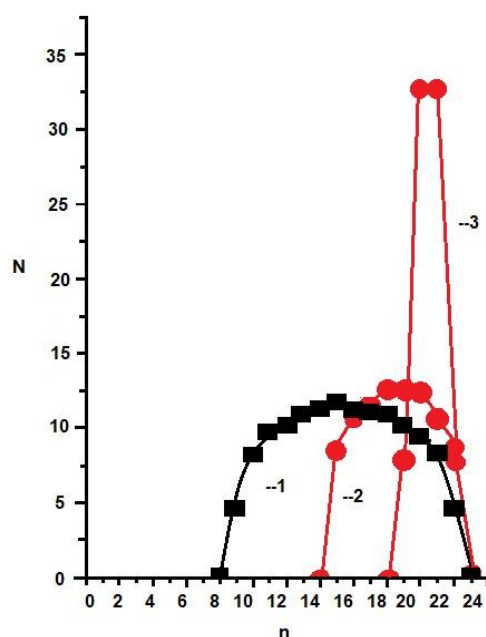
Figure 4. Distribution of the number of clusters with equal numbers of water molecules, on the number of water molecules in the different ranges. Curve 1 – Range 2 (average hydrogen bonds energy (-E) from 0.1062 to 0.1387 eV), Curve 2 – Range 3 (average hydrogen bonds energy from 0.1212 to 0.1387 eV), Curve 3 – Range 4 (average hydrogen bonds energy (-E) from 0.1312 to 0.1387 eV).

Table 3 illustrates the mean values, standard deviations and maximal numbers of water molecules in clusters.

Table 3. Mean values, standard deviations and maximal numbers of water molecules in clusters.

Range of (-E) [eV]	x̄ [eV]	S	n_{max}
0.0912 - 0.1412	0.115	0.0148	11
0.1037 - 0.1412	0.1225	0.01045	15
0.1187 - 0.1412	0.1299	0.00612	18
0.1287 - 0.1412	0.1349	0.00321	21

*Range of (-E) - energy of hydrogen bonds [eV]; $\bar{x}$ [eV] - mean value; S - standard deviation; n_{max} - maximum number of water molecules in clusters.

CONCLUSION

The obtained results show that the structure of water filtered with patented filter EVOdrop has a complex character that could be influenced by external conditions. In the normal state, clusters with different numbers of water molecules are formed in the water. Since the average energy of hydrogen bonds depends on the numbers of water molecules in the clusters, the numbers of clusters with the same numbers of water molecules can vary. Under the assumption that these numbers have Gaussian distribution, different numbers of clusters with equal hydrogen bonds energy are prevalent in water filtered with patented filter EVOdrop.

Under normal conditions, temperature and pressure, the results show that a maximum of 11 water molecules are present in water. During evaporation, the maximum number of clusters changes and those with larger numbers of water molecules prevail. If the types of the predominant clusters have different numbers of water molecules, they may cause different chemical and biological effects which must be taken into account.

REFERENCES

1. I. Ignatov, G. Gluhchev, N. Neshev, D. Mehandjiev, *Bulgarian Chemical Communications*, **53**(20), 234 (2021).
2. A. Antonov, L. Yuskesselieva, Method for determination of structural changes in liquids, *Author's certificate of invention*, 43821 (1983).
3. A. Antonov, *Comptes Rendus de l'Académie Bulgare des Sciences*, **37**, 1199 (1984).
4. A. Antonov, L. Yuskesselieva, I. Teodossieva, *Physiologie*, **26**(4), 2552 (1989).
5. W. Luck, *American Chem. Soc.,* 50 (1980).
6. G. M. Kontogeorgis, A. Hoster, N. Kottaki, E. Tsochantaris, F. Topsoe, J. Poulsen, M. Bache, X. Liang, N. S. Blom, J. Kronholm, *Chemical Thermodynamics and Thermal Analysis,* **6**, 100053 (2022).
7. L. F. Vega, F. Llovell, *Fluid Ph. Equilib*., **416**, 150 (2016).
8. S. Aparicio-Martínez, K. Hall, *Fluid Phase Equilib.*, **254**, 112 (2007).
9. G. Clark, A. Haslam, A. Galindo, G. Jackson, *Mol. Phys*., **104**, 3561 (2006).
10. L. Todorova, A. Antonov, *Comptes Rendus de l'Académie Bulgare des Sciences*, **53** (7) (2000),
11. B. J. Zhang, K. J. Kim, Ch. T. Lee, *Experimental Thermal and Fluid Science*, **96**, 216 (2018).
12. A. Luzar, S. Svetina, B. Žekš, *Chemical Physics Letters,* **96** (4)**,** 485 (1983).
13. A. C. Kumbharkhane, Y. S. Joshi, S. C. Mehrotra, Sh., Yagihara, S. Sudo, *Physica B: Condensed Matter,* **421**, 1 (2013).
14. S. Todorov, A. Damianova, I. Sivriev, A. Antonov, T. Galabova, *Comptes Rendus de l'Académie Bulgare des Sciences*, **61**(5251), 857 (2008).
15. S. Todorov, A. Damianova, A. Antonov, L. Todorova, *Comptes Rendus de l'Académie Bulgare des Sciences*, **63**(4), 555 (2010).
16. P. Gramatikov, A. Antonov, M. Gramatikova, *Fresenius' Journal of Analytical Chemistry*, **343**(1), 134 (1992).
17. J. Jelev, A. Antonov, T. Galabova, *US20070276192A1* (2003).
18. S. Todorov, L. Todorova. *Bulg. J. Phys.,* **46**, 229 (2019).
19. A. Antonov, Dissertation thesis for degree "Doctor of physical sciences", Blagoevgrad, Sofia, 1995.
20. I. Ignatov, T. P. Popova, R. Bankova, N. Neshev, *Plant Science Today*, **9**(1), 41 (2022).
21. S. Boteva, A. Kenarova, G. Radeva, I. Traykov, V. Bogoev, *Comptes Rendus de l'Académie Bulgare des Sciences*, **66**(11), 1579 (2013).
22. I. Ignatov, N. Neshev, T. P. Popova, Y. Kiselova-Kaneva, Ch. Drossinakis, R. Bankova, R. Toshkova, G. Gluhchev, N. Valcheva, M. Angelcheva, G. Dinkov, I. Angushev, T. Todorova, V. Balabanski, S. Baiti, F. Huether, A. I. Ignatov, *Plant Science Today*, **9** (3), 760 (2022).
23. T. Yu, Q. Li, H. Hu, Y. Tan, L. Xu. *Colloid and Surfaces A: Physicochemical and Engineering Aspects*, **632**, 127807 (2022).
24. D. Mehandjiev, I. Ignatov, N. Neshev, G. Gluhchev, Ch. Drossinakis, *Physical Science International Journal*, **25** (12), 15 (2021).
25. J. Smith, C. Cappa, K. Wilson, R. Cohen, P. Geisler, R. Saykally, *PNAS*, **102** (40), 14171 (2005).
26. K. Mizusek, A. Fujii, *J. Phys. Chem. Lett.*, **2** (17) 2130 (2011).
27. A. Lenz, L. Ojamae, *J. Phys. Chem. A*, **110** (50), 13388 (2006).
28. M. Masella, J. P. Flament, *The Journal of Chemical Physics,* **107**, 9105 (1997).
29. Y. I. Neela, A. S. Mahadvi, G. N. Sasty, J. *Phys. Chem. B*, **114** (51),17162 (2010).
30. S. Maheshwary, N. Patel, N. Sathyamurthy, A. D. Kulkarni, S. R. Gadre, *J. Phys. Chem. A,* **105** (46), 10525 (2001).

31. Y. Gao, H. Fang, K. Ni, *Scientific Reports*, **11**, 9542 (2021).
32. F. Huether, Filter system, Fabio and Markus membrane Eng GMBH [CH] *WO2020169852A1* (2020).
33. I. Ignatov, G. Gluhchev, F. Huether, *Physical Science International Journal*, **24** (7), 47 (2020).
34. M. H. Brooker, G. Hancock, B. C. Rice, J. Shapter, *Journal of Raman Spectroscopy*, **20**, 683 (1989).

Selected papers from the 8th International Conference on New Trends in Chemistry (ICNTC), held in Famagusta, May 16 - 18, 2022

Characterization of activated carbon produced from pistachio shell at different temperatures

H. Dolas

Harran University, Hilvan Vocational School, Program of Occupational Health and Safety, Sanliurfa 63900, Turkey

Activated carbons (ACs), which are used as active surfaces in an adsorption process, make the latter successful owing to their high surface area and high volume in terms of micropores. The characteristics of the method used in AC production help to improve the porosity structure of AC and to increase the surface area.

In this work, the effect of different temperatures and H_2SO_4 on the surface area and porosity structure in obtaining AC from pistachio shells was studied. For this purpose, the collected pistachio shells were kept in 10% NaCl and 10% H_2SO_4 solution for 24 h. At the end of the period, the material was carbonized for 45 min at 3 different temperatures (500, 700 and 800 ºC). The obtained ACs were characterized using a surface area and pore size analyzer, Fourier transform infrared (FT-IR) and scanning electron microscopy (SEM). According to the results obtained, it was found that the AC-800 has the highest surface area compared to the other obtained ACs. So, it had a BET surface area of 2093.063 m^2/g, and its micropore volume was 1.053 cc/g. All functional groups in the structure of raw pistachio shells were destroyed for pore formation and the resulting porosity is supported by FT-IR and SEM images. With this new method, ACs with a high surface area were obtained and it was understood that the use of H_2SO_4 decreased the surface area while increasing the temperature increased both the surface area and micropore volume.

Key words: Agricultural waste, Carbonization, Activated carbon, Surface area, Micropore volume.

INTRODUCTION

All living and/or inanimate beings maintain their existence in a certain relationship and cycle in this ecosystem, which we call the environment. As a result of developing technology and other formations, this cycle, which is in a certain order, is disrupted. One of the biggest factors in this deterioration, which is called environmental pollution, is the solid, liquid and gaseous waste. Every breakthrough made to respond to the increasing population and improve the quality of life has led to the development in technology. However, the gas, liquid and solid wastes of the factories established as a result of these developments pollute the air, soil and water, and it is seen that this pollution harms living life [1].

Adsorption is one of the low-cost and easy-to-apply ways to prevent this pollution [2, 3]. Adsorption is the process of chemically or physically adsorbing on the active solid surface (adsorbent) of all charged or uncharged ions and molecules dissolved in the liquid or gas phase. The success of the adsorption depends on the temperature, the physical and chemical state of the ion or molecule to be adsorbed, the ambient pressure and the properties of the active solid surface used. The properties of the active solid surface, especially the surface area and porosity, are of great importance in the adsorption process. Generally, activated carbon (AC) is chosen as adsorbent in adsorption processes. AC is a kind of adsorbent produced from various carbon-structured materials and has a high surface area and a porous structure, the majority being micropores. Thanks to this porous structure, ACs have a high surface area as they can fit surfaces of thousands of square meters per unit weight.

Generally, the tendency is to use agricultural wastes, which are abundant, completely waste, and have a suitable porous structure by losing the hydroxyl and carboxyl groups in their structure, and also have a quality fiber structure in AC production. The use of agricultural wastes with abundant cellulosic and fibrous structure not only reduces the cost, but also contributes to waste management.

For a long time, various agricultural wastes such as wheat straw [4], banana peel [5], orange peel [6, 7], cane sugar [8], walnut shell [9], peanut shell [10], coconut shell [11], olives [12] were used in AC production [13].

In a previous study, the effect of the use of salt as an activator on the surface area was shown. In this study, it was investigated how the use of acid as an activating agent affects the changes in properties such as surface area, micro, meso and macro porosity, thermal degradation and morphological appearance of ACs obtained from the fistic shell by applying different carbonization temperatures.

To whom all correspondence should be sent:
E-mail: hacerdolas@harran.edu.tr

EXPERIMENTAL

Production of AC. Pistachio shells (FK) were collected from the fields of Bozova district of Sanlıurfa province, Turkey. The collected shells were first cleaned of their soft shell and coarse dirt. They were broken into large pieces and washed with tap water. 20 g of dried shells were weighed and poured into 10% NaCl solution in a 250 ml flask. It was kept in this solution for 1 day. Then, the filtered shells were poured into 10 % H_2SO_4 solution in a 250 ml flask and kept in this solution for 1 day. After the activation process, the filtered peels were thoroughly

washed with distilled water. They were dried in an oven at 80 ºC and carbonized in a high-temperature muffle furnace at three different temperatures, 500, 700 and 800 ºC for 45 minutes. This process was carried out in an atmosphere of N_2 gas. The carbonized shells were cooled to ambient temperature were again washed with distilled water to remove excess gas in the pores, and the dried shells were ground and sieved. ACs produced in this way were labeled as AC-500, AC-700 and AC-800 based on the temperature to which they were subjected.
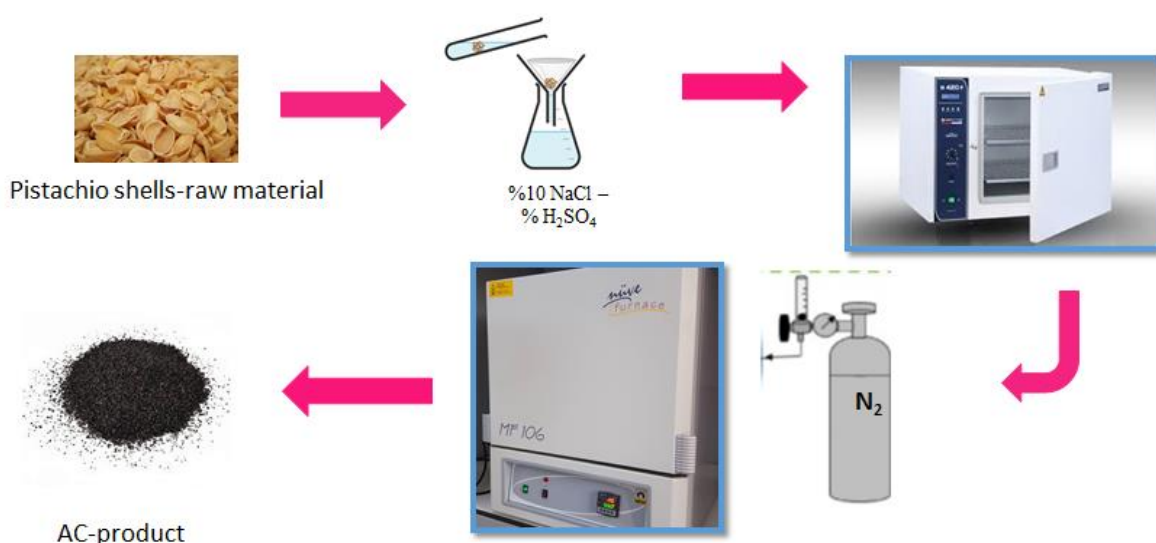
Figure 1. The route of AC production.

Characterization

Surface analysis. NOVA 4000e-Quantachrome surface area and pore size analyzer device was used to determine the active surface area and pore volume of the produced ACs. Before analysis, ACs were dried at 170 ºC under vacuum overnight to open all pores on the AC surface. Based on the nitrogen adsorption method under cryogenic conditions, the adsorption isotherm was obtained at the end of the analysis process. Thanks to the application of this isotherm, the BET surface area [14], Langmuir surface area, pore width, pore volume and micropore surface area by DR method, adsorption energy [15] and BJH method [16] mesopore distribution of AC-800 were determined.

Thermal analysis. Thermal analysis SHIMADZU brand DTG-60A simultaneous DTA-TG apparatus was performed from ambient temperature to 900 ºC by applying a heating rate of 10 C/min. Meanwhile, the medium was fed with N_2 gas. The gas flow rate was chosen as 50 mL/min.

Structural and morphological analysis. The spectrum obtained with SHIMADZU IRTracer-100

FTIR was obtained with 4 cm^{-1} resolution. The pore network in the structure of the AC-800 was demonstrated using SEM images and the ZEISS brand EVO 50 Model SEM device.

RESULTS AND DISCUSSION

Adsorption isotherms. The activity of ACs produced by carbonization of agricultural wastes under suitable conditions due to their cellulosic structure, is indicated by their active surface areas and porosity structure. ACs obtained for this purpose were subjected to N_2 adsorption. For comparison, the raw material peanut shells and commercial activated carbon and the adsorption isotherms of Ac produced in this study are given in Figure 2. The knee formation observed in these graphs, especially at the relative pressure values of 0-0.01 P/Pº (low relative pressure), indicates the presence of micropores in the structure and the gas being adsorbed by them. The more gas adsorption has taken place in this region, the more micropores can be mentioned. As a result, a high surface area can be observed. As can be seen from the figure, the activated ACs obtained by

carbonization at different temperatures adsorbed a very high amount of nitrogen compared to the raw material.
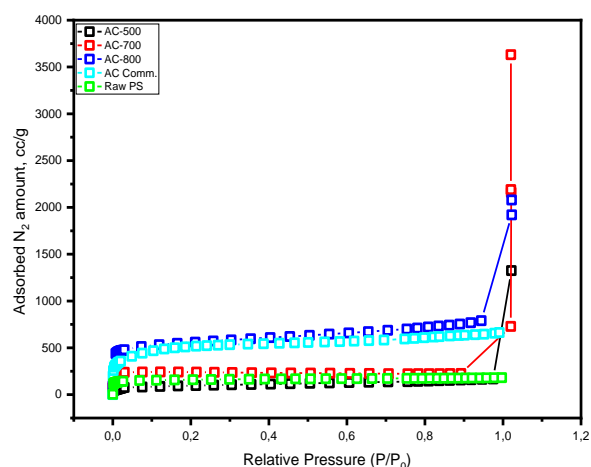
Figure 2. Adsorption isotherms.

The isotherm of the raw material exhibits a monolayer adsorption isotherm. Capillary condensation in the 0.9-1 relative pressure region is not observed. This corresponds to the Type I monolayer adsorption isotherm in the isotherm classification made by the International Union of Pure and Applied Chemistry (IUPAC). Although micropore formations are mostly observed in the structure of such ACs, meso- and macroporosity are relatively less. The produced AC (AC-500, AC-700 and AC-800) exhibits adsorption isotherm corresponding to type IV of IUPAC classification. In such isotherms, the presence of mesopore formation in the structure and even an adsorption with capillary condensation are mentioned. Relatively high surface areas are obtained from structures exhibiting such isotherms. Comparatively, the micropore volume and surface area and adsorption energy obtained by BET and Langmuir surface area DR method are given in Table 1. As can be seen from the table, peanut shells, which are raw materials, have a BET surface area of 500.275 m²/g; ACs produced at different temperatures have BET surface area of, respectively, 422.052 at 500 °C; 1022.031 at 700 °C

and 2093.063 m²/g at 800 °C. In this state, ACs with higher beta surface area than the commercially sold ACs were produced. Langmuir surface area, which expresses the monolayer adsorption surface area, reached the highest value at AC-800. The surface area and pore volume of the microporosity in the structure of AC were determined by the DR technique and are given in Table 1. The change in pore volume and surface area with respect to the diameter is shown in Figure 3 by the BJH method.

The results in the figure clearly show that AC with the highest surface area and volume of porosity has a lower pore size. It is understood that the current micropore volume of AC-800 has the highest micropore volume with 1.053 cc/g and the highest microporosity with a micropore surface area of 2963.759 m²/g. Therefore, the graph supports the result in the table.

Thermal analysis

The material obtained before carbonization was subjected to thermogravimetric analysis and compared with the AC obtained after carbonization in order to see how the pistachio shells used as raw material in the production of activated carbon in the study would degrade in the face of heat treatment. The Tg and DTA curves obtained by controlled heating in nitrogen environment from ambient temperature to 800 °C are given in Figure 4.

When the TG curve is examined, it can be observed that the humidity in the building disappears up to about 100 °C, and this covers a low percentage (3%). In addition, the sample decomposed in one step and this decomposition corresponds to the temperature range of 350-500 °C, where the organic content is lost. In this degradation, the loss was determined as 87% (Figure 3 inner graph). The DTA curve clearly shows that the degradation is in the range of 350-500 °C. The DTA curve of the product (AC) obtained at the end of carbonization shows that there is no significant change in (inset) energy. Thus, it can be said that the transformation is completed under the applied conditions.

Table 1. BET, Langmuir, DR micropore volume, surface area and adsorption energy.

	BET, m²/g	Langmuir, m²/g	DR micropore volume, cc/g	DR micropore surface area, m²/g	Adsorption energy, kJ/mol
Raw Material	500.275	632.858	0.426	1199.900	9.055
Comm. AC	1648	2479.262	0.659	1849.312	14.976
AC-500	422.052	447.019	0.161	453.86	9.872
AC-700	1022.031	1051.394	0.454	1278.232	14.354
AC-800	2093.063	3939.573	1.053	2963.759	10.927

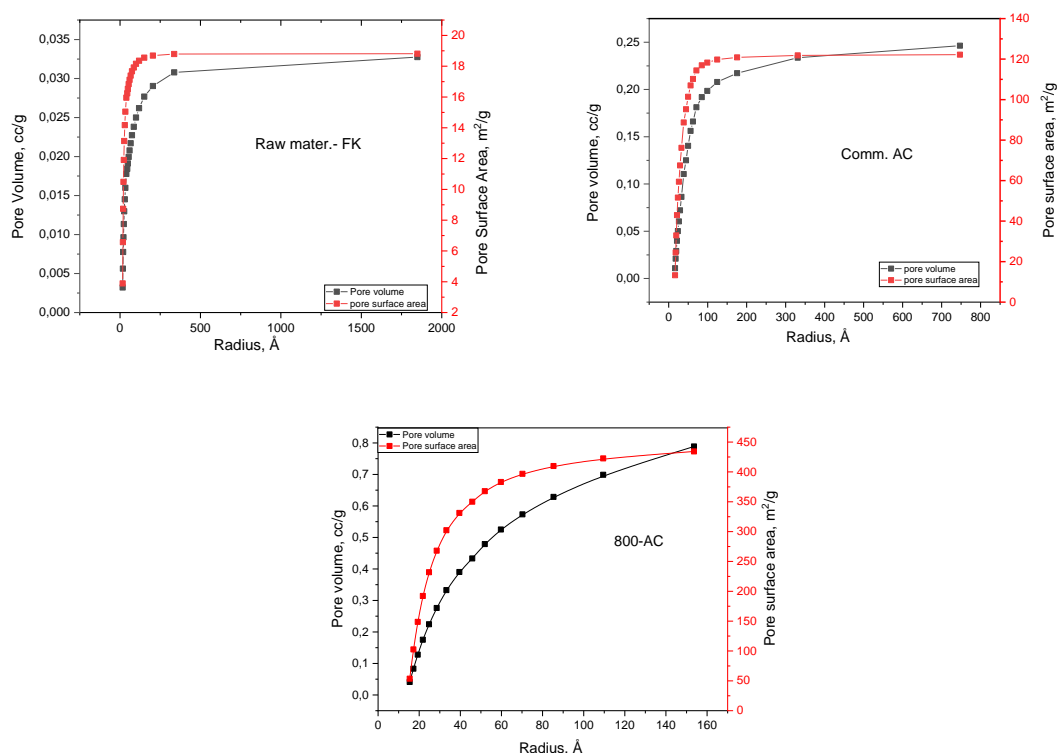**Figure 3.** Distribution of pore volume and pore surface area *versus* radius of AC by BJH method.
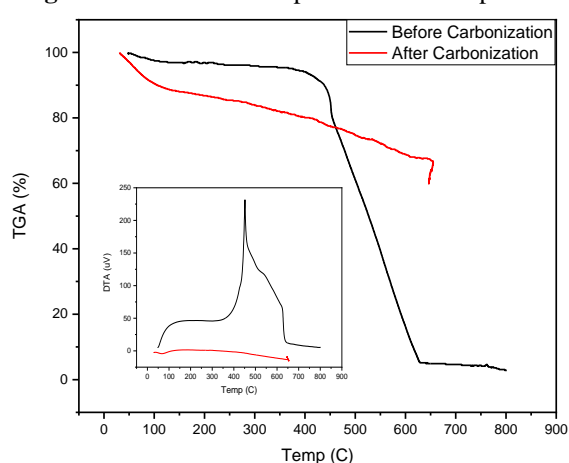

Figure 4. TG curve and DTA curve (inset).

Figure 5. FT-IR spectrum

Structural analysis

Tg data give the information that the organic structure of the raw material is deteriorated, resulting in the formation of pores in the structure of the raw material. In addition, this information was confirmed by the FT-IR spectrum. The products before and after carbonization of the raw material were compared structurally. The FT-IR results obtained are given in Figure 5.

Peanut shells have a cellulosic structure mostly containing H, C elements and OH groups. In addition, information about the presence of carbonyl, ether, ester, alcohol and phenol groups in pistachio shells is also available in the literature [17].
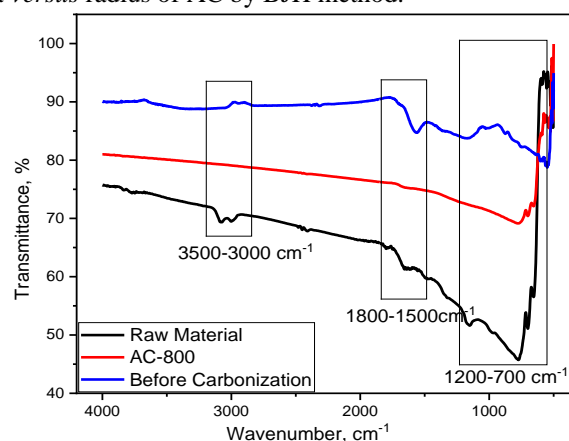
The vibrations in the raw material structure observed in the FT-IR spectrum were vibrations of functional groups such as –OH (3600-3000 cm^{-1} in alcohol and phenols); C=C (alkene group, 2300-2100 cm^{-1}); C=O vibration (carbonyl group in amides, 1820-1650 cm^{-1}), and C-O (alcohol, phenol, ester and ether groups, 1150-1050 cm^{-1}). While stretching vibrations related to all bonds of the organic structure in raw peanut shells are observed very little in the activated material before carbonization, they are observed very limitedly and rarely in the AC structure obtained after carbonization. This shows that the structure collapses step by step during the activation process as a result of high temperature.

Morphological analysis

SEM images of AC-800 samples were examined and compared with the raw material in order to show that the functional groups in the raw organic
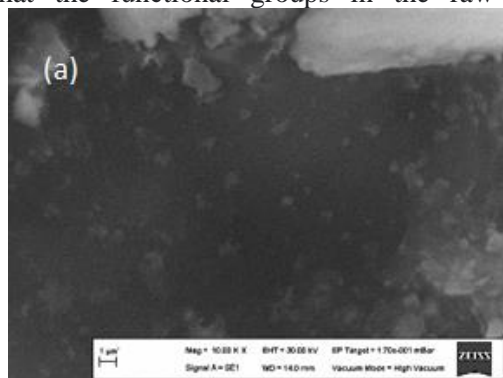
structure were broken down and a new porous structure was formed. The obtained SEM images are shown in Figure 6.
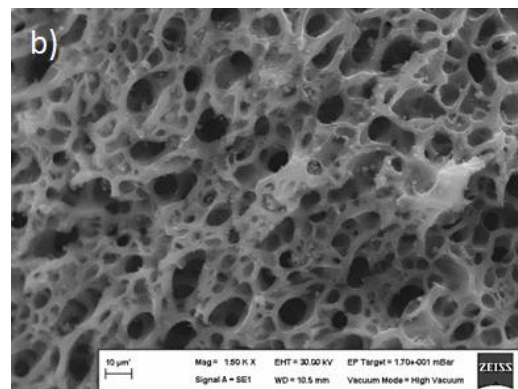
Figure 6. The SEM images of a) raw material and b) AC-800.

SEM images were obtained by applying 30kV energy. While the surface image of the raw material is available in Figure 6a, a distance of 10 μm is given for the AC-800 produced at 800°C as a product in Figure 6b. When both figures are compared, the pores opened in the structure of the raw material can be seen very clearly. The large and small pores formed indicate the structure and high surface area in the AC sample.

CONCLUSION

As a result, the peanut shells accumulated as agricultural waste were activated for 1 day using 10% NaCl or 10% H_2SO_4 solution. Afterwards, these shells were thoroughly washed and carbonized using a nitrogen atmosphere for 45 minutes at three different high temperatures, 500, 700 and 800 °C. Appropriate analyzes were carried out to determine the surface area and porosity structure of the obtained ACs. According to the results obtained, it was determined that AC-800 had LARGER surface area and micropore volume than raw peanut shell. Namely, while raw FK HAS 500.275 m^2/g, AC-800 has a BET surface area of 2093.063 m^2/g. On the other hand, while raw FK has a micropore volume of 0.426 cc/g and a micropore surface area of 1199.900 m^2/g; AC-800 has a micropore volume of 1.053 cc/g and a surface area of 2963.759 m^2/g micropores. In order to obtain this porous structure, the thermal decomposition took place in the range of about 87 to 350-500 °C. The porosity structure of the obtained AC could be observed by SEM. With these properties, it was determined that ACs obtained by applying appropriate activation and carbonization conditions are superior to the raw material FK. It is thought that these applied conditions are suitable for the production of ACs with high surface area and micropore volume from other waste materials.

REFERENCES

1. M.A. Aly-Eldeen, A A.M. El-Sayed, M.S.A. Salem Dalia, G.M. El Zokm, *Egyp. J. Aq. Res.,* **44,** 179 (2018).
2. T. Fan, J. Zhao, Y. Chen, M. Wang, X. Wang, S. Wang, X. Chen, A. Lu, S. Zhao, *Adsorption Sci. Technol.*, 12 (2021).
3. S. D. Ashrafi, H. Kamani, H. S. Arezomand, N. Yousefi, A. H. K. H. Mahvi, *Desalin. Water Treat.,* **57**, 14051 (2015).
4. J. G. Shang, W. He, C. X. Fan, *Chin. J. Oceanol. Limnol.,* **33**, 169 (2015).
5. H. Gupta, B. Gupta, *Desalin. Water Treat,* **57**, 9498 (2015).
6. J.C. Moreno-Piraján, L. Giraldo, *Coden Echo E-J. Chem.,* **9**, 926 (2012).
7. M.H. Salmania, M. Miria, M.H. Ehrampousha, A. Alahabadib, A. Hosseini-Bandegharaei, *Desalin. Water Treat.,* **82,** 157 (2017).
8. N. Rattanachueskul, A. Saning, S. Kaowphong, N. Chumha, L. Chuenchom, *Biores. Technol.,* **226,** 164 (2016).
9. M. C. Tonucci, L. V. A. Gurgel, S. F. D. Aquino, *Ind. Crop Prod.,***74,** 111 (2015).
10. H. Dolas, O. Sahin, D. C. Saka, *Chem. Eng. J.,* **166,** 191 (2010).
11. R.X. Tang, Dai, C. Li, W.H. Liu, S.T. Gao, C. Wang, *J. Chem.*, 1 (2017).
12. R. Lopez-Cabeza, B. Gamiz, J. Cornejo, R. Celis, *Geoderma,* **293,** 64 (2017).
13. K. Gergova, N. Petrov, S. Eser, *Carbon,* **32**, 693 (1994).
14. S. Brunauer, P. H. Emmett, E. Teller, *JACS,* **60,** 309 (1938).
15. M.M. Dubinin, E.D. Zaverina, L.V. Radushkevich, *Zh. Fiz. Khim.,* **21,** 1351 (1947).
16. E.P. Barrett, L.C. Joyner, P.H. Halenda, *J. Am. Chem. Soc.,* **73,** 373 (1951).
17. A.C. Lua, T. Yang, *J. Colloid Interface Sci.,* **290**, 505 (2005).

Possible reaction pathways of selected organophosphorus and carbamate pesticides according to the DFT calculation method

B. Eren[1*], Y. Y. Gurkan[2]

[1]Tekirdag Namik Kemal Üniversity, Faculty of Agriculture, Tekirdag, Turkey
[2]Tekirdag Namik Kemal Üniversity, Departmen of Chemistry, Tekirdag, Turkey

This research was carried out in order to analyse the reactions of three organophosphorus (OP) and three carbamate (CB) pesticides with the hydroxyl radical (.OH), and their degradation paths. The studied organophosphorus pesticides are Azamethiphos, Coumaphos, Temephos, and the carbamate pesticides are Methiocarb, Carbofuran, Pirimicarb. Initially, in the reactions, the initial geometries of the reactants were determined. Geometric optimisations were performed using the DFT/B3LYP/6-31G (d) basic set of Quantum Mechanical Density Functional Theory (DFT). For each molecule, degradation reaction mechanisms were tried to be clarified using the calculated energy values. Since the reactions of pesticides with .OH are essential in terms of both water treatment and atmospheric chemistry, energy values were calculated both at gaseous phase and aqueous phase by modelling the solvent effect. For each molecule, fragments were found out by analysing the bond lengths, bond angles, and energy values, and as a result, degradation paths were determined.

Keywords: Organophosphorus pesticides, Carbamate pesticides, DFT

INTRODUCTION

Organophosphorus compounds have become the most widely used insecticides after the use of chlorinated hydrocarbons were restricted and banned due to the problems they caused. As a chemical structure, organophosphorus insecticides (OPs) are the esters of phosphoric acid (H_3PO_4). Methoxy (OCH_3) or ethoxy (OC_2H_5) are usually bound to the phosphorus atom as two ester groups. The third ester group may be aliphatic, homocyclic, or heterocyclic, and can be bound to the phosphorus atom *via* ester (P-O-R) or thioester (P-S-R) bonds. This weak bond increases the electrophyllic property of the phosphorus atom, and brings in the electron withdrawing property. Physicochemical properties of active agents in different subgroups such as evaporation, water solubility, penetration into plant tissues, and their movement within plant tissues vary considerably. It is stated that this change mainly results from P = 0 or P = S structure, and also from organic structures from the third ester group. The persistence of OPs in nature is short due to their rapid degradation. These pesticides degrade quickly, thus do not lead to long-term damage; however, besides they kill the non-target insects they also harm both people and nature. In addition, since they do not have a stable structure, they are used frequently. Therefore, they are considered costly [1-9].

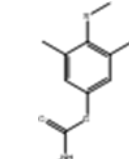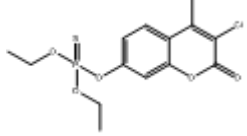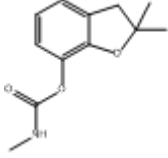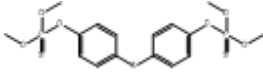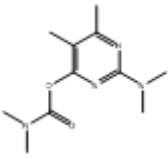Carbamate pesticides (CBs) are able to transform into various products through oxidation, biotransformation, hydrolysis, biological growth, photolysis, biological degradation, as well as through metabolic reactions in living organisms [10]. Besides the ability to metabolise CBs, microbial populations can also make themselves congruent with many of the metabolites of CBs. These pesticides and their metabolites may affect the microflora and also the soil fertility. Although CBs are very stable at aqueous environments, the administration of these toxic compounds may lead to a considerable decrease in non-target organisms [11]. The main problem in the use of CBs is that they remain in the environment for a long time. Due to their high water solubility, their residues are able to circulate in aqueous environments by percolation from soil to soil or to surface waters. Moreover, their wide application in agriculture increases their residues in environmental matrices [12].

The two-dimensional figures, molecule names, abbreviations that will be used hereafter and molecule formulas of the six molecules analyzed in this research are given in Table 1. The pesticides were analyzed initially in terms of their structures: It is possible to analyse the OPs, which are organophosphorus, according to how sulfur, oxygen, nitrogen, and carbon atoms are bound. While methoxy was bound as two ester groups to P atom in OP1 and OP3 molecules, ethoxy was bound as two ester groups to P atom in OP2 molecule. There is P=O bond in OP1 while there is P= S instead of P=O in OP2 and OP3 molecules.

Table 1. Two-dimensional figures, molecule names, abbreviations and molecule formulas of the studied molecules.

Two-dimensional figure	Molecule name and formula	Two-dimensional figure	Molecule name and formula
	(OP1) Azamethiphos $C_9H_{10}ClN_2O_5PS$		(CB1) Methiocarb $C_{11}H_{15}NO_2S$
	(OP2) Coumaphos $C_{14}H_{16}ClO_5PS$		(CB2) Carbofuran $C_{12}H_{15}NO_3$
	(OP3) Temephos $C_{16}H_{20}O_6P_2S_3$		(CB3) Pirimicarb $C_{11}H_{18}N_4O_2$
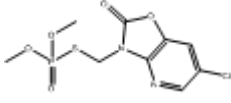
Since there are three O atoms and one S atom in all three molecules, all three OPs are called thiophosphates. Out of these three OPs, OP3 has a symmetric structure.

CBs, which are called carbamate compounds, and are carbamic acid esters, constitute a smaller group compared to the OPs. They are composed of a carboxyl (COO) instead of a hydrogen atom bound to an amine (NH_2) resulting in H_2N-COO-R structure. While there is one methyl group bound to N in CB1 and CB2 molecules, it is remarkable that there are two methyl groups bound to N in CB3 molecule. In all three molecules the R groups are different within H_2N-COO-R molecule structure.

All of the studied molecules are organic compounds, and it is known that organic pollutants are found in waters at low concentration levels. Biomolecules, which are hydroxyl radical scavengers and are various in terms of velocity, are specific detectors for hydroxyl radicals due to their hydroxylation capabilities. An attack of a hydroxyl radical to an aromatic compound leads to formation of a hydroxylated product, thus may be more dangerous than the original product at the beginning of the process. Therefore, it is essential that these products be observed [13].

METHODOLOGY

Theoretically, in order to determine all possible reaction paths of pesticides, geometric optimisations were perfofmed using the DFT/B3LYP/6-31G (d) basic set of Quantum Mechanical Density Functional Theory (DFT). In all molecular orbital calculations, energy values were calculated, and geometric optimisations were made by using Gauss View 5.0.8 molecular display programme and Gaussian 09 programme. Gauss View5.0.8 visualizes the molecules for the use of the Gaussian packaged software, and enables the rotation, movement, or any change of the molecules. It also permits the researcher to analyse all the calculated results of the Gaussian programme graphically [14]. The energy of the decomposition reaction of all organic compounds is affected by the water molecules in aqueous medium. In addition, the geometry stretch in the solutions is induced by H_2O. In other words, the presence of dielectric environment such as H_2O leads to geometric relaxation, and this results in an energy decreasing, and stabilising effect for the mechanism [13]. Therefore, in order to explain the solvent impact of H_2O on pesticide + ·OH reaction in this study, COSMO (conductor-like screening solvation model) within the Gaussian 09 packaged software was used [14]. Since the fate in the nature of the analysed three organophosphorus and three carbamate pesticides is important in terms of both atmospheric chemistry and water chemistry, the energy values in Table 2 and Table 3 are given in both aqueous and gaseous phases. Since the data obtained in atomic mass units when converted to kcal/mol unit started to differ from each other on the seventh digit, the results were given completely without rounding up the numbers. The bond lengths and bond angles given in the tables, which are apparently bigger, are highlighted as bold characters.

THEORETICAL RESULTS
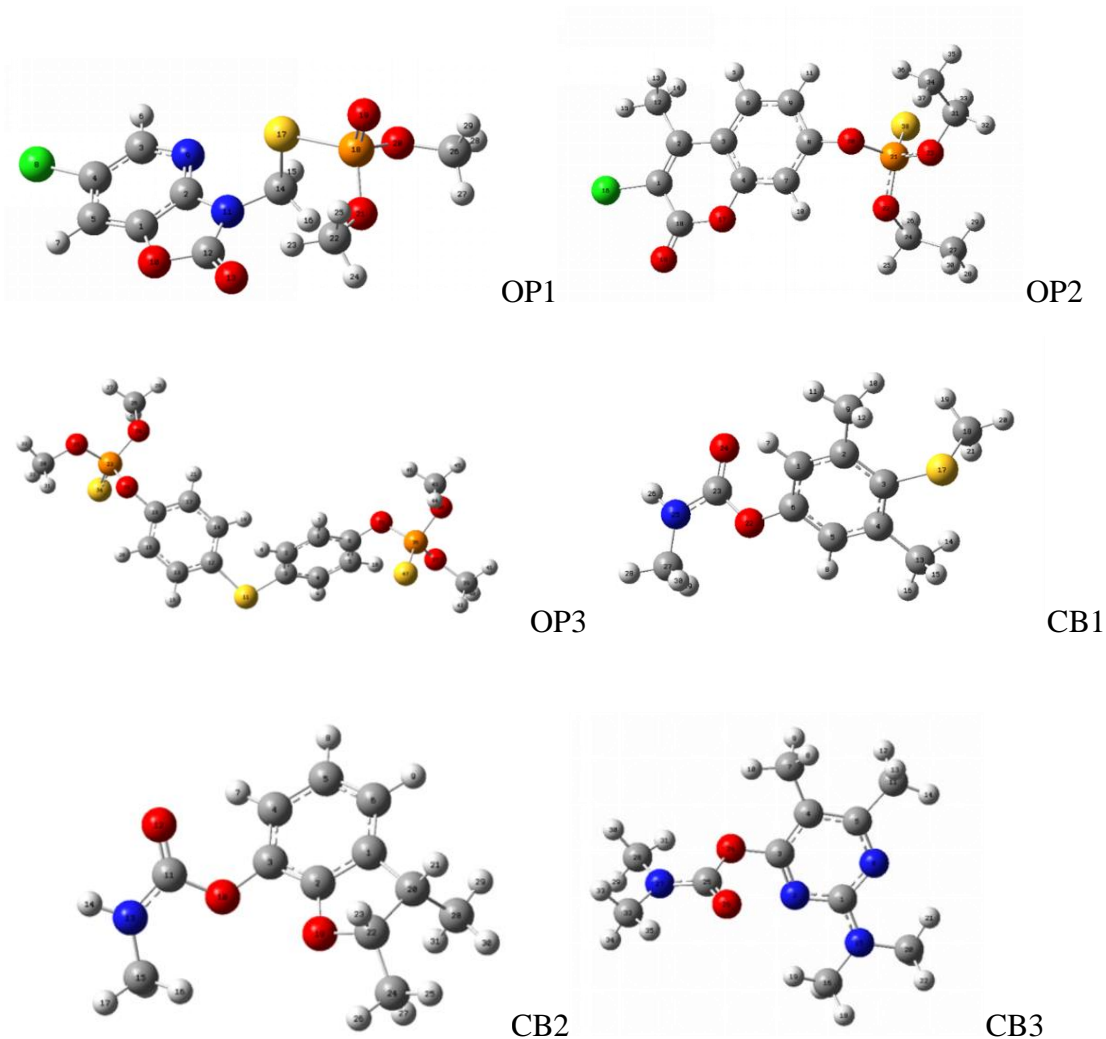
Figure 1. Optimized geometric structures of the studied molecules with DFT method (grey, C; white, H; blue, N; red, O; green, C; yellow, S; orange, P).

Table 2. Energy values of the gaseous and aqueous phases of OPs, and bond lengths and bond angles of atoms within OPs.

|	Gaseous phase (kcal/mol)	Aqueous phase (kcal/mol)	Bond length	(Å)	Bond angle	(°)
OP1	-1,276,474.519 -1,276,473.927 -1,276,518.746	-1,276,484.148 -1,276,483.556 -1,276,529.022	O_{21}-C_{22} O_{20}-P_{18} O_{21}-P_{18} S_{17}-P_{18} S_{17}-C_{14} N_{11}-C_{14} O_{20}-C_{26}	1.44823 1.61186 1.61665 **2.10137** **1.86825** 1.43993 1.44569	$C_{26}O_{20}P_{18}$ $O_{20}P_{18}O_{21}$ $P_{18}O_{21}C_{22}$ $S_{17}P_{18}O_{21}$ $C_{14}S_{17}P_{18}$ $N_{11}C_{14}S_{17}$	**118.59736** 99.44751 **119.67896** 107.77915 100.93849 111.14930
OP2	-1,329,539.807 -1,329,539.214 -1,329,589.227	-1,329,549.935 -1,329,549.343 -1,329,599.736	**Cl_{16}-C_1** C_{12}-C_2 O_{20}-C_8 **O_{20}-P_{21}** **S_{38}-P_{21}** **O_{23}-P_{21}**	**1.74557** 1.50422 1.38960 **1.63745** **1.93952** **1.60469**	$O_{22}C_{24}C_{27}$ $O_{23}C_{31}C_{34}$ $O_{22}P_{21}S_{38}$ $O_{23}P_{21}S_{38}$ $O_{20}P_{21}O_{22}$ $O_{20}P_{21}O_{23}$	111.55491 111.64910 **117.86055** **117.57544** 99.98248 99.81860

			Bond length	(Å)	Bond angle	(°)
			O₂₂-P₂₁	**1.60503**	C₈O₂₀P₂₁	122.55848
			O₂₂-C₂₄	1.45472	**O₂₀P₂₁S₃₈**	**116.43632**
			C₂₄-C₂₇	1.51907		
			O₂₃-C₃₁	1.45341		
			C₃₁-C₃₄	1.51927		
OP3	-1,851,213.200 -1,851,212.608 -1,851,276.348	-1,851,225.391 -1,851,224.798 -1,851,288.619	O₃₇-C₃₉	1.44123	C₄₃O₃₈P₃₆	120.76411
			O₃₈-C₄₃	1.43965	C₃₉O₃₇P₃₆	120.56106
			O₃₈-P₃₆	1.61018	C₆O₃₅P₃₆	**123.21190**
			O₃₇-P₃₆	1.60977	O₃₅ P₃₆S₄₇	117.32956
			S₄₇-P₃₆	**1.93700**	S₄₇P₃₆O₃₈	117.40393
			O₃₅-P₃₆	1.62704	C₃₀O₂₅P₂₃	120.79832
			O₆-O₃₅	1.39693	C₂₆O₂₄P₂₃	120.28954
			S₁₁-C₃	1.79378	O₂₄ P₂₃O₂₂	100.46100
			S₁₁-C₁₂	1.79393	S₃₄ P₂₃O₂₂	117.52168
			O₂₅-C₃₀	1.43951	P₂₃O₂₂C₁₉	**124.60188**
			O₂₄-C₂₅	1.44147	C₁₂S₁₁C₃	103.30950
			O₂₄-P₂₃	1.61068		
			O₂₅-P₂₃	1.61038		
			S₃₄-P₂₃	**1.93616**		
			O₂₂-P₂₃	1.62655		
			O₂₂-C₁₉	1.39522		

Table 3. Energy values of the gaseous and aqueous phases of CBs, and bond lengths and bond angles of atoms within CBs.

	Gaseous phase (kcal/mol)	Aqueous phase (kcal/mol)	Bond length	(Å)	Bond angle	(°)
CB1	-647,184.4656 -647,183.8726 647,224.4561	-647,190.0072 -647,189.4148 -647,230.3271	N₂₅-C₂₇	1.45499	**C₂₇N₂₅C₂₃**	**126.20337**
			N₂₅-C₂₃	1.36217	N₂₅C₂₃O₂₂	109.57643
			O₂₂-C₂₃	1.37696	C₂₃O₂₂ C₆	120.62380
			O₂₂-C₆	1.39141	C₁₈S₁₇C₃	101.01669
			S₁₇-C₁₈	**1.83693**	S₁₇C₃C₄	119.64032
			S₁₇-C₃	**1.80236**	**C₃C₄C₁₃**	**122.31470**
			C₄-C₁₃	1.51156	C₅C₄C₁₃	118.94762
CB2	-468,420.1723 -468,419.5800 -468,457.6359	-468,428.6023 -468,428.0093 -468,466.1173	**N₁₃-C₁₅**	**1.45464**	**C₁₅N₁₃C₁₁**	**126.26617**
			N₁₃-C₁₁	1.36116	N₁₃C₁₁O₁₀	109.50848
			O₁₀-C₁₁	1.37639	C₁₁O₁₀C₃	119.94145
			O₁₀-C₃	1.38867	C₁C₂₀C₂₈	111.71001
			C₂₂-C₂₄	**1.51697**	O₁₉C₂₂C₂₄	108.41780
			C₂₀-C₂₈	**1.53876**	C₂₀C₂₂C₂₄	118.30637
			O₁₉-C₂₂	**1.46116**	C₂₂C₂₀C₂₈	115.53466
CB3	-501,498.9604 -501,498.3680 -501,543.1276	-501,505.8385 -501,505.2455 -501,549.6004	**N₂₇-C₂₈**	**1.45428**	C₂₀N₁₅C₁	121.76976
			N₂₇-C₃₂	**1.45430**	C₁N₁₅C₁₆	121.43061
			N₂₇-C₂₅	1.36415	C₂₀N₁₅C₁₆	116.28654
			O₂₆-C₂₅	1.21252	C₂₅N₂₇C₂₈	124.91824
			O₂₄-C₂₅	1.38970	C₃₂N₂₇C₂₈	116.57136
			O₂₄-C₃	1.38378	C₃₂N₂₇C₂₈	116.57136
			N₁₅-C₂₀	**1.45156**	N₂₇C₂₅O₂₄	110.73159
			N₁₅-C₁₆	**1.45190**	**O₂₄C₂₅O₂₆**	**123.22908**
			N₁₅-C₁	1.37002	**N₂₇C₂₅O₂₆**	**125.97465**
			C₅-C₁₁	**1.50775**	C₂₅O₂₄C₃	117. 6189
			C₄-C₇	**1.50604**		

Table 4. Energy values of fragments of OP molecules in gaseous phase.

OP	Gaseous phase (kcal/mol)	OP	Gaseous phase (kcal/mol)	OP	Gaseous phase (kcal/mol)
OP1	$\Delta E = -1{,}276{,}474.519$ $\Delta H = -1{,}276{,}473.927$ $\Delta G = -1{,}276{,}518.746$	OP2	$\Delta E = -1{,}329{,}539.807$ $\Delta H = -1{,}329{,}539.214$ $\Delta G = -1{,}329{,}589.227$	OP3	$\Delta E = -1{,}851{,}213.200$ $\Delta H = -1{,}851{,}212.608$ $\Delta G = -1{,}851{,}276.348$
$OP1_1$	-1,251,829.351 -1,251,828.758 -1,251,828.758	$OP2_1$	-1,304,885.400 -1,304,884.808 -1,304,933.008	$OP3_1$	-1,826,567.746 -1,826,567.153 -1,826,627.826
$OP1_2$	-1,252,288.284 -1,252,287.691 -1,252,325.969	$OP2_2$	-1,280,118.360 -1,280,230.069 -1,280,276.369	$OP3_2$	-1,801,922.162 -1,801,921.570 -1,801,980.884
$OP1_3$	-963,425.967 -963,425.374 -963,464.772	$OP2_3$	-1,280,239.707 -1,280,239.115 -1,280,284.604	$OP3_3$	-1,801,922.622 -1,801,922.029 -1,801,980.023
$OP1_4$	-988,081.157 -988,080.564 -988,123.768	$OP2_4$	-1,280,231.280 -1,280,230.688 -1,280,276.632	$OP3_4$	-1,050,909.013 -1,050,908.421 -1,050,948.843
$OP1_5$	-596,452.829 -596,452.236 -596,478.917	$OP2_5$	-1,041,138.508 -1,041,137.915 -1,041,185.763	$OP3_5$	-1,752,631.045 -1,752,630.453 -1,752,684.711
$OP1_6$	-308,049.323 -308,048.730 -308,073.243	$OP2_6$	-1,304,885.648 -1,304,885.056 -1,304,933.369	$OP3_6$	-1,243,036.585 -1,243,035.993 -1,243,084.858
$OP1_7$	-621,105.140 -621,104.548 -621,134.006	$OP2_7$	-1,016,484.104 -1,016,483.511 -1,016,529.431	$OP3_7$	-634,859.235 -634,858.642 -634,894.182
$OP1_8$	-870,967.493 -870,966.900 -870,998.630	$OP2_8$	-1,016,483.333 -1,016,482.740 -1,016,529.052	$OP3_8$	-1,777,276.851 -1,777,276.258 -1,777,332.407
$OP1_9$	-1,132,742.293 -1,132,741.700 -1,132,777.662	$OP2_9$	-1,255,576.546 -1,255,575.954 -1,255,620.102	$OP3_{21}$	-1,754,705.068 -1,754,704.476 -1,754,761.596
$OP1_{10}$	-963,441.125 -963,440.532 -963,477.748	$OP2_{10}$	-1,230,930.996 -1,230,930.404 -1,230,971.800	$OP3_{22}$	-1,707,485.222 -1,707,484.629 -1,707,539.171
$OP1_{11}$	-1,204,609.012 -1,204,608.420 -1,204,648.722	$OP2_{11}$	-1,206,285.055 -1,206,284.463 -1,206,323.472	$OP3_{23}$	-1,195,840.766 -1,195,840.173 -1,195,888.033
$OP1_{12}$	-938,785.100 -938,784.508 -938,820.472	$OP2_{12}$	-672,054.408 -672,053.815 -672,085.640	$OP3_9$	-540,468.308 -540,467.716 -540,499.397
$OP1_{13}$	-891,565.651 -891,565.058 -891,599.512	$OP2_{13}$	-624,858.313 -624,857.721 -624,887.961	$OP3_{51}$	1,705,413.934 -1,705,413.342 -1,705,465.073
$OP1_{14}$	-844,339.253 -844,338.661 -844,372.455			$OP3_{52}$	-1,658,196.793 -1,658,196.200 -1,658,246.328

**Table 5.** Energy values of fragments of CB molecules at gaseous phase.

| CB	Gaseous phase (kcal/mol)	CB	Gaseous phase (kcal/mol)	CB	Gaseous phase (kcal/mol)
CB1	ΔE= -646,961.779 ΔH= -647,183.873 ΔG= -647,224.456	CB2	ΔE= -468,420.172 ΔH= -468,419.580 ΔG= -468,457.636	CB3	ΔE = -501,498.960 ΔH = -501,498.368 ΔG = -501,543.128
CB1$_1$	-622,534.677 -622,534.084 -622,571.718	CB2$_1$	-443,769.090 -443,768.498 -443,803.804	CB3$_1$	-476,849.737 -476,849.145 -476,891.558
CB1$_2$	-622,531.874 -622,531.282 -622,569.784	CB2$_2$	-443,766.239 -443,765.647 -443,802.036	CB3$_2$	-476,851.211 -476,850.618 -476,892.847
CB1$_3$	-622,532.928 -622,532.335 -622,570.695	CB2$_3$	-419,114.956 -419,114.363 -419,147.993	CB3$_3$	-476,846.201 -476,845.608 -476,888.095
CB1$_4$	-597,881.471 -597,880.879 -597,916.436	CB2$_4$	-394,462.904 -394,462.312 -394,494.120	CB3$_4$	-476,836.756 -476,836.164 -476,877.675
CB1$_5$	-587,878.743 -597,878.151 -597,914.624	CB2$_5$	-288,617.636 -288,617.670 -288,642.136	CB3$_7$	-476,851.211 -476,850.618 -476,892.842
CB1$_6$	-597,883.246 -597,882.653 -597,917.775	CB2$_6$	-241,425.820 -241,425.227 -241,448.596	CB3$_8$	-452,202.855 -452,202.263 -452,241.368
CB1$_7$	-573,227.718 -573,227.125 -573,261.071			CB3$_6$	-452,189.581 -452,188.988 -452,228.523
CB1$_8$	-323,363.666 -323,363.074 -323,393.491			CB3$_9$	-417,469.381 -417,468.789 -417.506,179
CB1$_9$	-298,712.157 -298,711.564 -298,739.598			CB3$_{10}$	-392,820.116 -392,819.523 -392,855.204
CB1$_{10}$	-442,728.940 -442,728.348 -442,752.493			CB3$_{11}$	-368,174.342 -368,173.750 -368,206.206
CB1$_{11}$	-395,536.578 -395,535.985 -395,558.810			CB$_{35}$	-346,360.378 -346,359.785 -346,393.973
CB1$_{12}$	-192,864.522 -192,863.930 -192,885.827			CB3$_{12}$	-262,331.250 -262,330.658 -262,357.466
CB1$_{13}$	-145,672.144 -145,671.552 -145,692.129			CB3$_{13}$	-165,814.401 -165,813.808 -165,834.192
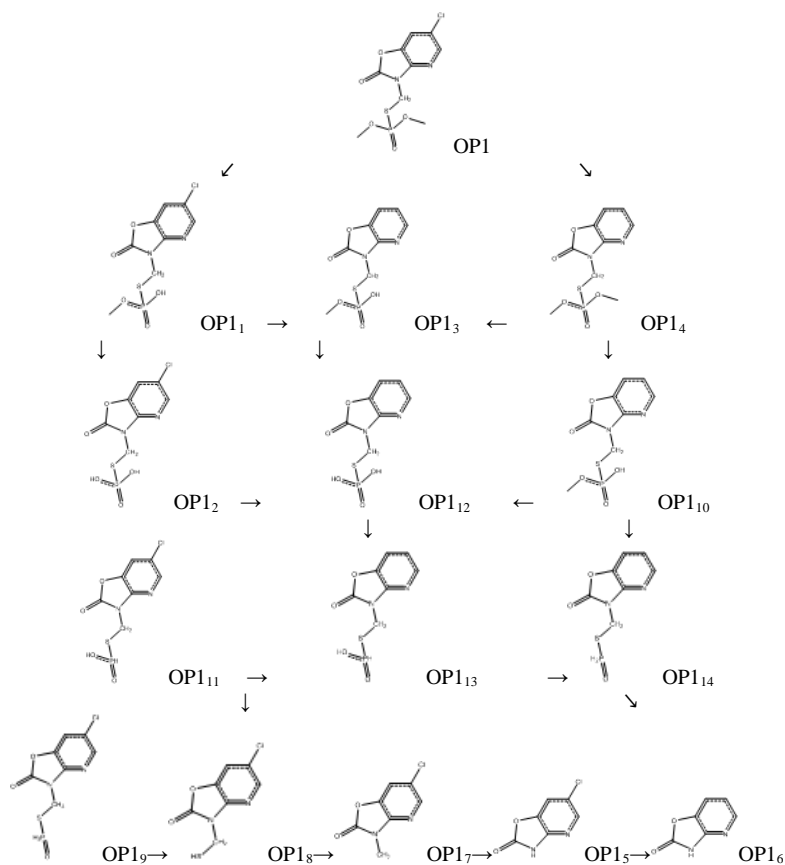
Figure 2. Degradation mechanism of OP1 molecule.
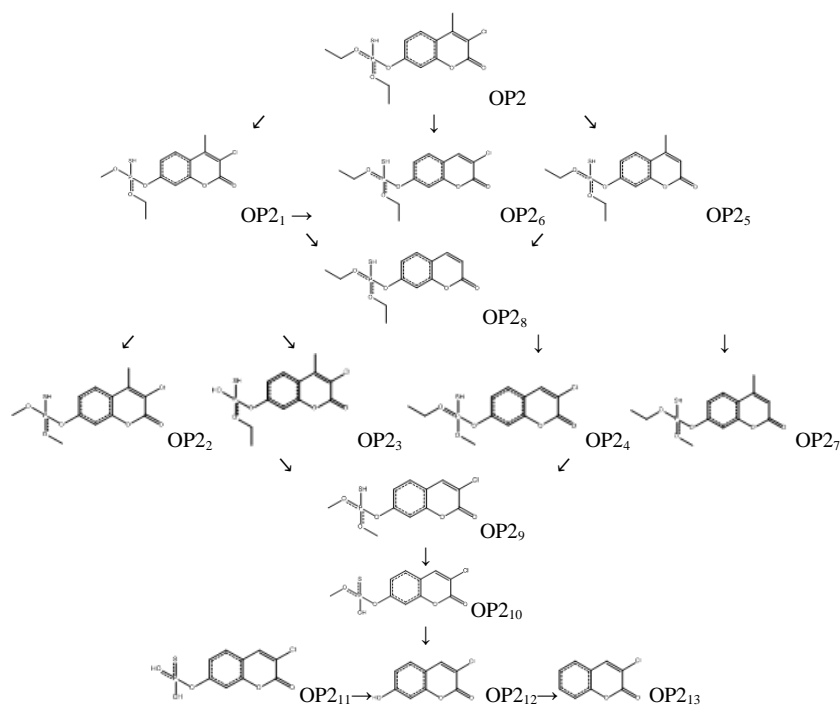
Figure 3. Degradation mechanism of OP2 molecule.
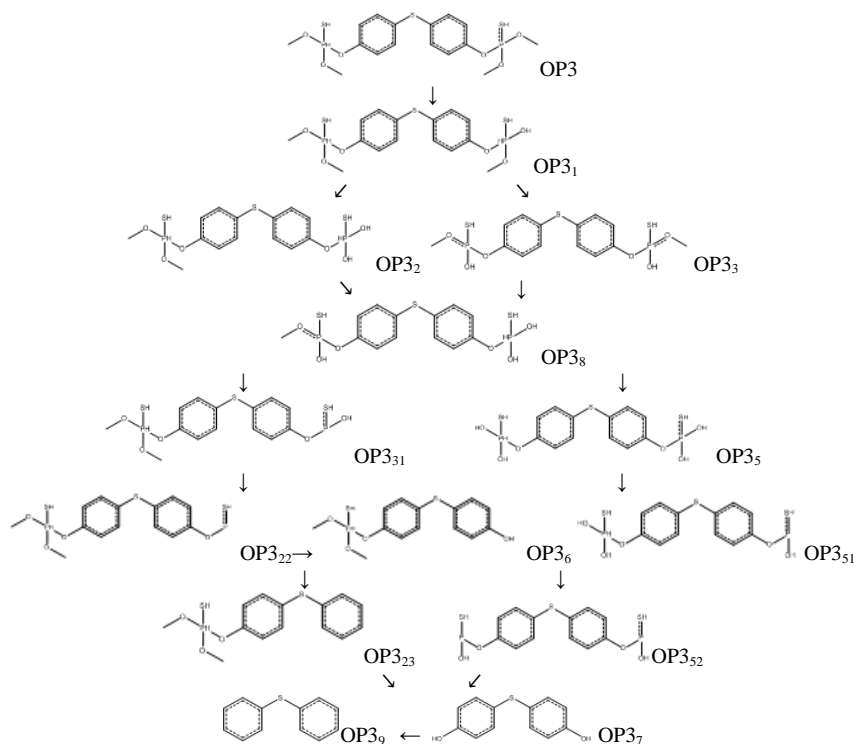
Figure 4. Degradation mechanism of OP3 molecule.
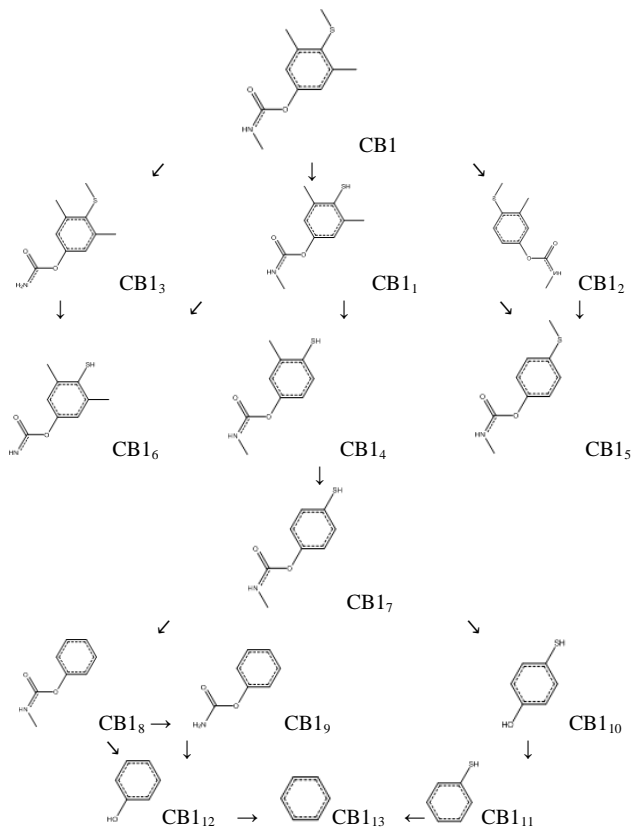
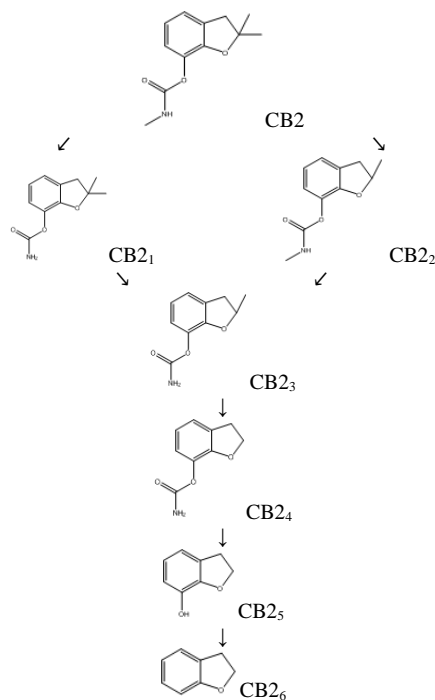**Figure 5.** Degradation mechanism of CB1 molecule.
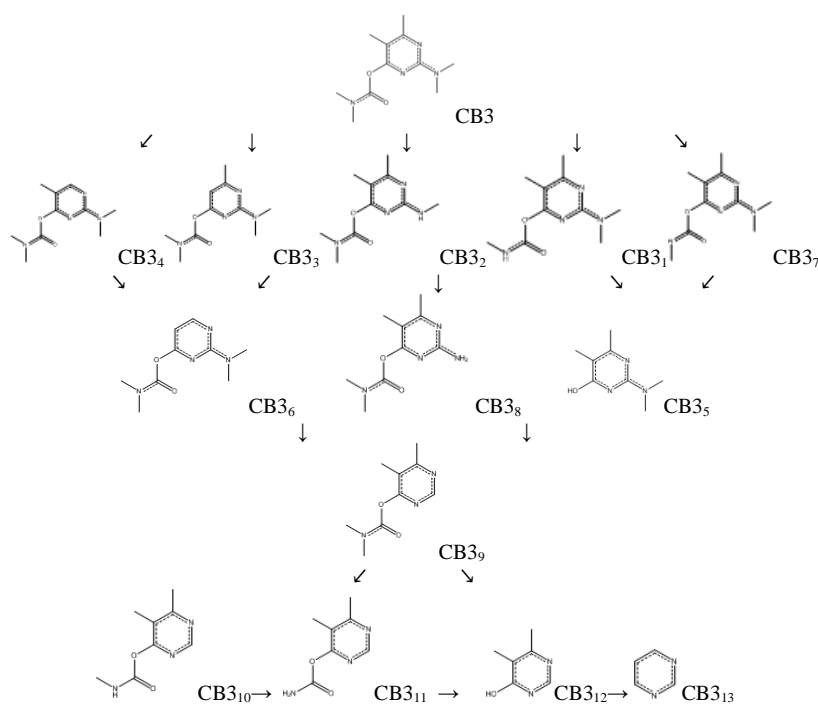
Figure 6. Degradation mechanism of CB2 molecule.

Figure 7. Degradation mechanism of CB3 molecule

CONCLUSION

While the degradation mechanism was obtained for each molecule, bond lengths and bond angles of all atoms within all molecules and energy values of each fragment were analyzed individually, it was tried to make estimations starting from the one with the lowest energy, in other words, the most spontaneous fragment; also considering the ones with the longest bond length, and the one with the widest bond angle, or the most stable structures

bound with double bonds. In order to exemplify what has been considered during these estimations, below there are explanations for one sample for each pesticide group, namely OP1 and CB1.

O_{19} and O_{13} in OP1, as also seen in Figure 1, form double bonds with P_{18} and C_{12} atoms, respectively. Since these bonds are stable, they are not expected to break. Bond lengths of O_{21}-C_{22} and O_{20}-C_{26} in Table 2 are 1.44823 Å; 1.44569 Å, respectively. Again in the same Table, the first and second wide

bond angles are the ones of $P_{18}O_{21}C_{22}$ with the bond angle 119.67896^0, and the ones of $P_{18}O_{20}C_{26}$ with the bond angle 118.59736^0. In the light of this information, the methyl groups including C_{26} and C_{22} atoms are expected to break. Whether the methyl groups were the first of the fragmentation paths was determined by analysing their energy values. The $OP1_1$ and $OP1_2$ fragments in Figure 2 confirm this prediction. N_{11} is an electronegative atom. When the space surrounded by this atom was observed, it was found that N_{11}-C_{14} in Table 2 has a bond length of 1.43993 Å, and since there are longer bond lengths than this one, it was predicted that if there were to be any bond break there, it would be subsequent to the break of the other bonds. In Figure 2, the degradation of the N-bond in the final stages of the cleavage pathway proves this thesis. The bond lengths of S_{17}-P_{18} and S_{17}-C_{14} in Table 2 are the longest bonds in the molecule with 2.10137 Å; 1.86825 Å respectively. When the bond formed by S breaks, phosphate will leave the molecule. In Table 4, energy values of the fragments at gaseous phase were analysed. The degradation path for OP1 in Figure 2 was determined starting from the fragment with the lowest energy level, in other words, from the most spontaneous fragment, considering both the above given predictions and the energy values for each fragment given in Table 4.

O_{22} in CB1 molecule given in Figure 1 is an electronegative atom. When the space surrounded by this atom was observed, it was found out that the $C_{23}O_{22}C_6$ bond angle was 120.62380^0, O_{22}-C_{23} bond length was 1.37696 Å, and O_{22}-C_6 bond length was 1.39141 Å as given in Table 3. Since in terms of bond angles there are wider angles than this, and since there are bond lengths longer than the above given one, if there were to be a bond break there, it would occur subsequent to the other bond breaks. The break from O_{22} in the molecule is in the final stage of degradation, as can be seen in Figure 5. As seen in Figure 1, since O_{24} is bound to C_{23} with a double bond, it is stable, and this bond is not expected to break. Although N_{25} is an electronegative atom, in Table 3, $C_{27}N_{25}C_{23}$ in its optimized form is the widest bond angle of the molecule with 126.20337^0. The bond length N_{25}-C_{27} is the longest with 1.45499 Å in the same table. We can understand from here that the methyl group $C27$ attached to $N25$ will break off in the first place. This bond length comes after the bond lengths made by S_{17} and C_4 atoms. The width of the bond angle competes with these bond lengths. For S_{17} atom, S_{17}-C_{18} bond in Table 3 is ready to break with the longest bond length in the molecule as 1.83693 Å. $C_3C_4C_{13}$ bond angle in the same table with 122.31470^0 is a

preview of a methyl group being ready to detach from the molecule. Methyl groups including C_9, C_{13}, C_{18}, C_{27} atoms are remarkable in terms of their first fragmentation paths. Predicting that the break will start here, energy values at gaseous phase of the fragments in Table 5 were analysed. First, methyl groups were detached one by one, and $CB1_1$, $CB1_2$, $CB1_3$ were obtained, then binary breakings were analysed, and $CB1_4$, $CB1_5$, $CB1_6$ fragments gained their place in the decomposition reaction. Starting with the fragment with the lowest energy level, in other words with the most spontaneous one, degradation path of CB1 was determined by both the above given predictions and by the analysis of the energy values given in Table 5 for each fragment.

DISCUSSION

Degradation mechanism for the six molecules, which were studied in this research were predicted, and are given in Figures 3-7, respectively. Due to having the lowest energy values, OP3 among organophosphorus pesticides, and CB1 among carbamate pesticides were determined to be the most spontaneous molecules to react. It is predicted that the reason of OP3 to react as the most spontaneous molecule among other molecules of its group is its having a symmetric structure. However, the reason of CB1 molecule to react as the most spontaneous molecule among its group is the R group within H_2N-COO-R molecular structure.

This study is compiled of the data obtained in the PhD dissertation, in which seven pesticides in total were analysed both theoretically and experimentally. Experimental and theoretical results for Phosmet, one of these seven pesticides, have been published [1]. The degradation reactions under the influence of light of the selected seven pollutants in aqueous TiO_2 suspensions were analysed experimentally as well. It was also established that when light and TiO_2 were in the same environment together, all the matters degraded to a large extent. The concentration changes at the end of 100 minutes were calculated as 78% for OP1, 85% for OP2, 76% for OP3, 87% for CB1, 95% for CB2, 94% for CB3. These results show that OP2 among organophosphorus pesticides, and CB2 among carbamate pesticides are the pesticides with the greatest degradation. According to the k rate constant, OP3 among organophosphorus pesticides, and CB1 among carbamate pesticides are the most rapid ones, since these two molecules have a greater constant rate among their own groups with 9.55 ± 0.006 10.35 ± 0.002, respectively, and thus react faster than the others. The experimental results also indicate that OP1 and CB3 molecules are the

most spontaneous ones during reaction among their own groups.

REFERENCES

1. B. Eren, Y. Yalçın Gürkan, *Bulgarian Chemical Communications*, **53** (4), 456 (2021).
2. R. Atkinson, S. M. Aschmann, M. A. Goodman, A. M. Winer, *Int. J. Chem. Kinet.,* **20**, 273 (1988).
3. M. A. Goodman, S. M. Aschmann, R. Atkinson, A. M. Winer, *Arch. Environ. Contam. Toxicol*., **17**, 281 (1988).
4. M. A. Goodman, S. M. Aschmann, R. Atkinson, A. M. Winer, *Environ. Sci. Technol.,* **22**, 578 (1988).
5. R. Atkinson, J. Arey, *Chem. Rev*., **103**, 4605 (2003).
6. S. M. Aschmann, E. C. Tuazon, R. Atkinson, *J. Phys. Chem. A*, **109**, 11828 (2005).
7. S. M. Aschmann, E. C. Tuazon, R. Atkinson, *J. Phys. Chem. A*, **109**, 2282 (2005).
8. S. M. Aschmann, R. Atkinson, *J. Phys. Chem. A,* **110**, 13029 (2006).
9. S. M. Aschmann, E. C. Tuazon, W. D. Long, R. Atkinson, *J. Phys. Chem. A*, **114**, 3523 (2010).
10. Z. Q. Cai, J. Wang, J. T. Ma, X. L. Zhu, J. Y. Cai, G. H. Yang, *Journal of Agricultural and Food Chem.,* **63,** 7151 (2015).
11. M. Gupta, S. Mathur, T.K. Sharma, M. Rana, A. Gairola, N. K. Navani, R. Pathania, *Journal of Hazardous Materials,* **301,** 250 (2016).
12. M. Sturini, E. Fasani, C. Prandi, A. Casaschi, A. Albini, *J. Photochem, Photobiol. A: Chem.,* **101**, 251 (1996).
13. B. Eren, Y. Yalçın Gürkan, *JSCS*, **82** (3), 277 (2017).
14. Gaussian 09, Revision B.04, Gaussian Inc., Pittsburgh, PA, (2009).

Relation of the grain size, petrophysical parameters, and Fourier transform infrared analysis of Kusuri sandstones in the Zonguldak subbasin of the West Black Sea, Turkey

A. Geçer

Department of Chemical Engineering, Engineering Faculty, Tandoğan Campus, Ankara University, 06100 Ankara, Turkey

The Zonguldak subbasin has recently attracted attention due to the identification of unexplored areas for hydrocarbon potential. Here, I present the first detailed reservoir investigation of Kusuri Formation sandstones in a well around Bartın, located in the Zonguldak subbasin of the West Black Sea. I employed an integrated approach that includes petrography, well logging, petrophysical analysis, and Fourier transform infrared analysis for reservoir characterization. The purpose of this study is to investigate the relation of the grain size, petrophysical parameters, and Fourier transform infrared analysis of Kusuri sandstones. The Kusuri Formation sandstones are divided into three groups based on their grain size using petrographic analyses. Group 1 is composed of 0.4-0.6 mm grains, group 2- of 0.3 mm grains, and group 3- of very fine grains (0.1-0.2 mm). Group 1 and group 2 sandstones of the Kusuri Formation exhibit medium-good petrophysical characteristics. The presence of hydrocarbons was determined using attenuated total reflection- Fourier transform infrared (ATR-FTIR) analysis. The results show that the Kusuri sandstone interval has medium-good reservoir properties and a high potential to produce hydrocarbons increasing the reserves in the study area.

Key words: Reservoir sandstone, well logs, grain size, petrophysical parameter, ATR-FTIR, hydrocarbon

INTRODUCTION

Zonguldak, Ulus, Devrek, Sinop, and Bolu subbasins, are parts of the West Black Sea Basin [1]. The Zonguldak subbasin extends between Ereğli and Amasra, parallel to the Black Sea. Currently, no studies have addressed the petroleum potential of the Zonguldak subbasin in the Western Black Sea region.

Hydrocarbons are produced from deltas in many parts of the world [2-7]. Kusuri Formation sandstones in the Zonguldak subbasin might have been deposited in a delta environment and the delta sandstones formed important oil reservoirs [8].

The Kusuri Formation is composed of dark gray shale and sandstone (Fig. 1). Well log data suggest that the thickness of the sediments in the Zonguldak subbasin is up to 8000 m. The thickness of the Kusuri Formation was measured as 3900 m in the Zonguldak subbasin [8]. The unit has reservoir rock features and contains porous sandstone.

This is the first study on a delta using well logs, petrographic, petrophysical properties, attenuated total reflectance-Fourier transform infrared (ATR-FTIR) spectroscopy analysis, and scanning electron microscopy-energy dispersive spectroscopy (SEM-EDS) analyses in the Kusuri Formation.

In this study, the reservoir characteristics of the Kusuri Formation sandstones in a well drilled in the Zonguldak subbasin (around Bartın), were investigated.

The aim of the study is to (1) determine the grain size of the Kusuri Formation sandstones, (2) evaluate the petrophysical parameters (porosity and permeability) of the sandstones, (3) well log interpretation, (4) determine the presence of organic matter (5) determine the clay minerals, and (6) determine the reservoir quality.

MATERIALS AND METHODS

Cores and logs from a well in the Zonguldak subbasin of the West Black Sea Basin were studied. Petrographic analysis was performed on 25 thin sections obtained from subsurface core samples. The grain size was measured using an optical microscope-ocular micrometer [9] from 20 thin sections by 300-point counts. Five core samples were analysed using a scanning electron microscope-energy dispersive spectrometer at the METU laboratories, Turkey. Porosity and permeability analyses to determine the reservoir rock quality of the Kusuri sandstones could not be performed using porosimeter and permeameter devices and cylindrical core samples due to the dispersive properties of the sandstones.
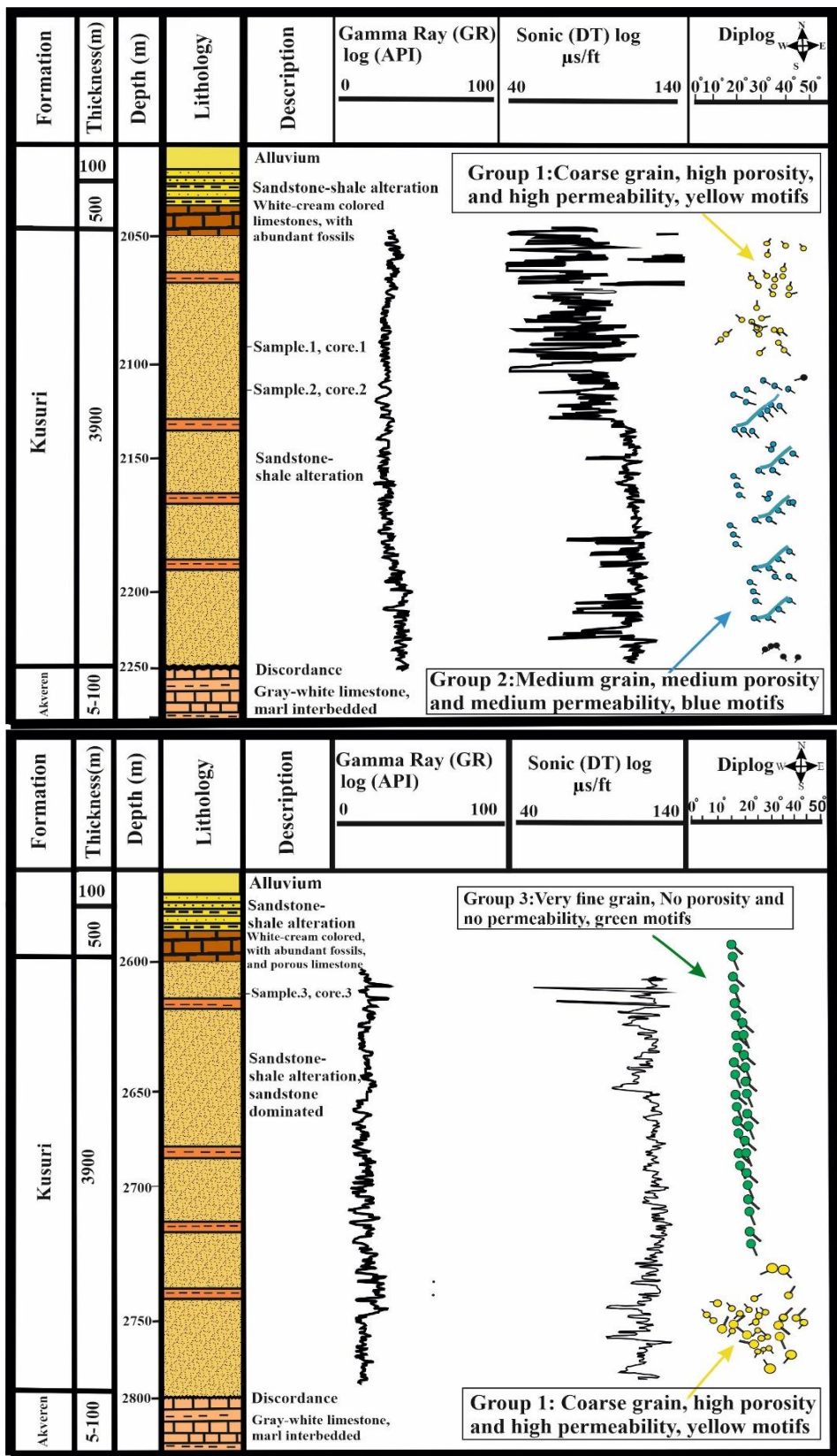

Fig. 1. Well logs (GR, DT, and Diplog) of the Kusuri Formation sandstones

Porosity and permeability were determined by Sonic logs only. The presence of hydrocarbons can be determined using FTIR analysis [10, 11]. The samples from the Zonguldak subbasin were analyzed

using the ATR-FTIR method in this study for the first time. FTIR analysis was performed on core samples at the METU laboratories in Turkey.

Log measurements were performed in a well for the Kusuri sandstones in the studied basin (Fig. 1). Well logs were interpreted for a well of the West Black Sea, and the data were used to determine depositional characteristics, namely, laminations, grading, grain size, porosity, and permeability of the reservoir sandstones [8].

The reservoir properties of Kusuri sandstones were determined from gamma ray (GR), sonic (DT), and dipmeter (DIP) logs according to [12].

The shale (clay) volume V_{sh} in the Kusuri sandstones was calculated using the following equation [13]:

$$V_{sh} = \frac{GR_{log} - GR_{min}}{GR_{max} - GR_{min}} \qquad (1)$$

where GR_{log} is the average gamma ray log value, GR_{min} is the gamma ray minimum value, and GR_{max} is the gamma ray maximum value.

The effective porosity (ϕ_{ef}) of the Kusuri sandstones was calculated using the following equation [13]:

$$DT_{cor} = DT - \frac{V_{sh} * DT_{sh}}{(1 - V_{sh})} \qquad (2)$$

where DT_{cor} is the corrected sonic log value for shaley sand, DT is the sonic log value, V_{sh} is the shale volume, DT_{sh} is the sonic maximum value for the shale sand zone, and $DT_{cor} = \phi_{ef}$.

The permeability (K) of the Kusuri sandstones was calculated using Timur's equation [14] at irreducible water saturation as follows:

$$K(mD) = \frac{0.136 * \phi_{ef}^{4.4}}{S_w^2} \qquad (3)$$

where K is the permeability, ϕ_{ef} is the effective porosity, and S_w is the irreducible water.

Sandstone porosity was estimated using the sonic log of the well. Porosity can be determined using the sonic (DT interval transit time; microsec/ft) – porosity (ϕ_{ef}) crossplots [12].

In oil research, the sandstone grain size of rocks passing in a well can be determined by interpreting dipmeter logs [15]. These logs are indicated by pin-shaped symbols that vary depending on the depth in boreholes. The tip of the pin-shaped symbol indicates the direction of the dip, while the circular head of the pin gives the amount or angle of the dip. The displacement of the symbol to the right represents the magnitude of the dip angle.

In dipmeter logs, various symbols are named red, green, yellow or blue (Fig. 1). The amount of slope in the blue motif decreases depending on the depth and indicates the layers formed by medium grain sandstone. Mixed motifs inclined in all directions in the yellow motif indicate coarse grains such as conglomerate and sandstone. In green motifs, on the other hand, the amount of dip does not change, indicating a laminated low-energy environment such as very thin sandstones-shale according to [15] (Fig. 1).
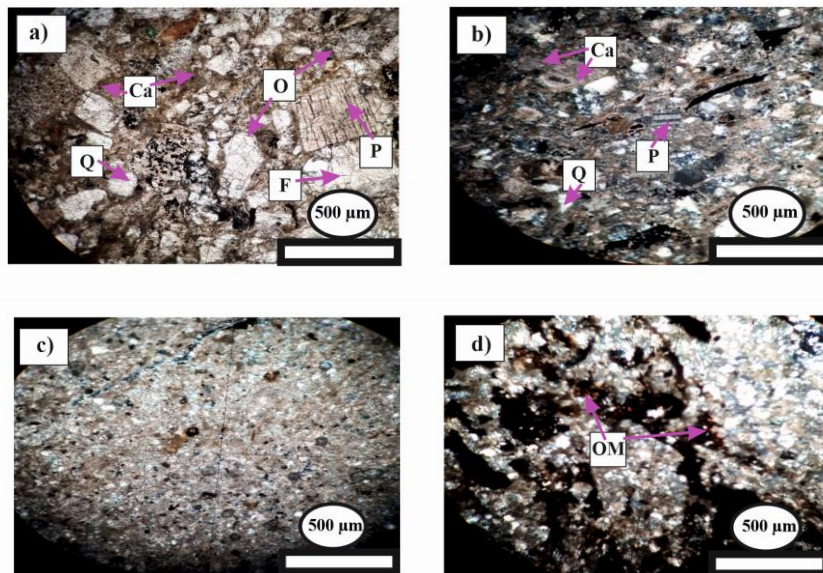
Fig. 2. Microphotographs of the Kusuri Formation sandstones. a) Group 1 sandstones Core number: 1. Depth: 2095.0 m b) Group 2 sandstones Core number: 2. Depth: 2115.0 m. c) Group 3 sandstones Core number: 3. Depth: 2610.0 m d) Organic matter smears (OM). Core number: 3. Depth: 2610.0 m. Double nicol.

RESULTS AND DISCUSSION

Petrographic analysis of the sandstones

Petrographic analysis of the Kusuri sandstones was performed on 25 thin sections obtained from core samples using optical microscopy. The Kusuri sandstones were divided into three groups based on their grain size using petrographic analyses. Group 1 contains medium-coarse grain sizes (0.4-0.6 mm) and medium well-sorted grains (Fig. 2a). Quartz (Q), orthoclase (O), plagioclase (P) minerals, fissure (F), carbonate cement (Ca, early calcite cement) are observed in the photograph. It is seen that the carbonate (Ca) mineral closes the pores (Fig. 2a).

Group 2 contains medium sized (0.3 mm) and medium-sorted grains (Fig. 2b). Quartz (Q) and plagioclase minerals (P) and carbonate cement (Ca, early calcite cement) are observed in the photograph (Fig. 2b).

Alternatively, group 3 has a very fine grain size (0.1-0.2 mm) (Fig. 2c) and does not exhibit reservoir features. In Fig. 2d, organic matter (OM) smears were observed.

Reservoir features of the sandstones

The porosity values of the Kusuri Formation sandstones are between 35% and 50% for Group 1 sandstones and 20-35% for Group 2 sandstones (Fig. 3). Similarly, permeability values range between 400-660 mD for Group 1 sandstones and 100-400 mD for Group 2 sandstones (Fig. 3).

Yellow motifs which show coarse grain in Dip logs have high porosity and high permeability. Blue motifs which denote medium grain in Dip logs have medium porosity and medium permeability. Green motifs which correspond to small grains show no porosity and no permeability (Fig. 1).

The Kusuri Formation Group 3 sandstones exhibit the worst reservoir characteristics, which is attributable to the very fine-grains, poorly sorted. In Group 1 and Group 2 sandstones, primary intergranular and mostly fractured crack porosities were dominant. Accordingly, it can be assumed that Group 1 and Group 2 have medium-good reservoir potential. Although the primary porosity decreases by closing the pores of early calcite cement and clay minerals (illite, kaolinite) (Fig. 4), fracturing of grains can be considered in positive terms of reservoir quality.

It can be said that the sandstones (Groups 1 and 2) of the Kusuri Formation are of medium to good quality, considering the grain size using petrographic properties, according to the porosity-permeability classification of Levorsen [16].

FTIR analyses

In this study, bituminous shale samples were analysed by FTIR spectroscopy using the ATR technique (Fig. 5). FTIR spectra were evaluated according to [17]. In the FTIR spectrum of the group 3 sample, structural hydroxyl peak at 3618 cm^{-1} was observed (Fig. 5a). The Si-O stretching of quartz was determined at 779 cm^{-1} and 798 cm^{-1}. Characteristic CO_3 peaks of calcite were observed at 712 cm^{-1} and 873 cm^{-1}. The peak at 462 cm^{-1} corresponds to Si-O-Si deformation. Aromatic C-H peaks were observed at 695 cm^{-1}, 984 cm^{-1}, and 1164 cm^{-1} (Fig. 5a).

The FTIR spectrum of the group 2 sample showed a structural hydroxyl peak at 3620 cm^{-1} (Fig.

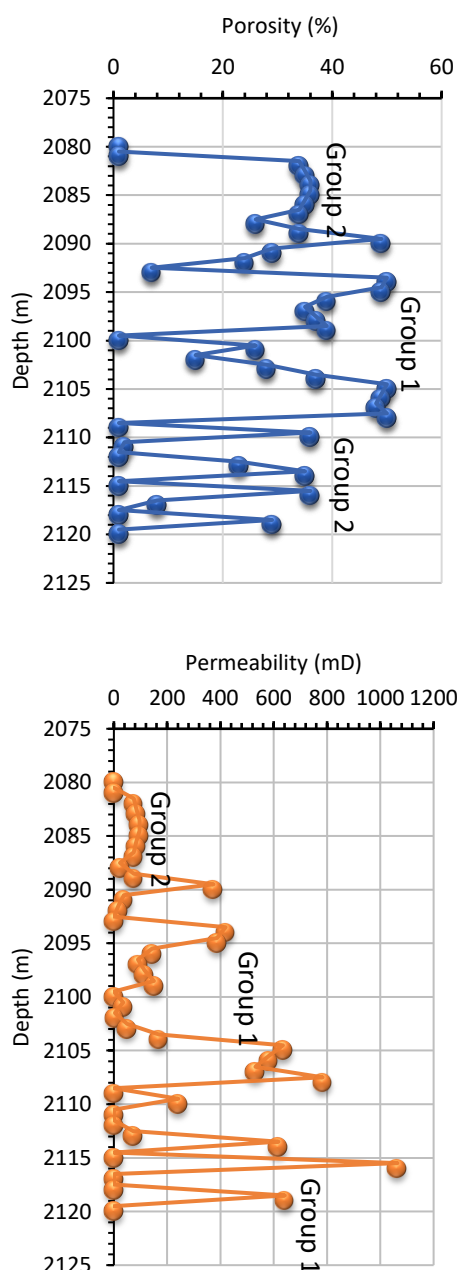**Fig. 3.** Porosity and permeability *versus* depth for Kusuri Formation sandstones

5b). Si-O stretching of quartz minerals was observed at 779 cm^{-1} and 798 cm^{-1}. The CO_3 peaks at 712 cm^{-1} and 873 cm^{-1} showed the presence of calcite. The peak at 462 cm^{-1} corresponds to Si-O-Si deformation. Aromatic C-H peak was observed at 992 cm^{-1}. The $CH=CH_2$ peaks of alkenes were observed at 1418 cm^{-1} and 1634 cm^{-1} (Fig. 5b).

In the FTIR spectrum of the group 1 sample, a structural hydroxyl peak at 3627 cm^{-1} was observed (Fig. 5c). Si-O stretching of quartz minerals was determined at 779 cm^{-1} and 798 cm^{-1}. The CO_3 peaks of calcite mineral were observed at 712 cm^{-1} and 873 cm^{-1}. The peak at 460 cm^{-1} corresponds to Si-O-Si deformation. Aromatic C-H bonds were observed (695 and 992 cm^{-1}). In addition, the $CH=CH_2$ peak of alkenes was observed at 1418 cm^{-1}. (Fig. 5c).

Aromatic C-H bonds are the main hydrocarbon functional groups in the FTIR spectra of the samples (Fig. 5). The permeabilities of Group 1 sample, Group 2 sample, and Group 3 sample were 550 mD, 350 mD, and 0.1 mD, respectively. Samples with greater permeability displayed lower hydrocarbon peaks than those with lower permeability in the FTIR spectra, similar to that observed by Büyükutku *et al.* (2020) [8]. The aromatic C-H peaks and $CH=CH_2$ peaks of alkenes indicate the presence of unsaturated hydrocarbons. According to FTIR analysis, it was concluded that the shales of the Kusuri Formation contain organic matter and they are in the aromatic structure.
.
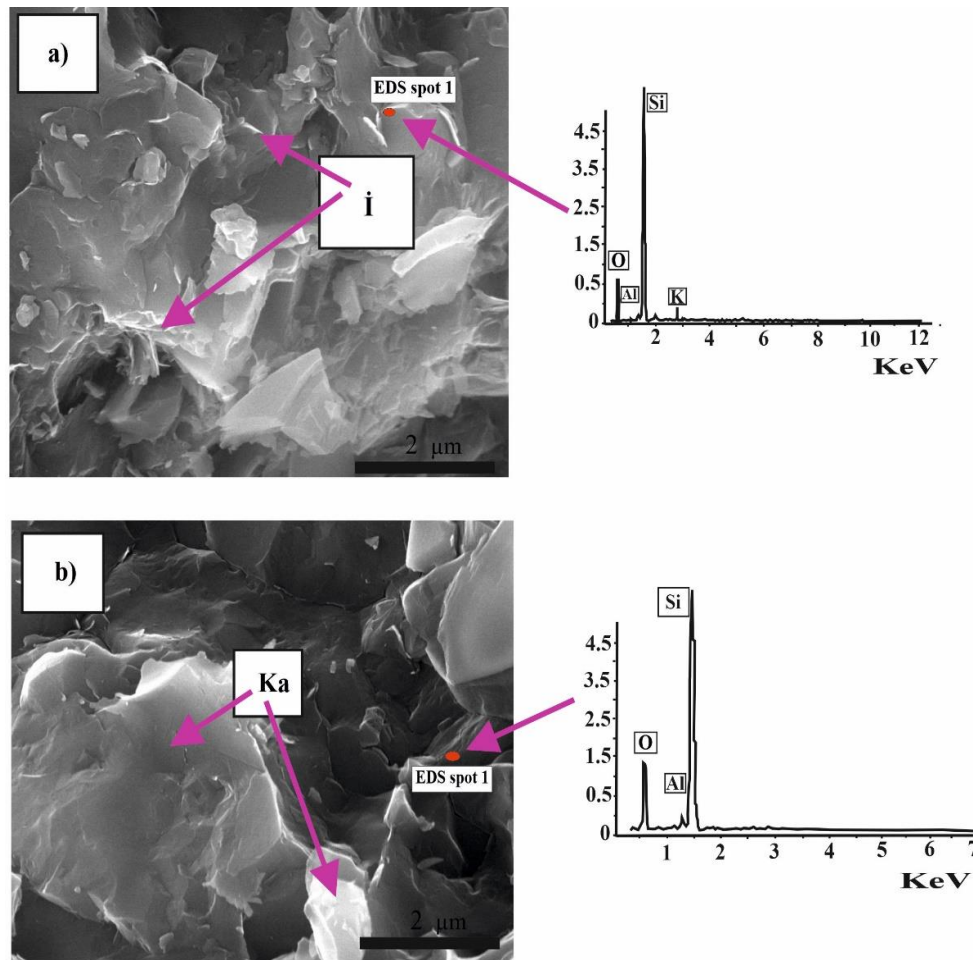
Fig. 4. SEM microphotographs of Kusuri formation. a) In the photograph, illite clay minerals (I) are observed in an acicular form. The K peak is dominant in the EDS graph. Core number: 2. Depth: 2115.0 m. b) Kaolinite clay minerals (Ka) are observed in the form of booklets. In the EDS graph, it is observed that Al, Si and O peaks are dominant. Core number: 2. Depth: 2115.0 m.
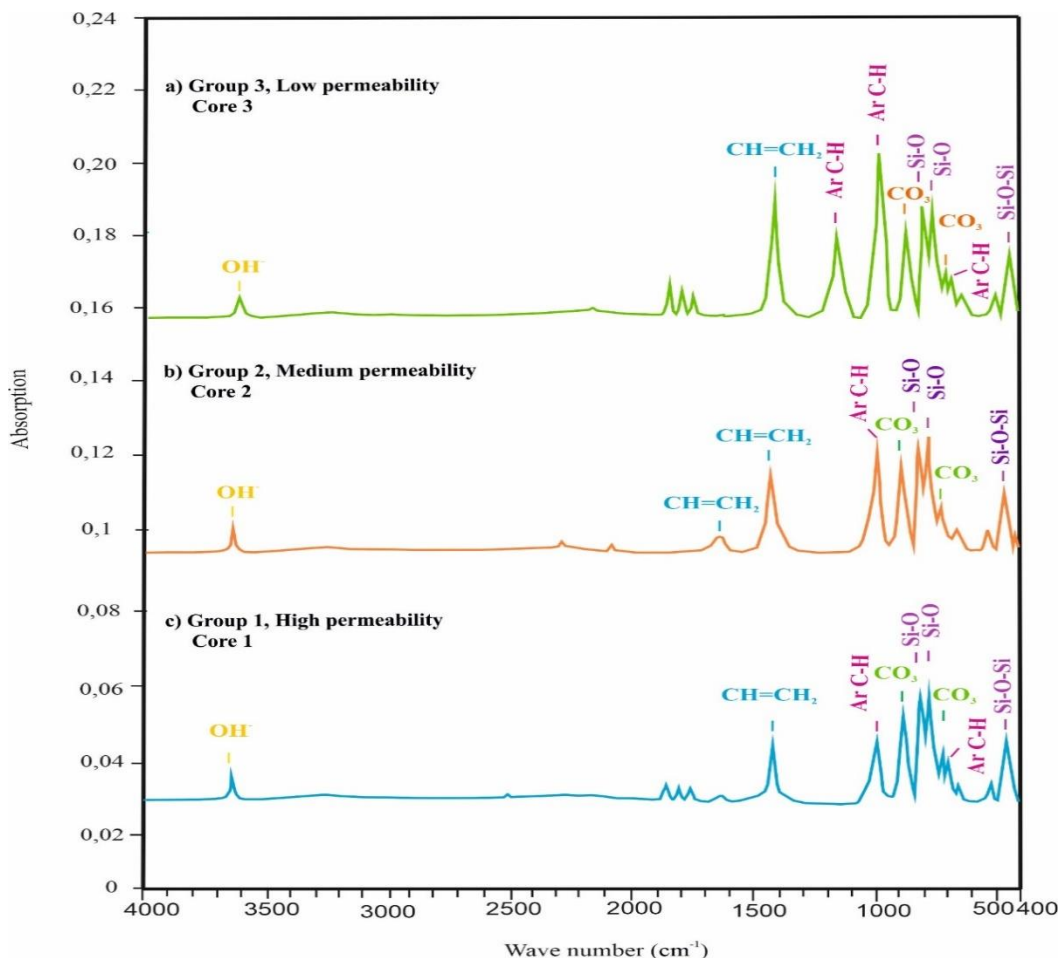
Fig. 5. FTIR spectra

CONCLUSIONS

In this study, Kusuri Formation sandstones with gas potential in the Zonguldak subbasin were investigated. A reservoir characterization was carried out by combining petrographic analysis and log-based petrophysical assessment (porosity and permeability values). According to the ATR FTIR analyses performed on the shale samples of the Kusuri Formation, the presence of organic matter and aromatic hydrocarbons was established.

The present study quantitatively analyses Kusuri sandstone sediments as regards their reservoir potential. Here, I present the first detailed reservoir investigation of Kusuri sandstones. This is the first-ever work from the studied field that presents a detailed petrographic and petrophysical investigation of different groups (Group 1, Group 2, and Group 3 sandstones) to imply the grain size, presence of organic matter, clay minerals, and reservoir quality. The porosity and permeability of the Kusuri sandstones are controlled by clay minerals and early calcite cement. It was observed that clay and early carbonate cement reduce the porosity and permeability. As fracture porosity was observed in the petrographic sections of the Kusuri

sandstones, the reservoir rock porosity and reservoir quality increased. In the Kusuri Formation sandstones, Group 3 sandstones do not display a reservoir character, whereas Group 1 and 2 sandstones show moderate-good reservoir characteristics according to porosity and permeability values. According to FTIR analysis, it was determined that the Kusuri Formation shales contain organic matter that displays aromatic structure and gas formation.

REFERENCES

1. A. S. Derman, *TPJD Bull.*, **14(1)**, 37 (2002).
2. W. H. J. Curry, W. H. Curry, *Am. Assoc. Petroleum Geologists Bull.*, **38**, 2119 (1954).
3. D. A. Busch, *Am. Assoc. Petroleum Geologists Bull.* **43**, 2829 (1959).
4. W. L. Fisher, J. H. McGowen, *Am. Assoc. Petroleum Geologists Bull.,* **53**, 30 (1969).
5. D. A. Goddard, J. B Echols, *Basin Research Institute Bulletin*, **3(1)**, 3 (1993).

6. C. Vandré, B. Cramer, J. Winsemann, *Org. Geochem.*, **38(4),** 523 (2007).

7. E. J. Acra, O. C. Ogbonna-Orji, U. P., Adiela, *Journal of Scientific and Engineering Research,* **4(4)**, 290 (2017).

8. A. Büyükutku, Diagenesis and reservoir properties of the Çağlayan Formation sandstones passed through two wells drilled around Ereğli Amasra, Ankara University Scientific Research Project, Ankara, 2020.

9. F. J. Pettijohn, P. E. Potter, A. Siever, Sand and sandstone, Springer Verlag, New York, 1973.

10. M. B. Adamu, *Nigerian Journal of Basic and Applied Science*, **18**, 6 (2010).

11. B. Udvardi, I. J. Kovacs, P. Kónya, M. Földvari, J. Füri, F. Budai, G. Falus, T. Fancsik, C. Szabó, Z. Szalai, J. Mihál, *Sedimentary Geology*, **313**, 1 (2014).

12. Schlumberger, Log interpretation charts, Schlumberger Educational Services, Houston, 1986, p. 1.

13. Schlumberger, Log interpretation charts, Schlumberger Well Services, Houston, 1996, p. 2.

14. A. Timur, *The Log Anal.,* **9**, 3 (1968).

15. Schlumberger, Log Interpretation Principles/ Applications, Schlumberger Educational Services, Houston, Texas, 1989.

16. A. I. Levorsen, in: Geologie of petroleum, second edn., W. H. Freeman (ed.), San Francisco, 1967.

17. H. W. van der Marel, H. Beutelspacher, Atlas of Infrared Spectroscopy of Clay Minerals and their Admixtures, first edn., Elsevier: Amsterdam, Holland, 1976, pp. 241 and 305.

Preparation of modified polyethersulfone membranes for hemodialysis

Ö. Ş. Kahraman[1], M. T. Phoo[1], İ. Küçük[1], A. Hasanoğlu[1,2]∗

[1]Yıldız Technical University, Chemical Engineering Department, Esenler, Istanbul, Turkiye
[2]Bursa Technical University, Food Engineering Department, Yıldırım, Bursa, Turkiye

Polyether sulfone (PES) is one of the common materials used as a membrane in hemodialysis. However, its use in pristine form is limited since its contact with blood can cause various interactions between the membrane and blood cells. Therefore, PES should be modified to reduce these reactions before its use in hemodialysis applications. In this study, tissue and blood-compatible PES based dialysis membranes were prepared by phase inversion method. To improve the biocompatibility and hemo-compatibility of the membrane, the PES polymer was blended with two polymers; polyvinylpyrrolidone (PVP) and polyethyleneglycol (PEG). PES polymer (15% (wt)) in N-methylpyrrolidone was used to prepare the pristine PES membranes while a polymer blend of 5% (wt) PVP or PEG additives and 10% (wt) of PES in the same solvent was used to prepare the modified PES membranes. Biocompatibility and hemo-compatibility of the prepared membranes were defined by water sorption, BSA protein and creatinine adsorption values. The sorption and BSA adsorption experiments indicated that the addition of PVP and PEG in the membrane matrix increased the hydrophilicity of the membrane and decreased the protein adsorption rate. In the light of these results, it was seen that the biocompatibility of the membranes can be increased using PVP and PEG additives in the PES membrane by reducing the amount of protein adsorption, and the modified membranes can prevent complications from contact with blood.

Keywords: Hemodialysis, biocompatible membranes, polyether sulfone, polyvinlypyrrolidone, polyethylene glycol

INTRODUCTION

Hemodialysis is a clinical process used for kidney patients, which aims to remove toxic biological substances from blood such as urea and creatinine. Acute kidney diseases can be mortal for the patients and the number of kidney patients is growing by 6-7% annually worldwide [1]. The core element of the hemodialysis process is the membrane which provides the separation of the toxic materials. The most important requirement for a hemodialysis membrane is the biocompatibility and hemo-compatibility of the membrane material, as well as the high rejection to toxic substances. The membrane should eliminate the toxic metabolites and excess water from blood by means of its preferential selectivity and should prevent clotting and platelet adhesion owing to its biocompatibility and hemo-compatibility. When polymeric membranes are in contact with blood, blood proteins tend to adsorb on the membrane surface and this phenomenon may have several adverse effects such as coagulation of blood cells and thrombosis. Thus in hemodialysis, the most crucial issue is the development of highly biocompatible membranes with high separation performance. In order to increase the biocompatibility of the membrane material several techniques such as surface modification, blending, grafting, nanoparticle adding have been applied [2-4].

Several polymeric materials have been applied for hemodialysis membranes including polysulfone [5], PAN and PAN/PVP [1, 6], chitosan [7], cellulose acetate [8] and polyethersulfone (PES) [1, 9-11]. Among the polymers used in medical applications, PES is one of the most applicable membranes thanks to its high performance properties such as high thermal and mechanic stability and easy handling for film preparation. Over the last four decades, PES membranes have been used commonly in microfiltration and ultrafiltration applications. Furthermore, it has been used in several medical applications such as artificial organs, hemodialysis, hemofiltration, plasma collection [12]. However, PES should be modified for its use in medical applications since it has poor hydrophilic properties which can cause protein adsorption and other problems such as aggregation and coagulation. Several methods have been reported in the literature to enhance the biocompatibility of PES membranes [12-14]. Fang *et al.* (2009) blended PES with acrylonitrile and acrylic acid followed by BSA grafting on the surface. They reported that the water contact angle and protein adsorption significantly decreased after the modification [12]. Zhu *et al.* (2007) blended PES with styrene-maleic anhydride to increase the hydrophilicity [13]. Irfan *et al.* (2014) used nanoparticles for surface modification of PES. First, they functionalized multi-wall carbon nanotubes, mixed the nanoparticles with polyvinyl-

pyrrolidone (PVP), and blended them with PES. They reported that the resulting membranes were more hydrophilic than the pristine PES [14]. In general, the modification techniques include bulk modification, surface modification and blending [12]. Blending the PES polymer with other polymers to improve its properties is a practical method in terms of short preparation procedures and easy film casting. Blending method allows to optimize the properties without complicated synthesis processes. Polyethylene glycol (PEG) and PVP are known as good hydrophilic agents in the polymeric blends and are usually used as additives to change the properties of polymers [15, 16]. In this study, PES polymer was modified by the blending method using PVP and PEG with different molecular weights to increase the biocompatibility. Biocompatibility of the membranes was evaluated by water sorption and BSA adsorption. Also creatinine adsorption tests were done for evaluation of the membranes for creatinine removal. This way it was aimed to develop high performance membranes with good biocompatibility and selectivity for hemodialysis.

MATERIALS AND METHOD

Materials

Polyether sulfone (PES, Ultrason E3010) was purchased from BASF, Germany. N-methyl-2-pyrrolidone (NMP) used as solvent was supplied by VWR International. Isopropanol used as solvent was purchased from Isolab GmbH. Polyvinylpyrrolidone (PVP, MW: 58000) was purchased from Acros Organics, New Jersey, US. BSA, creatinine and Folin Ciocalteu's phenol reagent used in protein adsorption determination were purchased from Sigma Aldrich. Polyethylene glycol (PEG, MW:1000 and 10000) used as additive, copper sulfate and sodium carbonate used as analytical reagents for Lowry method were purchased from Merck, Germany.

Membrane preparation

Before membrane preparation, the PES polymer was placed in an oven for 1 hour at 70°C for moisture removal. The dried PES was weighed in the desired amount and then a solution of PES in NMP was prepared by 15% w/w. The solution was stirred for 24 hours at 500 rpm at room temperature. Then the solution was cast onto glass plates with a blade at room temperature and the thickness of the wet films were about 254 µm. Afterwards, the membrane layers were immersed in a coagulation bath containing 77.5% of pure water, 20% of IPA and 2.5% of NMP. The membranes were kept in the bath

for 24 hours. Membranes removed from the bath process were taken between Teflon plates and kept there for 24 hours to avoid shrinking while drying. This was aimed to prevent contraction and superficial deformation by ensuring that the moisture removal is slow. Then the membranes were dried in an oven under vacuum at 50°C for 1 hour and at 70 °C for another 1 hour and the process was terminated. For PEG- and PVP-blended membranes the polymer solution was prepared by 10% of PES and 5% of PVP or PEG. All the remaining steps were the same as pristine PES membrane preparation.

Sorption experiments

Membranes with known weights were immersed into closed vessels containing water and kept at room temperature. Every 24 hours, the swollen membranes were wiped off and weighed. When no change was observed in weight, the sorption percentage was calculated using the equation below where m_{wet} and m_{dry} represent the weight of the wet and dry membrane, respectively:

$$Sorption\% = \frac{m_{wet} - m_{dry}}{m_{dry}} \times 100 \qquad (1)$$

Adsorption experiments

The membrane samples were cut into small pieces (2 cm × 2 cm) and inserted into closed vessels containing 1 mg/mL of BSA. The vessels were shaken for 8 hours using a shaker at the desired temperature. For the first 4 hours, a sample was taken from the vessels every hour and the concentration of BSA in the solution was measured using UV spectrophotometry (Analytic Jena Specord 200). Later, the samples were taken at the 6th and 8th hour. Then the adsorption amount of the membranes was calculated using the equation below where c represents BSA concentration. BSA concentrations were determined by the Lowry method:

$$Adsorption\% = \frac{c_0 - c_t}{c_0} \times 100 \qquad (2)$$

The creatinine adsorption tests were done likewise. In this case the concentration of creatinine was measured directly by UV spectrophotometry at 200 nm without using an analytical reagent.

Membrane characterization

SEM pictures of the membranes were taken using a Zeiss EVO LS 10 model and brand scanning electron microscopy equipment.

RESULTS AND DISCUSSION

Membrane morphologies

The cross-section SEM pictures of the membranes are given in Figure 1.
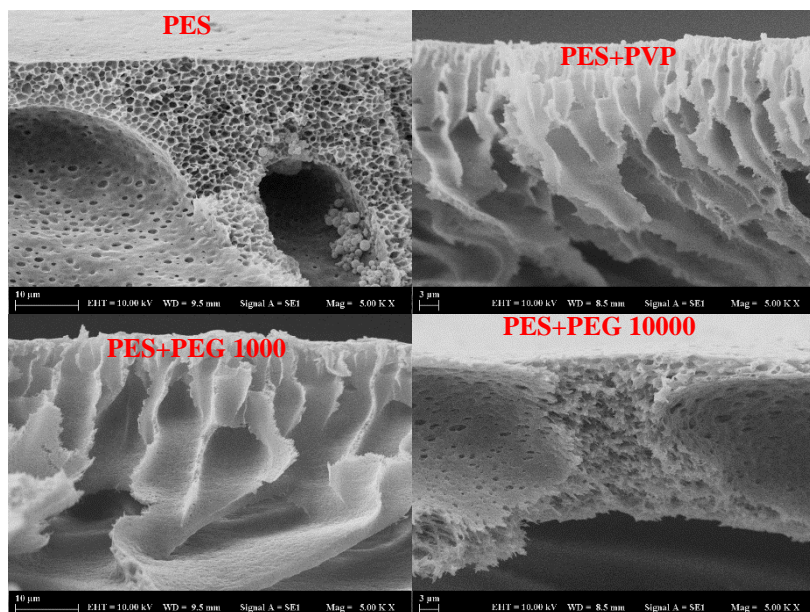
Figure 1. The cross section SEM pictures of the membranes

As can be seen in Figure 1, the structure of the membranes is modified by including the additives in the PES matrix. Furthermore, it can be seen that the porosity is increased for the modified membranes, especially for PVP and PEG 1000 additives. The pristine PES has sponge-like pores while the structures of the pores are converted to finger-like with the addition of PVP and PEG 1000. When the structures of all the membranes are compared, it can be seen that PVP has the highest porosity. On the other hand, the addition of PEG 10000 did not affect the porosity significantly.

the membranes were determined to obtain the hydrophilicity of the membrane materials.

Sorption results of the membranes in water are shown in Figure 2. As can be seen, the water sorption values of the blended membranes increased compared to the neat PES membrane. The addition of PEG and PVP additives increased the hydrophilicity of the membrane. When the membranes with the two additives of PEG and PVP are compared, it can be seen that PVP is more effective to increase the hydrophilicity. This can be a result of increased porosity of the PVP-blended membranes.
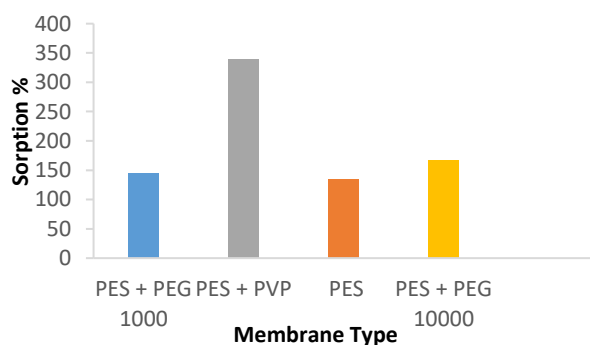

Figure 2. Sorption percentages of the membranes in water

Sorption results

In medical and biotechnological applications membrane hydrophilicity is favored since it prevents the biofouling. The hydrophilicity of the membrane leads to formation of a thin aqueous layer on the surface impeding the deposition of the proteins on the surface [1, 7]. Thus, the water sorption values of
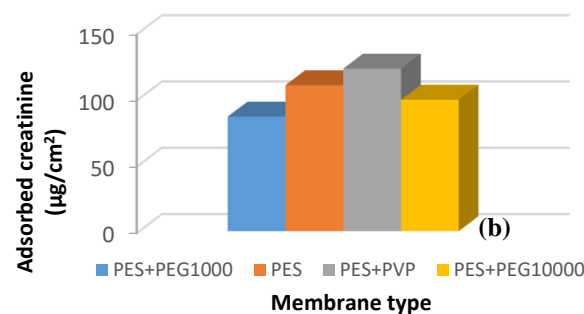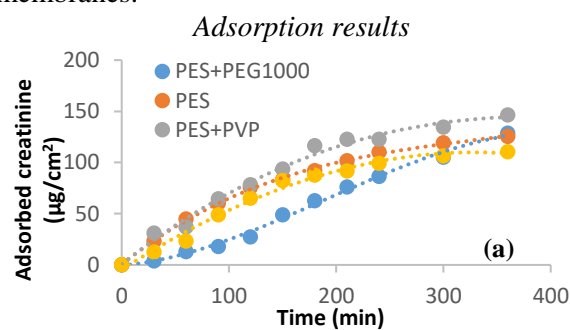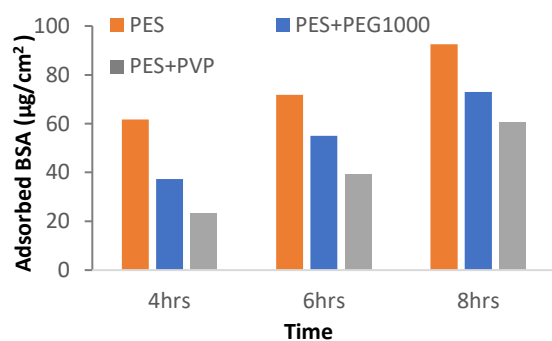

Figure 3. Adsorbed amounts of creatinine onto the membranes a) as a function of time b) in 4 hours

BSA and creatinine adsorption experiments were carried out to evaluate the biocompatibility of the membranes and the affinity of the membranes with creatinine. BSA adsorption onto the membrane is undesired since the adsorption of blood proteins onto the membrane material can cause complex problems. On the other hand, creatinine adsorption is desired since it should be removed from the blood using the membrane. Figure 3 shows the adsorbed creatinine amount onto the membranes.

Figure 4. Adsorbed BSA amounts onto the membranes

As can be seen from Figure 3, PVP blended membranes adsorbed more creatinine than the neat PES membrane and the PEG-blended membranes. With the addition of PEG into the membrane, a slight decrease in creatinine adsorption was observed. PVP showed better surface affinity towards creatinine. Thus, PVP-blended membranes are expected to permeate the creatinine molecules better than the neat membranes since the surface interactions with creatinine increased by the addition of PVP in the PES matrix. PVP-blended membranes have a potential to remove the creatinine not only by diffusion, but also by surface adsorption. Tijink *et al*. (2013) studied PES/PVP-based mixed matrix membranes containing activated carbon and reported that after 4 hours of simulated hemodialysis operation, both diffusion and adsorption equally contributed to the total creatinine removal [9]. The membranes were evaluated also in terms of their protein adsorption. Since PEG showed lower adsorption towards creatinine, only PEG1000-blended membrane was evaluated among the PEG blended membranes since it was easier to handle because of its lower viscosity. Figure 4 shows BSA adsorption of the membranes.

As can be seen in Figure 4, the BSA adsorption decreased for the blended membranes compared to the neat PES membrane. As the hydrophilicity of the membranes increased, the protein adsorption decreased. PVP-blended membranes showed the least amount of BSA adsorption because of its

highest hydrophilicity. The experiments indicate that the addition of hydrophilic polymer agents into the PES membranes improved the membrane against biofouling.

CONCLUSIONS

In this work the PES membranes were modified with PVP and PEG additives to improve the membrane properties for hemodialysis. The experiments showed that both additives increased the hydrophilicity of the membrane and consequently decreased the protein adsorption onto the membrane. The membranes modified with PVP had the highest hydrophilicity, indicating that it can have a better biocompatibility. Furthermore, the membranes were evaluated in terms of creatinine adsorption. PVP blended membranes showed higher surface affinity towards creatinine. The blended membranes have a potential to be used in hemodialysis applications. Future works will be done to determine the membrane interactions with urea and the membrane permeabilities for each component.

Nomenclature

BSA   bovine serum albumin;
c_0, c_t concentration initially and at the given time, respectively;
m   weight of the membrane samples;
PAN   polyacrylonitrile;
PEG   polyethyleneglycol;
PES   polyethersulfone;
PVA   polyvinyl alcohol;
PVP   polyvinylpyrrolidone.

REFERENCES

1. X. Yu, L. Shen, Y. Zhu, X. Li, Y. Yang, X. Wang, M. Zhu, B. S. Hsiao, *Journal of Membrane Science*, **523**, 173 (2017).
2. M. Irfan, A. Idris, *Material Science and Engineering C,* **56**, 574 (2015).
3. P. Thevenot, W. Hu, L. Tang, *Curr. Top Med. Chem.,* **8**, 270 (2008).
4. M. Tang, J. Xue, K. Yan, T. Xiang, S. Sun, C. Zhao, *Journal of Colloid and Interface Science*, **386**, 428 (2012).
5. M. Rafat, M. D. De, K. C. Khulbe, T. Nyugen, T. Matsuura, *Journal of Applied Polymer Science,* **101**, 4386 (2005).
6. W. C Lin, T. Y. Liu, M. C. Yang, *Biomaterials,* **25** 1947 (2003).
7. J. Liu, X. Chen, Z. Shao, P. Zhou, *Journal of Applied Polymer Science,* **90**, 1108 (2003).

8. O. Azhar, Z. Jahan, F. Sher, B. K. Niazi, S. J. Kakar, M. Shahid, *Materials Science and Engineering: C,* **126**, 112127 (2021).

9. M. S. L. Tijink, M. Wester, G. Glorieux, K. G. F. Gerritsen, J. Sun, P. C. Swart, Z. Borneman, M. Weeling, R. Vanholder, J. A. Joles, D. Stamatialis, *Biomaterials,* **34**, 7819 (2013).

10. A. Modi, S. K. Verma, J. Bellare, *Journal of Colloid and Interface Science,* **514**, 750 (2018).

11. S. Nie, M. Tang, C. Cheng, Z. Yin, L. Wang, S. Sun, C. Zhao, *Biomaterials Science,* **2**, 98 (2014).

12. B. Fang, Q. Baohong, W. Ling, Zhao, Y. Ma, P. Bai, Q. Wei, H. Li, C. Zhao, *Journal of Membrane Science,* **329,** 46 (2009).

13. L. P. Zhu, X. X. Zhang, L. Xu, C H. Du, B. K. Zhu, Y. Y. Xu, *Colloid Surf. B: Biointerf.,* **57**, 189 (2007).

14. M. Irfan, A. Idris, N. M. Yusof, N. F. M. Khairuddin, *Journal of Membrane Science,* **467**, 73 (2014).

15. J. Huang, J. Xue, K. Xiang, X. Zhang, C. Cheng, S. Sun, C. Zhao, *Colloids Surf. B: Biointerfaces,* **88**, 315 (2011).

16. Q. Yang, T. S. Chung, M. Weber, *Journal of Membrane Science,* **326**, 322 (2009).

CMC/PEG blended hydrogels for tissue engineering and regenerative medicine

D. Kavaz[1.2]*, N. Aşina[1.2]

[1] *Bioenginering Department, Faculty of Engineering, Cyprus International University, Nicosia 98258, Via Mersin 10, Turkey*

[2] *Biotechnology Research Centre, Cyprus International University, Nicosia 99258, Via Mersin 10, Turkey*

Hydrogels are ideal drug carrier systems for wound healing in tissue engineering and regenerative medicine applications. Their 3D structure supports the cell binding and tissue forming while treating the extracellular matrix for regulating the cellular functions. Poly (ethylene glycol) dmethacrylate (PEGDMA) based hydrogels hold a prominent place in tissue engineering but their applications are limited due to the low porosity and low biodegradability. Carboxymethyl cellulose (CMC) combined with PEGDMA hydrogels aims to decrease the porosity and cell viability for tissue regeneration with better swelling and biocompatibility features. The hydrogels were prepared with different concentrations of PEGDMA, CMC and Irgacure (2959). Surface morphology, pore size profile, chemical bonds and swelling behavior were investigated by scanning electron microscope (SEM) and Fourier-transform infrared spectroscopy (FTIR), respectively. The results show that the use of CMC improves the porosity along with the swelling behavior. Swelling results are in the range of 90-99.4%.

Keywords: Hydrogel; Tissue Engineering; Regenerative Medicine; PEGDMA; CMC.

INTRODUCTION

Wound healing is a highly complex system that includes many cell types, various cytokines, growth factors and their interactions. The wound healing mechanism plays a key role in tissue regeneration and healing in many enzymatic pathways, apart from cellular and biochemical components [1]. For this reason, natural and synthetic polymer-gel-like structures (hydrogels) which accelerate the process are mainly used in the wound treatment process.

Hydrogels are crosslinked homo- or copolymeric systems that can "swell" by absorbing a high amount of water. They are three-dimensional polymeric networks that don't dissolve in water but swell [2], that is, can take most of the water into their structures, and include both natural and synthetic polymers such as gelatin, agar and alginates [3]. Thus, water lover structure of the hydrogels made them the closest matter of structure to a real human tissue [4]. They swell to a stable volume in water but retain their shape. The amount of water absorbed by a hydrogel is quite large and can even reach 1000 times its own weight. For this reason, they have been used in a wide variety of fields in recent years.

Hydrogels can be classified depending on the method of preparation, ionic charge or physical structure [5, 6]. According to the preparation method, there are 4 types of hydrogels: homopolymer, copolymer, multipolymer and IPN (interpenetrating network) hydrogels. Hydrogels can be prepared by crosslinking with a radiant or a chemical reaction [7]. Radiation reactions take place with electron-emetic, irradiated, X-rays, or UV-rays. Chemical crosslinking occurs in the presence of at least one difunctional, small molecular weight crosslinking agent. This agent binds two long polymer chains through their functional groups.

Polymerization using UV radiation is the safest and cleanest polymerization method as it does not degrade the polymer properties [8, 9]. No chemical additives such as initiators, solvents, protective colloids or surfactants are required for this type of polymerization. As a result, the polymer retains its biocompatibility [10]. In addition, the use of radiation dose depends on the application area of the crosslinked polymer, and radiation dose and time are also important issues that affect the degree of crosslinking of the polymer.

Crosslinked polymer hydrogels exhibit a unique swelling behavior without dissolving in an aqueous environment or when entering a solvent, due to their high water absorption ability and the presence of critical crosslinks in their structure [11]. Their water absorption ability is due to the presence of hydrophilic functional groups such as –CONH, –OH, –$CONH_2$ and –SO_3H in the polymer structure forming the hydrogel. Water absorption by the hydrogel depends on the functional group, the state of the water, and the density of the crosslinking net-

* To whom all correspondence should be sent:
E-mail: dkavaz@ciu.edu.tr

work in the hydrogel [12]. Crosslinks in polymeric networks are achieved by hydrogen bonding, covalent bonds, van der Waals interactions, or physical entanglement. The degree of swelling is often used to describe hydrogels [13, 14]. The degree of swelling also depends on many factors such as mesh density, solvent structure, polymer-solvent interaction parameter.

Photopolymerized poly (ethylene glycol) dimethacrylate (PEGDMA) has been extensively studied for biomedical applications such as cell encapsulation, tissue engineering and drug delivery [9, 15]. PEGDMA is highly hydrophilic and the resulting hydrogel assets are tunable by changing the polymers molecular weight and water content. CMC on the other hand, is water-soluble anionic cellulose derived biopolymer with hydrophilic, pH-sensitive, non-toxic and easy gel-formable behavior [16, 17]. These characteristics show promising features in drug delivery systems and regenerative medicine [18].

Novel hydrogels were created by crosslinking carboxymethyl cellulose (CMC) sodium salt with PEGDMA in this study. The degree of crosslinking and the action of PEG as a network modifier were proven to adjust the mechanical and physico-chemical properties, as well as morphological aspects, in order to mirror the characteristics of real and genuine skin tissue.

EXPERIMENTAL

Materials

Poly (ethylene glycol) and dimethacrylate (PEGDMA) 1000 were purchased from Polysciences, phosphate buffered saline (PBS), carboxymethyl cellulose (CMC) and 2-hydroxy-4'-(2-hydroxyethoxy)-2-methylpropiophenone (Irgacure D-2959) were purchased from Sigma-Aldrich.

Preparation of Polymer Solution

0.2% (w/v) of Irgacure D-2959 was added into 5 mL of 1M PBS solution and heated at 100℃ with continuous stirring for 10 min. 20% (w/v) Poly (ethylene glycol) dimethacrylate was added into the Irgacure/PBS solution under constant stirring and left to dissolve. CMC solution was prepared in 1M PBS solution as well, 4% CMC was weighed and added into 30 mL of hot PBS under constant stirring. Remaining 70 mL were stored in a fridge for 30 min to cool down. After all CMC particles were evenly dispersed, 70 mL of cold PBS was added and continued stirring.

Samples were placed 5 cm away from the lamp and 3 mL of solutions were dropped into 60 mm

248

glass petri dishes. All samples were exposed to UV lamp for 5, 10 and 15 min (Table 1).

Freeze-Drying

Freeze-drying (lyophilization) technology is a drying method that can remove all water content without changing the material quality and shape properties of the products. It occurs by freezing the product first, then reducing the pressure in the environment and the water accumulated in the sample evaporates.

**Table 1.** Photo crosslinking duration and ratios of the hydrogels

	Crosslinking Time	PEGDMA:CMC:Irgacure (w/v)
P1	5 Min	2:1:1
P2	10 Min	2:1:1
P3	15 Min	2:1:1
C1	5 Min	1:2:1
C2	10 Min	1:2:1
C3	15 Min	1:2:1
I1	5 Min	1:1:2
I2	10 Min	1:1:2
I3	15 Min	1:1:2
S1	5 Min	1:1:1
S2	10 Min	1:1:1
S3	15 Min	1:1:1
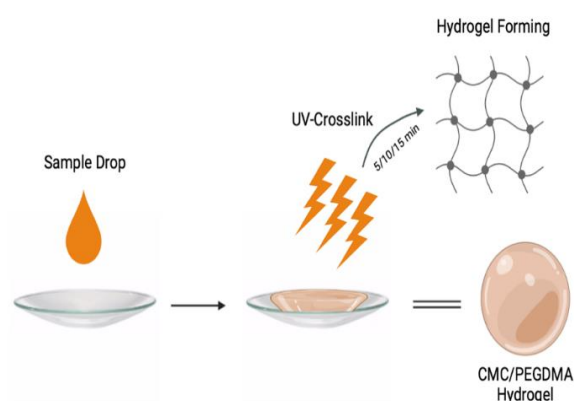
Figure 1. Schematic photopolymerization process of the hydrogels

Most of the physico-chemical properties of the product are preserved safely. Biobase brand freeze-dryer was used for the lyophilization process. Samples were first placed at -20 ℃ for pre-freezing

for 12 h and then placed at -80 °C for 24 h. After pre-freezing, the samples were freeze-dried at -72 °C with constant vacuum for 48 h.
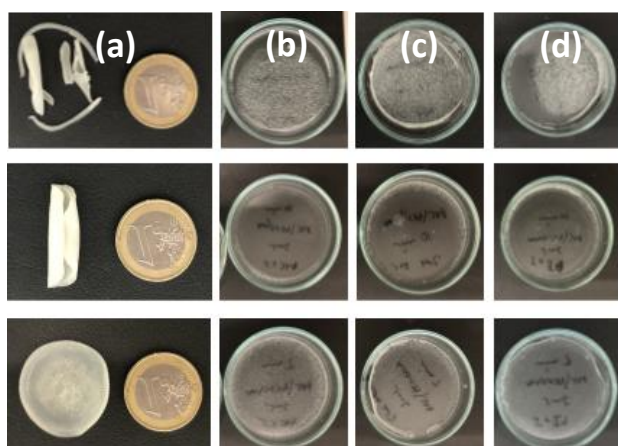
Figure 2. Photo-crosslinked (a) P, (b) C, (c) S and (d) I polymers.

CHARACTERIZATION

Fourier transmission infrared spectroscopy

Shimadzu IR Prestige 21 model FTIR spectroscope was used during the analysis. Organic or inorganic compounds are characterized by the tool called infrared (IR) spectroscopy. In response to the frequencies formed by the vibration of the bonds between the atoms that make up the matter, the IR spectrum shows the corresponding absorption peaks. PEGDMA, CMC and CMC/PEGDMA samples were analyzed by FTIR to conform the bonding between PEGDMA and carboxymethyl cellulose.

SEM and Porosity

Scanning electron microscope (SEM) is a system designed within the framework of electro-optical principles, which enables high-energy electrons to interact with the material to take the sample's surface morphology. The generated electron and photon signals interact with the sample by high-energy electrons. The computer-aided system collects the resulted images as a processing of the detector by the scattered electrons collected from different angles. Secondary electrons, material topography, and backscattered electrons provide information on atomic composition based on atomic number and contrast. Emitech brand SC7620 sputter coater was used for coating the samples. JEOL brand

JSM-6610 model scanning electron microscope was used for the analysis. Samples were coated with gold for 90 sec with 5mA current.

For polymer-based hydrogels, the porous structure holds a great importance especially for the cell hosting, cell culture and proliferation. The open structure on the other hand, affects the swelling behavior and mechanical properties of the hydrogel. Different types of materials are available, used for tissue engineering applications, which should provide particular properties to be able to fit for the application. Porosity is one of the main characteristics which affects the cell growth and proliferation. Specific pore size is preferred in the biomaterial production, particularly for cell culture or tissue engineering approaches due to the sufficient oxygen transportation through the ECM, as well as toxic compound removal and cellular growth.

Swelling

Swelling ratio is the water absorption ratio of a polymer as the ratio of wet weight of the sample and dry weight of the sample calculated while conducting the test. Swelling analysis was carried out in PBS solution. Pre-weighed samples (3n) were placed into 3 mL of PBS and kept for 24 h and 48 h at room temperature.

$$(Sk) = \frac{Wt - Wo}{Wo} x100$$

(Sk) is the swelling ratio, where (Wo) is the dried mass of the hydrogel and (Wt) is the wet mass of the hydrogel.

Statistical analysis

The swelling results are presented as mean ±standard error of the mean. SPSS Statistics, SPSS Software version 26 was used during Two-way ANOVA test followed by 3 factor ANOVA, Tukey's multiple comparison test, and factor interaction effect. Significance was considered if the p value was p≤0.05. All data were repeated three times.

One-way ANOVA was used while SEM pore size data was analyzed, then followed by Tukey HSD from SPSS and ImageJ. The data are presented as mean ±standard error of the mean. Significance was verified convenient if the p value was p≤0.05 and each sample was analyzed three times to be significant.
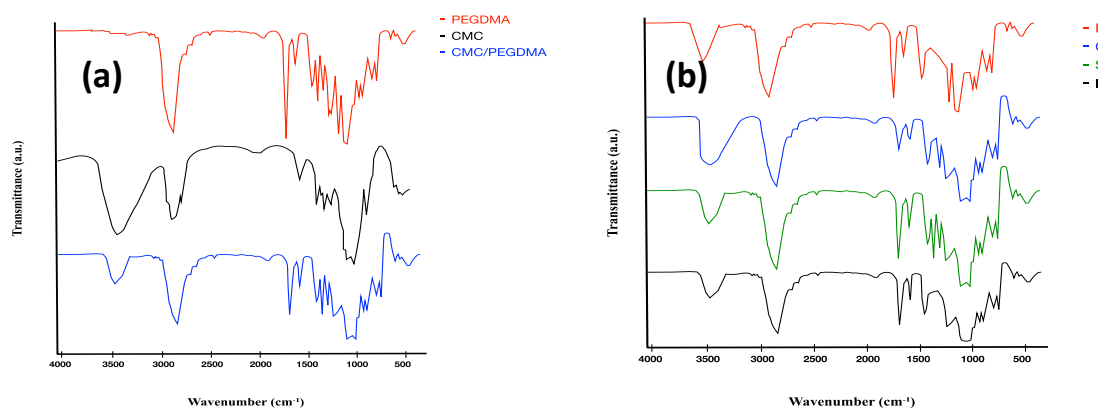
Figure 3. FTIR results of (a) PEGDMA, CMC and CMC/PEGDMA blend, (b) P, C, S and I.

RESULTS AND DISCUSSION

FTIR Results

Figure 3 presents the FTIR spectrum patterns of CMC, PEGDMA, CMC/PEGDMA and photopolymerized hydrogel, respectively. Based on Figure 3 (a), the observed peaks in the range of 3500-2750 cm^{-1} wave numbers represent polysaccharides; O-H and C-H bonding. The single peak in hydrogel formation at 1300 cm^{-1} shows the main chain of PEGDMA hydrogel as Fathi-Achachelouei *et al.* [19] found similar results in their hydrogel studies. For the CMC spectrum, C-H stretching was observed at 3000 cm^{-1}, hydrocarbon groups (-CH$_2$ scissoring) at 1450 cm^{-1} also peaks around 1400-1100 were observed corresponding to COO$^-$, OH coupling interactions of the carboxylic group and C-N stretching. C-H, C=C, C-O, amine I, amine II and amine III (stretching and forming) confirmed the binding between CMC/PEGDMA hydrogels. Both PEGDMA and CMC contain absorption peaks of C=C and C=O group chain as Klunklin *et al.* [20] mentioned.

On Figure 3 (b), all hydrogel variations and their bands are compared. Based on the polymerization technique, all showed identical characteristics with CMC/PEGDMA hydrogel. Only few differences were observed depending on the ratio difference. For instance, while P has a similar peak at 1720 cm^{-1} with PEGDMA itself, C showed a similar peak with CMC at 1720 cm^{-1}.

Surface Morphology and Porosity

SEM results helped to characterize and compare the surface morphology of all hydrogel variations. Figure 4 represents the variation of hydrogels along with the PEGDMA hydrogel without added CMC to compare the porosity with/without CMC. Best porosity was observed on C hydrogel, followed by P, S and I, respectively. Figure 4(b) confirms the additional increase in porous structure and the structural change after CMC addition. Figures 4(c) and 4(d) also show similar surface structure but lower porosity when compared with (a) and (b). Figure (e) clearly defines the surface difference when CMC is not added. As Barnett *et al.* [21] mentioned, PEGDMA polymer itself has low porous state without optimum environment (such as thickness and drying method) and plays a critical role on determining the morphology and pore size thereby the hydrogel behavior.

SEM images were used for the pore size distribution, performed on vertical and horizontal cross sections. Average pore diameter of samples imaged spontaneously. All samples were analyzed with average ± standard error. Each sample had 3-5 images during the pore size calculations. C group of hydrogels showed the highest porosity while I group of hydrogels showed the lowest porosity, when compared with P and S. P and S showed similar result with each other which also conforms the effect of carboxymethyl cellulose on porosity. Barnett *et al.* [21] found a pore size range between 5-40% in average. The pore size of the hydrogel must be big enough for the cells to migrate into the structure but small enough at the same time to establish a sufficient surface area. The average size of the fibroblast cells varies between 10-15 μm. In this study, the synthesized CMC/PEGDMA hydrogels showed an average pore size of 20-60 μm, which structure is suitable for cell growth and tissue engineering approaches.
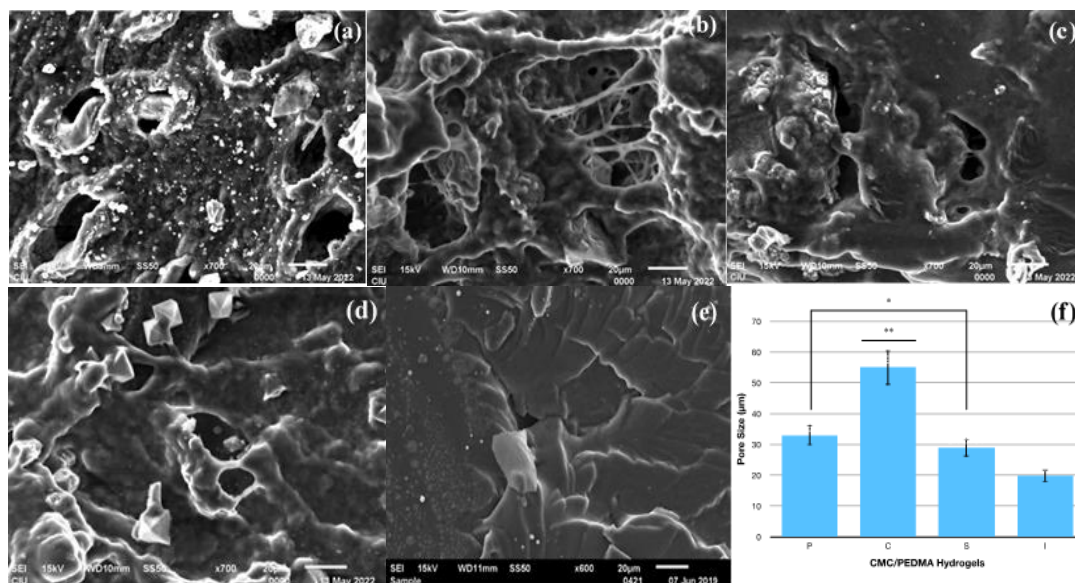
Figure 4. SEM results of (a) P, (b) C, (c) S, (d) I, (e) PEGDMA without CMC and (f) pore size distribution of /CMCPEGDMA hydrogels.
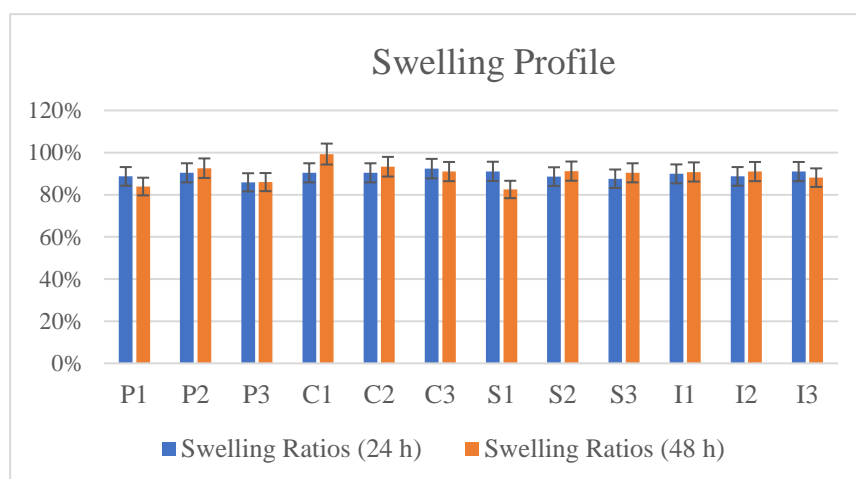
Figure 5. Swelling results of CMC/PEGDMA hydrogels with different ratios, (n=3).

Swelling Results

Swelling profile of the hydrogels is represented on Figure 5. The results were observed as a function of time in PBS over 48 h. Four ratios were compared with three different variations. Swelling profiles for all combination methods were compared with each other. P polymer blend achieved 90.4% over 24 h and 92.6% peak over 48 h while C polymer blend achieved up to 92.4% over 24 h and 99.3% peak over 48 h which recorded the highest swelling ratio out of the four polymer blends. Moreover, S polymer achieved 91.1% over 24 h and 91.2% peak over 48 h, and I polymer blend achieved 91.0% peak over 24 h and 48 h. No significant difference was observed in between the four polymer blends but in conclusion, C polymer blend achieved the highest swelling behavior. Zhang *et al.* [22] and Burke *et al.* [9] studied high-water content and resilience of

PEG-based hydrogels to compare the swelling equilibrium of PEG-based hydrogels and their mechanical properties. Zhang and co-workers [22] observed a similar result with 97.5% and 99.4% swelling profile with different PEG ratios whereas, Burke and co-workers [9] found around 40% swelling for their biodegradable PEGDMA hydrogels.

CONCLUSION

An exceptional design methodology for the fabrication of CMC/PEG hydrogels was examined. SEM, FTIR and swelling were employed in the characterization of the CMC/PEG hydrogels. The hydrogels performed exceptionally in terms of moisture absorption and retention and have therefore proven to be compatible in regard to biomedical implementations including wound dressings.

Significant swelling ratios observed over 99.3% ratio. P (1/2/3) and C (1/2/3) showed the best swelling and binding properties. Future work aims to focus on cytotoxicity and anti-cancer studies of the hydrogel samples.

REFERENCES

1. C. C. G. Geoffrey, S. Werner, Y. Barrandon, M. T. Longaker, *Nature*, **453,** 314 (2008).
2. E. M. Ahmed, *J. Adv. Res.*, **6** (2), 105 (2015).
3. Y. Chen, Y. F. Liu, H. M. Tan, J. X. Jiang, *Carbohydrate Polymers*, **75**(2), 287 (2008).
4. D. F. Li, Y. X. Ye, D. R. Li, X. Y. Li, C. D. Mu, *Carbohydrate Polymers*, **137**, 508 (2016).
5. J. M. Korde, B. Kandasubramanian, *Ind. Eng. Chem. Res.*, **58**, 9709 (2019).
6. M. F. Akhtar, M. Hanif, N. M. Ranjha, *Saudi Pharm. J.*, **24** (5), 554 (2016).
7. N. Annabi, J. W. Nichol, X. Zhang, C. Ji, S. Koshy, A. Khademhosseini, F. Dehghani, *Tissue Eng. - Part B Rev.*, **16**(4), 371 (2010).
8. C. M. Bunney, P. E. Zink, A. N. Holm, A. A. Billington, C. J. Kotz, *Physiol. Behav.*, **176** (6337), 139 (2017).
9. G. Burke, Z. Cao, D. M. Devine, I. Major, *Polymers (Basel).*, **11** (8), (2019).
10. E. Caló, V. V. Khutoryanskiy, *Eur. Polym. J.*, **65**, 252 (2015).
11. B. H. Cha, S. R Shin, J. Leijten, Y. C. Li, S. Singh, J. C. Liu, N. Annabi, R. Abdi, M. R. Dokmeci, N. E. Vrana, A. M. Ghaemmaghami, A. Khademhosseini, *Adv. Health. Mater.*, **6** (21), 1 (2017).
12. Y. C. Chiu, M. H. Cheng, H. Engel, S. W. Kao, J. C. Larson, S. Gupta, E. M. Brey, *Biomaterials*, **32**(26), 6045 (2011).
13. C. Echalier, L. Valot, J. Martinez, A. Mehdi, G. Subra, *Mater. Today Commun.*, **20** (5), 100536 (2019).
14. L. R. Feksa, E. A. Troian, C. D. Muller, F. Viegas, A. B. Machado, V. C. Rech, *Nanostructures Eng. Cells, Tissues Organs from Des. to Appl.*, **64**, 403 (2018).
15. Lh. Yahia, *J. Biomed. Sci.*, **04** (02), 1 (2015).
16. M. Jamadi, P. Shokrollahi, B. Houshmand, M. D. Joupari, F. Mashhadiabbas, A. Khademhosseini, N. Annabi *Macromol. Biosci.*, **17** (8), 1 (2017).
17. A. Montero, L. Valencia, R. Corrales, J. L. Jorcano, D. Velasco, *Smart Polymer Gels: Properties, Synthesis, and Applications*, Second edn., Elsevier Ltd., 2019.
18. X. Guan, M. Avci-Adali, E. Alarçin, H. Cheng, S. S. Kashaf, Y. Li, A. Chawla, H. L. Jang, A. Khademhosseini, *Biotechnol. J.*, **12** (5), 1 (2017).
19. M. Fathi-Achachelouei, D. Keskin, E. Bat, N. E. Vrana, A. Tezcaner, *J. Biomed. Mater. Res. - Part B Appl. Biomater.*, **108** (5), 2041 (2020).
20. W. Klunklin, K. Jantanasakulwong, Y. Phimolsiripol, N. Leksawasdi, P. Seesuriyachan, T. Chaiyaso, C. Insomphun, S. Phongthai, P. Jantrawut, S. R. Sommano, W. Punyodom, A. Reungsang, T. M. P. Ngo, P. Rachtanapun, *Polymers (Basel)*, **13** (1), 1 (2021).
21. H. H. Barnett, A. M. Heimbuck, I. Pursell, R. A. Hegab, B. J. Sawyer, J. J. Newman, M. E. Caldorera-Moore, *Journal of Biomaterials Science, Polymer Edition*, **30** (11), 895 (2019).
22. Y. Zhang, D. An, Y. Pardo, A. Chiu, W. Song, Q. Liu, F. Zhou, S. P. McDonough, M. Ma, *Acta Biomater.*, **53**, 100 (2017).

Spectroscopic investigation of new benzanthrone luminescent dyes

M. Olipova[1], A. Maleckis[2], A. Puckins[1], A. Kirilova[1], E. Romanovska[1], E. Kirilova[1*]

[1] Institute of Life Sciences and Technology, Daugavpils University, Daugavpils, Latvia
[2] Faculty of Materials Science and Applied Chemistry, Riga Technical University, Riga, Latvia

Luminescent dyes have received a considerable attention for their potential applications in biochemical and medical assays. Benzanthrone dyes are a special class of environmentally sensitive, photostable, bright luminophores. In the present research the photophysical properties of benzanthrone derivatives with amidine group and bromine atom in various positions were investigated and compared. The absorption and luminescence spectra in several organic solvents with various polarities were recorded and analyzed. Interesting results about substituent effects on the physical properties of the prepared dyes are obtained and discussed. The studied amidines are characterized by pronounced fluorescence solvatochromism. The results demonstrated that the studied amidine fluorophores have good properties of large Stokes shift, high emission, polarity sensitivity, that offer a great potential for biological imaging.

Keywords: Luminescent dyes; Benzanthrone derivatives; Synthesis; Fluorescence spectroscopy; Solvatochromism

INTRODUCTION

Nowadays luminescent substances have attracted significant attention owing to their opportunities in various functional applications. Organic luminescent materials with bright emission have drawn considerable attention for their wide applications. Despite the significant progress made recently, there is still great potential in the development of luminescent molecular materials, in particular organic highly fluorescent substances. Benzo[a]anthracene-7-one derivatives are polyaromatic hydrophobic substances with useful photophysical properties. Today, luminescent benzanthrone derivatives are used in various fields, such as synthetic and natural fiber dyes, photoconductors, luminophores, fluorescent labels and probes [1-4].

In recent years there has been a growing interest in the design of nitrogen-containing compounds (such as amidines) which can form luminescent complexes and associates in solids and solutions. Compounds with amidine group have played an important role in diverse areas such as catalyst design, material science, medicinal chemistry [5-8].

It is known that substituted aromatic amidines have an intense luminescence in solutions. Furthermore, the use of amidinate-ligated iridium complexes for fabrication of high-efficiency phosphorescent organic light-emitting devices has been reported [9].

Many amidines are employed as versatile tools in numerous applications such as fluorescent turn-on/turn-off sensors for the determination of diverse analytes - metal cations, amines, DNA, etc. [10-13].

For several years our research group has been working on benzanthrone dyes with D-π-A architecture, appearing to be particularly interesting because these dyes ultimately lead to prospective luminescent markers and sensors. In previous works, a series of benzanthrone-substituted amidines were synthesized from the corresponding primary arylamines by their condensation with substituted amides in the presence of phosphorus oxychloride [14-16]. The aim of the present research was to study and compare the photophysical properties of benzanthrone derivatives containing amidine constituents in various positions of the aromatic system.
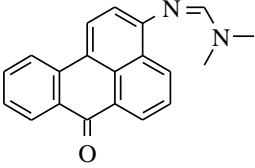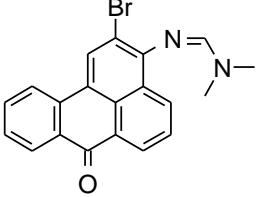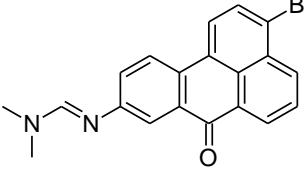
EXPERIMENTAL

Materials

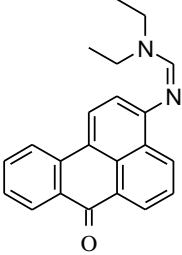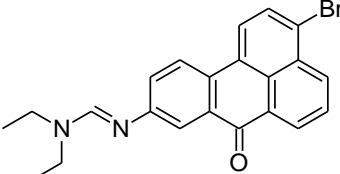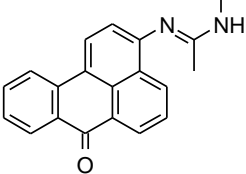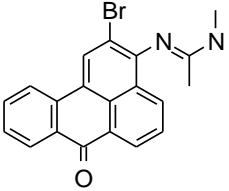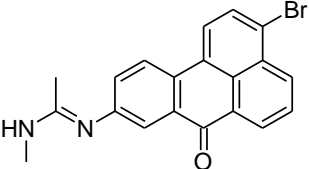The studied dyes were synthesized as described in the previous articles [14-16]. The chemical structures of the used compounds are presented in Table 1. The solvents as hexane, chloroform, benzene, ethyl acetate (EtOAc), acetone, ethanol (EtOH), N,N-dimethylformamide (DMF), and dimethylsulfoxide (DMSO) were of spectroscopic grade and were procured from Sigma Aldrich Chemical.

Spectroscopic measurements

Spectral properties of the investigated compounds were measured in various organic solvents with concentrations 10^{-5} M at ambient temperature in 10 mm quartz cuvettes. The absorption spectra were obtained using the UV-visible spectrophotometer Specord`s UV/VIS.

* To whom all correspondence should be sent:
E-mail: jelena.kirilova@du.lv

Table 1. Structure of studied amidines.
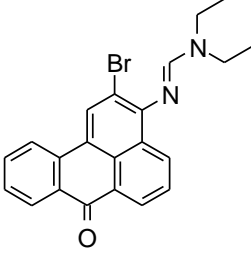
The fluorescence emission spectra were recorded on a FLSP920 (Edinburgh Instruments Ltd.) spectrofluorometer using Rhodamine 6G ($\Phi_0=0.88$) as a standard.

RESULTS AND DISCUSSION

In previous studies, benzanthrone derivatives with an amidine group and bromine atom in various position of benzanthrone core were synthesized from the corresponding amino benzanthrones – 3-aminobenzanthrone, 2-bromo-3-aminobenzanthrone and 3-bromo-9-aminobenzanthrone by their condensation with substituted amides in the presence of POCl₃. All these substances show pronounced light emission properties.

It was of interest to analyze how different positions of the same constituent affect the optical properties of benzanthrone derivatives, because one of the basic tasks of spectroscopy is to elucidate regularity between chemical structure of a particular substance and its optical characteristics.

In connection with our current interest on the design of novel luminescent compounds for bio-visualization and sensing purposes, we report a comparative study of several new luminescent analogous benzanthrone derivatives. In this work,

the spectral data were analyzed for the following compounds:

a) three compounds with an amidine fragment in the 3rd position of the benzanthrone aromatic system (A1-A3);

b) three substances with an amidine group in the 3rd and a bromine atom in the 2nd position of benzanthrone (B1-B3);

c) three compounds with an amidine group in the 9th position and a bromine atom in the 3rd position of the aromatic core (C1-C3).

These luminescent compounds contain a strong electron-donating amidine group and an electron-accepting carbonyl group linked by an aromatic spacer. In addition, the bromine atom affects the electronic density in compounds B1-B3 and C1-C3.

The electronic absorption spectra of the studied compounds (see Table 2) show a broad long-wave band around 420-490 nm, which has a charge transfer character, due to $\pi{-}{>}\pi^*$ electron transfer during the $S_0{-}{>}S_1$ transition [17]. The charge transfer in benzanthrone dyes occurs from the electron donor-acceptor interaction between electron-donating substituents and the electron-accepting carbonyl group of the chromophorous system.

Table 2. Absorption maxima (log e) of the studied amidines in various solvents (concentrations 10^{-5} M).

	A1	A2	A3	B1	B2	B3	C1	C2	C3
Hexane	437	443	432	429	434	427	439	444	433
	(4.28)	(4.35)	(3.96)	(4.11)	(4.03)	(4.30)	(4.35)	(4.45)	(4.21)
Benzene	456	461	447	447	448	443	460	461	448
	(4.27)	(4.31)	(3.91)	(4.02)	(4.05)	(4.28)	(4.38)	(4.46)	(4.33)
CHCl$_3$	464	460	448	447	449	446	465	472	455
	(4.18)	(4.25)	(4.11)	(4.06)	(4.07)	(4.35)	(4.37)	(4.48)	(4.17)
EtOAc	459	465	449	447	448	446	464	466	457
	(4.22)	(4.30)	(4.11)	(4.00)	(4.08)	(4.30)	(4.38)	(4.51)	(4.31)
Acetone	462	474	449	448	455	448	473	476	463
	(4.20)	(4.24)	(4.06)	(4.06)	(4.10)	(4.36)	(4.37)	(4.52)	(4.30)
Ethanol	471	476	448	447	448	446	473	477	455
	(4.12)	(4.12)	(4.07)	(3.96)	(4.02)	(4.34)	(4.33)	(4.05)	(4.24)
DMF	479	484	467	457	462	456	482	485	472
	(4.30)	(4.31)	(4.14)	(4.03)	(4.04)	(4.27)	(4.30)	(4.49)	(4.29)
DMSO	488	491	473	462	464	460	490	492	476
	(4.31)	(4.35)	(4.13)	(3.99)	(4.00)	(4.26)	(4.24)	(4.49)	(4.34)

Table 3. Fluorescence maxima (quantum yield) of the studied amidines in various solvents (concentrations 10^{-5} M).

	A1	A2	A3	B1	B2	B3	C1	C2	C3
Hexane	528	532	525	523	523	519	504; 527;	507;	527
	(0.64)	(0.70)	(0.64)	(0.23)	(0.25)	(0.29)	554	532; 554	(0.18)
Benzene	550	556	565	560	562	565	(0.28)	0.27)	570
	(0.67)	(0.74)	(0.60)	(0.20)	(0.22)	(0.31)	588	594	(0.42)
CHCl$_3$	590	615	608	594	601	608	(0.34)	(0.32)	610
	(0.56)	(0.72)	(0.58)	(0.25)	(0.27)	(0.30)	585	584	(0.32)
EtOAc	586	586	596	577	582	584	(0.38)	(0.37)	593
	(0.62)	(0.72)	(0.49)	(0.23)	(0.22)	(0.19)	612	608	(0.38)
Acetone	608	603	644	606	614	622	(0.29)	(0.30)	622
	(0.56)	(0.65)	(0.57)	(0.15)	(0.14)	(0.15)	657	657	(0.34)
Ethanol	646	655	665	624	633	666	(0.10)	(0.12)	668
	(0.27)	(0.30)	(0.18)	(0.01)	(0.01)	(0.05)	621	621	(0.14)
DMF	624	615	636	628	622	632	(0.23)	(0.20)	637
	(0.33)	(0.41)	(0.44)	(0.03)	(0.02)	(0.03)	651	634	(0.30)
DMSO	632	635	644	659	644	654	(0.12)	(0.11)	648
	(0.20)	(0.28)	(0.48)	(0.03)	(0.03)	(0.03)			(0.26)

Table 4. Stokes shifts (in cm^{-1}) of fluorescence maxima of the studied derivatives in various solvents.

	A1	A2	A3	B1	B2	B3	C1	C2	C3
Hexane	3944	3776	4100	4190	3922	4151	3804	3726	4120
Benzene	3747	3706	4672	4514	4527	4874	3688	3641	4777
CHCl$_3$	4602	5479	5874	5536	5633	5975	4498	4351	5585
EtOAc	4721	4440	5493	5040	5139	5299	4458	4336	5019
Acetone	5198	4514	6744	5819	5691	6244	4802	4561	5521
Ethanol	5751	5741	7283	6345	6523	7407	5921	5743	7008
DMF	4851	4401	5690	5958	5568	6107	4644	4516	5487
DMSO	4669	4619	5614	6470	6024	6448	5047	4552	5576

Compounds with only substituted amidine group at 3rd position absorb at 430-490 nm with high extinction coefficients, and emit at 530-650 nm showing both absorption and fluorescence solvatochromism. The introduction of bromine atom to 2nd position was found to cause a blue-shift (10-25 nm) of the absorption and emission bands and decrease in the fluorescent quantum yield. Compounds with bromine atom in 9th position show

a red shift of absorption maxima and increase of emission yield in comparison with the derivatives B1-B3.

All amidines are fluorescent in solutions in the region of 520-670 nm (see Table 3) and display large bathochromic shifts (110-150 nm) from hexane to ethanol solutions. However, compounds without a bromine atom in the molecule have a higher quantum yield of radiation (up to 74% in a benzene

solution). A large decrease in the quantum yield of radiation for compounds B1-B3 and C1-C3 indicates the energy loss in the excited state due to vibrational relaxation. The interaction of electrons of the bromine atom with the benzanthrone ring probably ensures nonradiative deactivation.

The Stokes shift was calculated because it is an important characteristic for fluorescent compounds. This parameter indicates the differences in the properties and structure of the emitting compound between the ground and the first excited state. Investigated derivatives display a significant Stokes shift (see Table 4), especially large in polar solvents (5700 - 7400 cm^{-1}). This is because the intramolecular charge-transfer effect leads to a large dipole moment in the excited state. Once excited, the solvent molecules surrounding the emitting compound molecule can reorder, resulting in a more stabilized, lower energy excited state. In a polar solvent the conformation of the dye molecule is probably twisted, and the twisted intramolecular charge transfer state (TICT) originates, which red shifts and decreases the efficiency of luminescence [18]. Therefore, the bathochromic shift and weakening of emission with growing solvent polarity might be caused by TICT formation.

Comparing amidines, a large Stokes shift is observed for compounds B1-B3 (up to 7400 cm^{-1} for amidine B3 in ethanol solution), which indicates great polarization of the molecule due to the influence of the bromine atom in 2nd position.

Therefore, the studied amidines exhibit remarkable Stokes shifts, which could minimize self-absorption and provide better fluorescence imaging in biology [19].

CONCLUSION

New data have been obtained on the relationship between the chemical structure of benzanthrone amidines and their photophysical properties, which may be of importance for the development of effective fluorescent derivatives based on the benzanthrone core and can be later used to create new promising fluorescent materials. Performed research demonstrates that the studied amidine fluorophores have good properties of significant Stokes shift, large extinction coefficient, high emission, polarity sensitivity.

The obtained results testify that the fluorescence of the synthesized amidino derivatives is sensitive to the change in polarity of surrounding medium, and fluorescence in the red region (above 600 nm in polar solvents) of the spectrum contributes to a high analytical sensitivity of the method using these fluorophores. These characteristics of the studied

benzanthrone dyes demonstrate their potential as biomedical probes for proteins, lipids, and cells. Such dyes can be also utilized as suitable sensing probes for checking solvent polarity.

REFERENCES

1. Y. Altaf, S. Ullah, F.A. Khan, A. Maalik, S.L. Rubab, M.A. Hashmi, *ACS Omega*, **6**, 32334 (2021).
2. O. Ryzhova, K. Vus, V. Trusova, E. Kirilova, G. Kirilov, G. Gorbenko, P. Kinnunen, *Methods Appl. Fluoresc.,* **4**, 034007 (2016).
3. E. Kirilova, I. Mickevica, L. Mezaraupe, A. Puckins, I. Rubeniņa, S. Osipovs, I. Kokina, A. Bulanovs, M. Kirjusina, I. Gavarane, *Luminescence,* **34**, 353 (2019).
4. I. Kalnina, L. Klimkane, E. Kirilova, M. M. Toma, G. Kizane, I. Meirovics, *J. Fluoresc.*, **17**, 619 (2007).
5. S. Caron, L. Wei, J. Douville, A. Ghosh, *J. Org. Chem.,* **75**, 945 (2010).
6. G. Li, M. Zhao, J. Xie, Y. Yao, L. Mou, X. Zhang, X. Guo, W. Sun, Z. Wang, J. Xu, J. Xue, T. Hu, M. Zhang, M. Li, L. Hong, *Chem. Sci.*, **11**, 3586 (2020).
7. O. K. Farat, I. V. Ananyev, A. L. Tatarets, S.A. Varenichenko, E. V. Zaliznaya, V. I. Markov, *J. Mol. Struct.*, **1224**, 12919 (2021).
8. H. Jiang, L. Xie, Z. Duan, K. Lin, Q. He, V. M. Lynch, J. L. Sessler, H. Wang, *Chem. Eur. J.*, **27**, 15006 (2021).
9. Y. Liu, K. Ye, Y. Fan, W. Song, Y. Wang, Z. Hou, *Chem. Commun.,* **25**, 3699 (2009).
10. A. R. Longstreet, R. R. Chandler, T. Banerjee, L. Z. Miller, K. Hanson, D. T. McQuade, *Photochem. Photobiol. Sci.*, **16**, 455 (2017).
11. I. Lee, S. Kim, S. N. Kim, Y. Jang, J. Jang, *ACS Appl. Mater. Interfaces*, **6**, 17151 (2014).
12. T. Tian, X. Chen, H. Li, Y.Wang, L. Guo, L. Jiang, *Analyst,* **138,** 991 (2013).
13. S. Maračić, P. Grbčić, S. Shammugam, M. R. Stojković, K. Pavelić, M. Sedić, K. S. Pavelić, S. Raić-Malić, *Molecules*, **26**, 7060 (2021).
14. S. Gonta, M. Utinans, G. Kirilov, S. Belyakov, I. Ivanova, M. Fleisher, V. Savenkov, E. Kirilova, *Spectrochim. Acta A*, **101**, 325 (2013).
15. E. M. Kirilova, A. I. Puckins, E. Romanovska, M. Fleisher, S. V. Belyakov, *Spectrochim. Acta A,* **202**, 41 (2018).
16. A. Kirilova, A. Puckins, S. Belyakov, E. Kirilova, *Molbank*, **2021**, M1287 (2021).

17. M. Nepras, O. Machalicky, H. Seps, R. Hrdina, P. Kapusta, V. Fidler, *Dyes Pigm.*, **35**, 31 (1997).
18. Z. R. Grabowski, K. Rotkiewicz, *Chem. Rev.,* **103**, 3899 (2003).
19. M. V. Sednev, V. N. Belov, S. W. Hell, *Methods Appl. Fluoresc*., **3**, 042004 (2015).

Computational examination of degradation reactions of Buprofezin

S. Kurumoglu, Y. Y. Gurkan[*]

Tekirdag Namık Kemal University. Department of Chemistry. Tekirdag. Turkey

Degradation reactions of molecules to be investigated will be examined by molecular modeling methods and theoretical approaches will be proposed for reaction pathways. For this purpose, possible reactions were calculated using Gaussian 09 package program. DFT method was used in the theoretical study. In this study, possible reaction paths in the reaction between pesticide substances and OH radical were determined. Fragmentation reaction requires energy; OH radicals are used to degrade pesticide substances. The lowest energy molecule has the most stable structure. According to *this*, when we list the pesticide substances and fragments from the most stable to the most unstable, they are F4, F2, F1, F3, Buprofezin. These results will guide experimental workers and determine the mechanism of fragmentation.

Keywords: Gaussian 09, DFT, Pesticide, Buprofezin.

INTRODUCTION

Due to the rapid increase in the world population and the decrease in natural resources as a result of population growth, various chemicals are used against pests such as insects, pathogenic organisms and weeds that will reduce yield, in order to increase agricultural production. Pesticides are among the most preferred chemicals. Many pesticides harm nature during production or use; they can mix with the atmosphere, soil and water resources.

Due to the increasing environmental pollution and climate crisis in the world, production activities have to be planned and implemented in a way that is sustainable and does not harm the environment. The methods used in agricultural production should be planned in a way that does not threaten human and environmental health [1]. If pesticides are used, it is of great importance to carry out qualitative and quantitative analyzes in soil and water resources. If the amount of pesticides does not exceed tolerance limits that will not adversely affect human health. and if it is above tolerance limits, it is of great importance to remove them from water and soil resources.

In addition to the residual chronic toxicity of pesticides, some of them have been found to have mutagenic, teratogenic and carcinogenic effects in humans in recent years. Pesticide deposits on plants, on the other hand, can sometimes pass to humans and animals through food, causing sudden poisoning, cancer, even dangers to genetic structure [2]. Behavior of pesticides in nature; degradation by soil microorganisms, chemical degradation (e.g. hydrolysis). adsorption and binding by organic and mineral soil. uptake by plant roots, evaporation, diluting effects of water flow processes [3].

Buprofezin is an insecticide with a thiadiazine structure. It acts by inhibiting chitin biosynthesis and subsequent cuticle deposition. It also has effects on the hormone levels of nymphs associated with moulting and on prostaglandin synthesis. It is not translocated in plants. It is for use on citrus fruit, tomato and lettuce [4]. The liver might be one of the major organs where Buprofezin accumulates and could represent the origin of an oxidative stress response following oral exposure to Buprofezin. During this process, Buprofezin at sublethal concentrations inhibited ATP production by promoting the conversion of energy metabolism from the aerobic TCA cycle and oxidative phosphorylation to anaerobic glycolysis [5].

The aim of this study is to computationally examine the degradation reactions of the pesticide molecule Buprofezin to remove it from water sources and convert it into harmless molecules.

METHODOLOGY

Degradation reactions of molecules to be investigated will be examined by molecular modeling methods and theoretical approaches will be proposed for reaction pathways. For this purpose, possible reactions were calculated using Gaussian 09 package program. DFT method was used in the theoretical study.

In this study, possible reaction pathways of the Buprofezin molecule were examined. For this purpose, Buprofezin was subjected to geometric optimization of its molecule and the most appropriate quantum mechanical method was determined. Possible products were theoretically predicted and calcual examinations were carried out.

Calculations of the most durable comforters of

* To whom all correspondence should be sent:

E-mail: yyalcin@nku.edu.tr

the Buprofezin molecule were carried out using DFT/B3LYP/6-31G(d) methods. All molecular orbital calculations were used in Gaussview5 molecular representation program and Gaussian 09W program [6].

The energy of the fragmentation reactions of all organic compounds is affected by water molecules in the aqueous environment. In addition, geometric stretching in the solution is induced by H_2O. However, the results obtained in many studies are that the geometry changes of the soluble substance for both open- and closed-shell structures have a trivial effect. Therefore. in this study in order to explain the solvent effect of H_2O on Buprofezin molecule to explain the solvent effect on Buprofezin + ·OH reaction energy; DFT/B3LYP/6-31G(d) method calculations were made and the COSMO (conductor-like screening solvation model) solvation model applied to the Gaussian package program was used [7].

RESULTS AND DISCUSSION

Fig. 1 shows the optimized geometric molecular structure of Buprofezin electronegative atoms attached to molecules; O. N. S are shown in color. The bond lengths, bond angles and Mulliken charges of molecules in Table 1 give preliminary information about the fragmentation sites of molecules.

When the Mulliken loads of the molecules in Table 1 are examined, the atoms with the highest electronegativity N_3. N_{20}. N_{21}. O_2 are written in bold in the table.

Electrochemical calculations in gaseous and aqueous phase were analyzed for each molecule. The ΔE energy. ΔH enthalpy and ΔG Gibbs free energy values in Table 7 are given separately for each molecule. When the Gibbs free energy values of ΔG were examined, it was seen that the ΔG value of each fragmentation was negative. Thus, we list the pesticide molecules from the most stable to the most unstable.
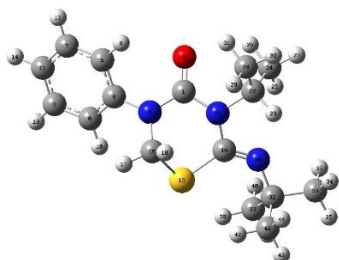
Figure 1. Optimized geometric structure of Buprofezin *via* DFT method. (grey. C; white . H; blue. N; red. O; yellow. S).

When the Mulliken loads of the Buprofezin molecule in Table 1 are analysed. the electronegative

atoms are N_3. O_2. N_{20}. N_{21}, respectively. As it can be seen in Figure 1. O_2 and N_{20} form a double bond with C_1 and C_{19} atoms. Since these bonds are stable, the bonds are not expected to break. N_{21}. O_2 atoms are the second and third electronegative atoms.

Buprofezin's most durable geometric structure is optimized with DFT/B3LYP/6-31G(d) methods. As a result of DFT calculations, Buprofezin's total energy in the gaseous phase is -791189 kcal mol^{-1}, enthalpy -791189 kcal mol^{-1}, Gibbs free energy -791234 kcal mol^{-1}. In addition, the total energy in the aqueous phase, enthalpy and Gibbs free energy are -791196 kcal mol^{-1}, -791195 kcal mol^{-1}, -791241 kcal mol^{-1}, respectively. Optimized with DFT/B3LYP/6-31G(d) methods, Buprofezin's geometric structure is shown in Figure 1 and geometric parameters are shown in Table 2.

Bond lengths of N_3-C_4 and N_{21}-C_{22} in Table 2 are 1.43 Å; 1.50 Å, respectively, and the bond angle of C_{19}-N_{20}-C_{32} is 128.98^0, while the bond angle of O_2-C_1-N_3 is the second widest bond angle with 122.62^0. Based on this information, it is expected that the methyl groups of C_4 and C_{22} atoms will break. So it is understood that this is the first stage of degradation mechanism. N_3 is the most electronegative atom. Looking at the area surrounded by this atom in Table 2, N_3-C_4 with a bond length of 1.43 Å although the N_3 atom is the most electronegative atom. Since there are bonds longer than this bond length, it is predicted that if there is a bond break here, it will happen after the other bonds. Even the fact that the bond angles N_3-C_4-C_5 and S_{15}-C_{19}-N_{21} in Table 2 are the widest ones, 120.79; 115.02, respectively, this will not change the situation. Buprofezin's fragments geometric structure and geometric parameters are shown in Tables 3-6.
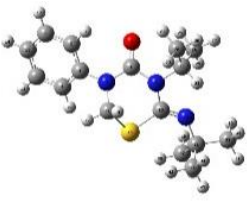
The ΔE, ΔH and ΔG values in Table 7 are given separately for each molecule. Looking at the data in Table 7, fragment 4 (F4) of Buprofezin has the lowest energy. In other words, it has the most stable structure. This fragment is formed by bond breaking from the ring to which the electronegative N atom is attached.

In this study, possible reaction paths in the reaction between Buprofezin and OH radical were determined. The degradation reaction requires energy. OH radicals are used to degrade pesticide substances in water. As seen in the fragments obtained, Buprofezin was reduced to F4 and became harmless to the environment. Our aim was to break down the pesticides that are mixed with water down to the smallest harmless substances and remove their toxic effect from water. As can be seen from the results, this fragmentation took place theoretically.
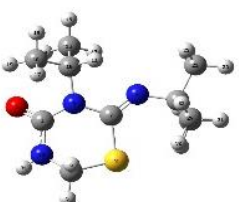
Table 1. Energy values of Buprofezin in gaseous and aqueous phases. and their Mulliken loads at gaseous phase.

Buprofezin ($C_{16}H_{23}N_3OS$)	Gaseous Phase (kcal × mol^{-1})	Aqueous Phase (kcal × mol^{-1})	Mulliken Loads	
	ΔE= -791189	-791196	**O_2**	**-0.508933**
	ΔH= -791189	-791195	**N_3**	**-0.525537**
	ΔG= -791234	-791241	C_6	-0.020480
			C_7	-0.010742
			C_9	-0.007077
			N_{20}	**-0.445599**
			N_{21}	**-0.521956**
			C_{28}	-0.002347
			C_{33}	-0.005052
			C_{37}	-0.000872
			C_{41}	-0.001032
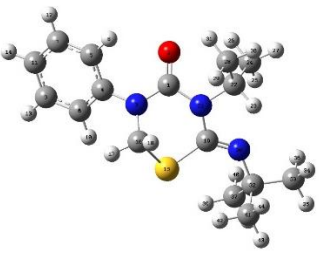
Table 2. Bond lengths and bond angles of atoms of Buprofezin molecule.

Buprofezin ($C_{16}H_{23}N_3OS$)	Bond Length	(Å)	Bond Angle	(°)
	C_1-O_2	1.22	O_2-C_1-N_3	**122.62**
	N_3-C_4	**1.43**	N_3-C_4-C_5	120.79
	N_3-C_{16}	1.44	N_3-C_{16}-S_{15}	110.96
	S_{15}-C_{19}	1.82	S_{15}-C_{19}-N_{21}	115.02
	C_{16}-S_{15}	1.83	C_{16}-S_{15}-C_{19}	95.23
	C_{19}-N_{20}	1.26	C_{19}-N_{20}-C_{32}	**128.98**
	N_{20}-C_{32}	1.47	N_{20}-C_32-C_{33}	105.16
	N_{21}-C_{22}	**1.50**	N_{21}-C_{22}-C_{28}	111.12

Table 3. Bond lengths and bond angles of atoms of F1 molecule.

F1	Bond Length	(Å)	Bond Angle	(°)
	C_1-N_{33}	1.37	C_1-N_{33}-C_4	122.39
	O_2-C_1	1.22	O_2-C_1-N_9	123.16
	S_3-C_7	1.82	S_3-C_7-N_8	125.41
	C_4-S_3	1.84	C_4-S_3-C_7	96.17
	C_7-N_8	1.26	C_7-N_8-C_{20}	129.27
	N_8-C_{20}	1.47	N_8-C_{20}-C_{25}	112.17
	N_9-C_{10}	1.50	N_9-C_{10}-C_{16}	111.16
	C_{10}-C_{12}	1.53	C_{10}-C_{12}-H_{15}	109.43
	C_{12}-H_{15}	1.10	C_1-N_{33}-H_{34}	114.43
	N_{33}-H_{34}	1.01		

Table 4. Bond lengths and bond angles of atoms of F2 molecule.

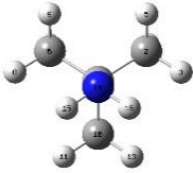| F2	Bond Length	(Å)	Bond Angle	(°)
	C_1-C_{11}	1.40	C_1-C_{11}-H_{12}	120.0
	C_2-C_5	1.40	C_2-C_5-H_9	119.99
	C_3-C_7	1.40	C_3-C_7-C_5	119.99
	H_4-C_1	1.09	H_4-C_1-C_{11}	119.99
	C_5-H_9	1.09	C_2-C_5-H_9	119.99

For the fragments in Table 7, the energy values in the gaseous and aqueous phase were examined. The lowest energy level, in other words the degradation path, starting from the most stable fragment for Buprofezin in Figure 1, was determined both in the light of the above mentioned predictions and by the analysis of the energy values of each fragment in Table 7.
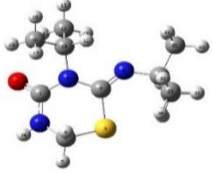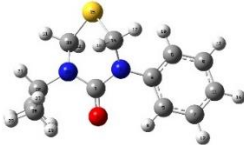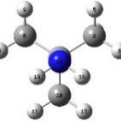
**Table 5.** Bond lengths and bond angles of atoms of F3 molecule.

F3	Bond Length	(Å)	Bond Angle	(°)
		1.22	O_2-C_1-N_3	123.77
N_3-C_1		1.40	C_4-N_3-C_1	122.66
C_4-N_3		1.43	C_5-C_4-N_3	118.80
C_5-C_4		1.40	C_6-C_9-C_{11}	120.34
C_6-C_9		1.39	S_{15}-C_{16}-N_3	113.26
S_{15}-C_{16}		1.85	N_{19}-C_{30}-H_{31}	108.41
N_{19}-C_{30}		1.46	C_{20}-N_{19}-C_1	119.98
C_{20}-N_{19}		1.49	C_{22}-C_{20}-C_{26}	112.47
C_{22}-C_{20}		1.54		
C_{26}-H_{28}		1.09		
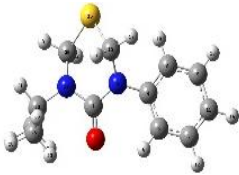
Table 6. Bond lengths and bond angles of atoms of F4 molecule.

F4	Bond Length	(Å)	Bond Angle	(°)
	C_2-C_1	1.54	C_2-C_1-N_{14}	107.26
	H_3-C_2	1.10	H_3-C_2-C_1	110.92
	H_4-C_2	1.09	H_4-C_2-C_1	111.08
	H_5-C_2	1.09	H_5-C_2-C_1	110.36
	C_6-C_1	1.54	C_6-C_1-N_{14}	107.26
	H_7-C_6	1.09	H_7-C_6-C_1	111.08
	H_8-C_6	1.10	H_8-C_6-H_9	107.96
	H_9-C_6	1.09	H_9-C_6-C_1	110.35
	C_{10}-C_1	1.54	C_{10}-C_1-N_{14}	112.46
	H_{11}-C_{10}	1.10	H_{11}-C_{10}-C_1	110.79
	H_{12}-C_{10}	1.10	H_{12}-C_{10}-H_{13}	107.67
	H_{13}-C_{10}	1.10	H_{15}-N_{14}-H_{16}	105.58
	N_{14}-C_1	1.48		
	H_{15}-N_{14}	1.02		
	H_{16}-N_{14}	1.02		

Table 7. Energy values at gaseous and aqueous phase of fragments of Buprofezin molecule at ground state.

Fragments	Gaseous Phase (kcal × mol^{-1})	Aqueous Phase (kcal × mol^{-1})
F1	ΔE = -646259.269 ΔH = -646258.677 ΔG = -646297.31	-646265.554 -646264.962 -646303.707
F2	ΔE = -145672.145 ΔH = -145671.552 ΔG = -145692.13	-145673.825 -145673.232 -145693.807
F3	ΔE = -658603.816 ΔH = -658603.224 ΔG = -658640.648	-658610.321 -658609.729 -658647.481
F4	ΔE = -134065.437 ΔH = -134064.845 ΔG = -134087.851	-134068.225 -134067.632 -134090.657

4.
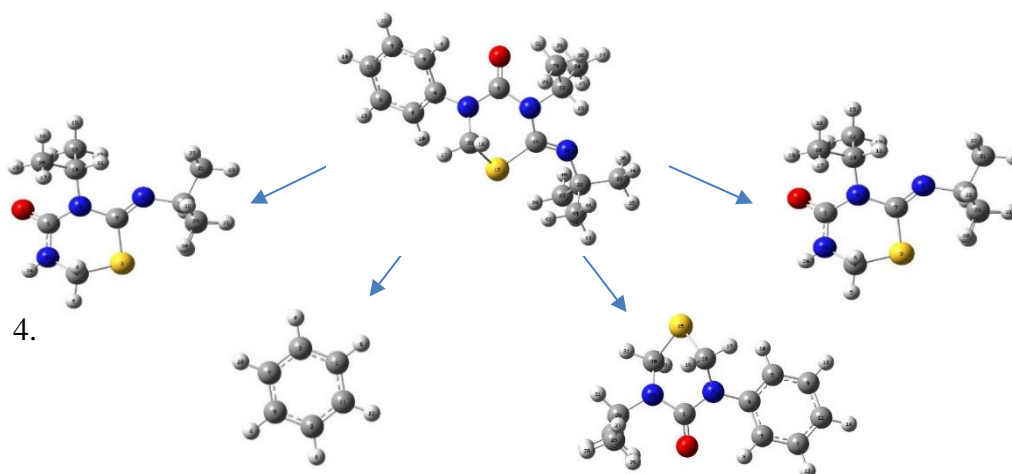
Figure 2. Optimized geometric structures of four fragments of the Buprofezin molecule. (grey, C; white, H; blue,N; red, O; yellow, S)

CONCLUSIONS

In this study, the possible reaction paths between the pesticide Buprofezin molecule and the OH radical were determined. For this purpose, geometry optimization of the molecules was made, then the most appropriate quantum mechanical method was determined and the possible products were theoretically predicted. The fragmentation reaction requires energy, OH radicals are used to degrade pesticide molecules. The lowest energy molecule has the most stable structure. Accordingly, we list the pesticide molecules from the most stable to the most unstable: F4, F2, F1, F3, Buprofezin. Our goal was to break down pesticide molecules molecules down to the smallest harmless substances. As can be seen from the results, this fragmentation took place theoretically. These results will guide experimental studies and determine the fragmentation mechanism.

REFERENCES

1. B. Sık, İ. Ö. Küçükçetin, T. Erkaymaz, G. Yıldız, *Akademik Gıda,* **10**(2) 89 (2012).
2. J. Dich, Sh. H. Zahm, A. Hanberg, H.-O. Adami, *Pesticides and Cancer Causes and Control*, **8** (1997).
3. M. G. Hayo van der Werf, *Agriculture, Ecosystems and Environment,* **60**, 81 (1996).
4. F. Hernandez-Jerez, P. Adriaanse, A. Aldrich et al., *The EFSA Journal,* **620**, 1 (2007).
5. X. Ji, T. Ku, N. Zhu, X. Ning, W. Wei, G. Li, N. Sang, *Journal of Hazardous Materials,* **320**, 176 (2016).
6. M. W. Hanna, Quantum mechanics in chemistry, Masachusetts: Benjamin/Cummings Publ., 1981.
7. J. P. Lowe, Quantum chemistry (2nd edn.). USA: Academic Press, 1993.

Degradation reactions of Covid-19 active ingredients by molecular modeling method

B. Pandir, Y. Y. Gurkan[*]

Tekirdag Namik Kemal University, Department of Chemistry, Tekirdag, Turkey

The coronavirus (Covid) is a large family of viruses known to cause a variety of illnesses, from the common cold to acute respiratory infections. The severity of the infection can be seen as pneumonia, acute respiratory syndrome and even death. This group of viruses was largely ignored until the SARS epidemic. However, since the SARS and MERS outbreaks, these viruses have been studied in more detail to advance vaccine research. On December 31, 2019, mysterious cases of pneumonia were detected in the city of Wuhan in China's Hubei Province. On January 7, 2020, the cause was identified as a novel coronavirus (2019-nCovid), and the disease was later named Covid-19 by WHO. In this study, possible reaction pathways of Afzelin, Delta Viniferin and Hesperidin molecules between OH radical were determined. Optimized geometries were plotted with Gauss View 5. Then, the lowest energy states were found by geometric optimization with the Gaussian 09 program.

INTRODUCTION

Coronavirus is a family of viruses with a positive-sense RNA that possess an outer viral coat. When looked at with the help of an electron microscope, there appears to be a unique corona around it. This family of viruses mainly cause respiratory diseases in humans, in the forms of common cold or pneumonia, as well as respiratory infections. These viruses can infect animals as well [1-2].

Up to the year 2003, coronavirus (CoV) had attracted limited interest from researchers. However, after the SARS (severe acute respiratory syndrome) outbreak caused by the SARS-CoV, the coronavirus was looked at with renewed interest [3, 4]. This also happened to be the first epidemic of the 21st century originating in the Guangdong province of China. Almost 10 years later, there was a MERS (Middle East respiratory syndrome) outbreak in 2012, which was caused by the MERS-CoV [5, 6]. Both SARS and MERS have a zoonotic origin and originated from bats. A unique feature of these viruses is the ability to mutate rapidly and adapt to a new host.

Coronaviruses are known to use Keni *et al.* COVID-19: a summary the angiotensin-converting enzyme-2 (ACE-2) receptor or the dipeptidyl peptidase IV (DPP-4) protein to gain entry into cells for replication [7-10].

In this study, geometric optimizations of reactions will be made on the basis of the DFT/B3LYP/6-31G(d) (Becke(B) 3 Lee-Yang-Parr (LYP)) method of quantum mechanical density functional theory (DFT). Fragmentation reaction mechanisms will be elucidated by using the calculated energy values for each molecule. All calculations of the active ingredients of Covid-19 will be performed both in the gas phase and in the water phase by modeling the solvent effect.

Active ingredients of Covid-19 are Afzelin, Delta Viniferin, and Hesperidin. Molecular weights and molecular formulas of Covid-19 active ingredients are given in Table 1.

Table 1. Molecular weights and molecular formulas of Covid-19 active ingredients

	Afzelin	Delta Viniferin	Hesperidin
Molecular weight	432.4 g/mol	454.5 g/mol	610.6 g/mol
Molecular formula	$C_{21}H_{20}O_{10}$	$C_{28}H_{22}O_6$	$C_{28}H_{34}O_{15}$

METHODOLOGY

The reaction model used in the computational part of this study is the reaction between the afzelin, delta viniferin, hesperidin molecules and the photo-generated •OH radicals [11]. Therefore, all the calculations were based on hydroxyl radical chemistry. Hydroxyl radicals can react with organic compounds by (i) hydrogen abstraction from single bonds, (ii) addition to double bonds, and (iii) one-electron oxidation, which is mostly loss of water from hydroxyl radical adducts. The reaction system under consideration consists of •OH radicals, in other words, open-shell species. It is well known that open-shell molecules pose severe problems in quantum mechanical calculations. Hartree–Fock (HF) methods suffer from spin contamination, because they are wave function-based. In contrast to

* To whom all correspondence should be sent:
E-mail: yyalcin@nku.edu.tr

the HF methods, density functional theory (DFT) methods use the exact electron density instead of the wave function to calculate molecular properties and energies. Electron correlation, whose absence is the main drawback to HF methods, is accounted for in DFT methods. They suffer from spin contamination less than HF methods and this feature makes them suitable for calculations involving open-shell systems. Therefore, geometry optimizations of the reactants were performed with the DFT method. The DFT calculations were carried out as implemented in GAUSSIAN 09 code [12], using the exchange-correlation functional B3LYP, which combines HF and Becke exchange terms with the Lee–Yang–Parr correlation functional, in combination with the 6-31G* basis set. Vibrational frequencies were calculated for the determination of the structures as stationary points and true minima on the potential energy surfaces. All the possible stationary geometries located as minima were generated by free rotation around single bonds [13].

RESULTS AND DISCUSSION

Theoretical prediction of the degradation mechanism

In the search for a plausible mechanism for the photocatalytic degradation reaction of Afzelin, Delta Viniferin and Hesperidin molecules DFT reactivity descriptors were employed to have information about the most susceptible sites for hydroxyl radical attack. Fig. 1 shows the optimized structure of Afzelin, Delta Viniferin and Hesperidin molecules and the numbering system that is used throughout the calculations. Three main competing reaction pathways shown in Fig. 2 were determined by selecting the specific sites of Afzelin molecule, on the basis of their softness values being close to that of the •OH radical.
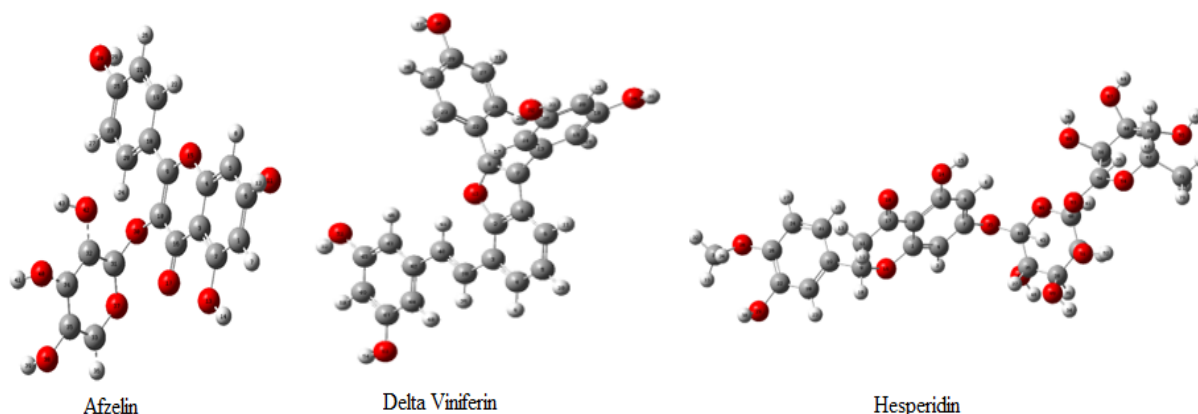

Fig. 1. Optimized geometric structure of Afzelin, Delta Viniferin and Hesperidin molecules *via* DFT method. (grey, C; white, H; red, O).
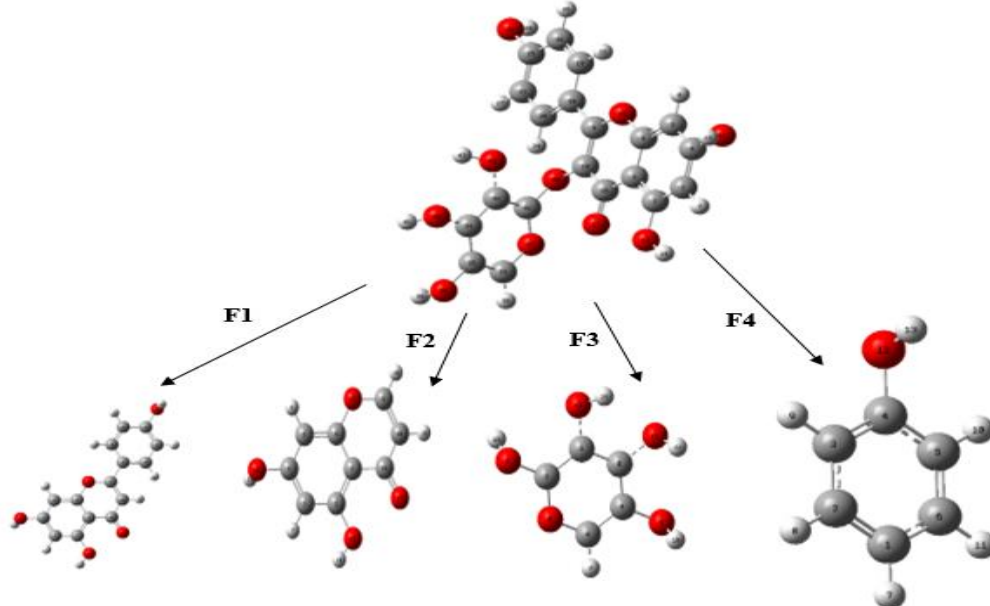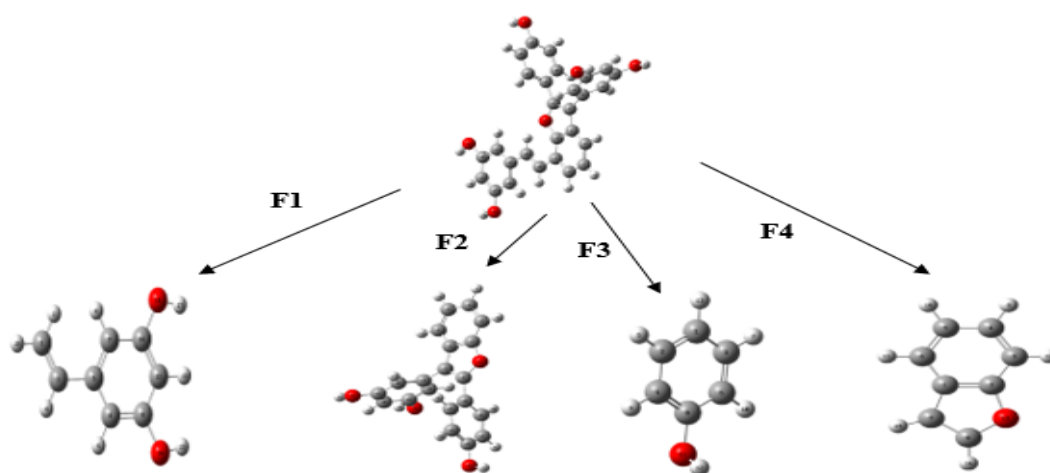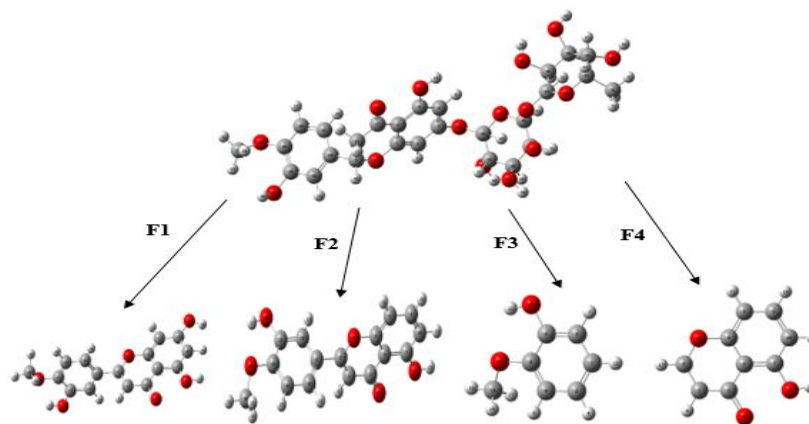

Fig. 2. Possible pathways for the photocatalytic degradation of Afzelin (grey, C; white, H; red, O)

Table 2. Constant energy, enthalpy and Gibbs free energy values according to the DFT method.

Molecules	Phase	Energy (kcal mol^{-1})	Enthalpy (kcal mol^{-1})	Gibbs free energy (kcal mol^{-1})
Afzelin	Gas	-954891.659	-954891.069	-954945.487
	COSMO	-954912.963	-954912.373	-954966.590
F1	Gas	-598315.296	-598314.704	-598353.105
	COSMO	-598330.741	-598330.149	-598368.530
F2	Gas	-406179.408	-406178.815	-406207.980
	COSMO	-406191.317	-406190.724	-406219.706
F3	Gas	-357324.236	-357323.643	-357353.844
	COSMO	-357331.972	-357331.379	-357361.547
F4	Gas	-192819.296	-192818.703	-192840.874
	COSMO	-192871.883	-192871.290	-192893.531

Fig. 3. Possible pathways for the photocatalytic degradation of Delta Viniferin (grey, C; white, H; red, O)

Fig. 4. Possible pathways for the photocatalytic degradation of Hesperidin (grey, C; white, H; red, O)

Table 3. Constant energy, enthalpy and Gibbs free energy values according to the DFT method.

Molecules	Phase	Energy (kcal mol^{-1})	Enthalpy (kcal mol^{-1})	Gibbs free energy (kcal mol^{-1})
Delta Viniferin	Gas	-960021.093	-960020.503	-960078.234
	COSMO	-960039.297	-960038.701	-960096.714
F1	Gas	-288609.624	-288609.031	-288636.960
	COSMO	-288616.978	-288616.385	-288644.319
F2	Gas	-672144.010	-672143.420	-672186.310
	COSMO	-672155.443	-672154.847	-672197.650
F3	Gas	-192867.756	-192867.164	-192889.392
	COSMO	-192871.884	-192871.291	-192893.531
F4	Gas	-240680.946	-240680.353	-240703.587
	COSMO	-240683.436	-240682.844	-240706.083

Table 4. Constant energy, enthalpy and Gibbs free energy values according to the DFT method.

Molecules	Phase	Energy (kcal mol^{-1})	Enthalpy (kcal mol^{-1})	Gibbs free energy (kcal mol^{-1})
Hesperidin	Gas	-1365293.170	-1365292.580	-1365365.410
	COSMO	-1365322.340	-1365321.740	-1365393.890
F1	Gas	-670157.649	-670157.053	-670199.215
	COSMO	-670173.036	-670172.446	-670214.558
F2	Gas	-622961.753	-622961.161	-623001.670
	COSMO	-622974.269	-622973.676	-623014.129
F3	Gas	-264710.265	-264709.673	-264735.726
	COSMO	-264714.291	-264713.698	-264739.829
F4	Gas	-358983.378	-358982.786	-359010.305
	COSMO	-358992.386	-358991.793	-359019.215

CONCLUSIONS

In the study, degradation mechanisms were estimated for three molecules and their reasons were explained by examining their energy values and electronegative atoms in the molecule, bond lengths and angles. In this study, possible reaction pathways were determined in the reaction between Covid agents and OH radical. The decomposition reaction requires energy. OH radicals are used to degrade Covid active ingredients. The lowest energy molecule has the most stable structure. Accordingly, we listed the Covid active ingredients from the most stable to the most unstable: Hesperidin - 1365293.170 kcal/mol, Delta Viniferin -960021.090

kcal/mol, Afzelin -954891.660 kcal/mol. Our aim was to break down the Covid active ingredients down to the smallest harmless substances. As can be seen from the results, this fragmentation occurred theoretically. These results will guide experimental workers and determine the fragmentation mechanism.

REFERENCES

1. K. McIntosh, J. H. Dees, W. B. Becker, A. Z. Kapikian, R. M. Chanock, *Proc.. Natl. Acad. Sc.* USA, **57**, 933 (1967).
2. F. Esper, C. Weibel, D. Ferguson, M. L. Landry, J. S. Kahn, *J. Infect. Dis.,* **191**, 492 (2005).
3. K. Stöhr, *Lancet*, **361**, 1730 (2003).
4. J. S. M. Peiris, S. T. Lai, L. L. M. Poon, Y. Guan, L. Y. C. Yam, W. Lim, *Lancet*, **361**, 1319 (2003).
5. A. Zumla, D.S. Hui, S. Perlman, *Lancet*, **386**, 995 (2015).
6. A. M. Zaki, S. van Boheemen, T. M. Bestebroer, A. Osterhaus, R. Fouchier, *N. Engl. J. Med.,* **367**, 1814 (2012).
7. S. Perlman, J. Netland, *Nat. Rev. Microbiol.,* **7**, 439 (2009).
8. W. Li, M. J. Moore, N. Vasilieva, J. Sui, S. K. Wong, M. A. Berne, *Nature*, **426**, 450 (2003).
9. X-Y. Ge, J.-L. Li, X.-L. Yang, A. A. Chmura, G. Zhu, J. H. Epstein, *Nature*, **503**, 535 (2013).
10. M. Wang, Z. Hu, *Virol. Sin.,* **28**, 315 (2013).
11. N. San, M. Kilic, Z. Cinar, *J. Adv. Oxid. Technol.*, **10**(1), 51 (2007).
12. Gaussian 09, Revision B.04, in: Gaussian, Inc., 2009.
13. J. P. Stewart, *J. Comput. Chem.*, **10**, 221 (1989).

Antioxidant and antidiabetic activities of hexane extract of *Genista januensis* var. *lydia*

C. Cakir[1], H. H. Orak[2], M. Argon[3], H. Caliskan[3], T. Sabudak[3*], M. Ozturk[1], N. Guler[4]

[1] *Department of Chemistry, Faculty of Science, Mugla Sıtkı Kocman University, Mugla, Turkey*
[2] *Department of Food Technology, Vocational School of Technical Sciences, Namik Kemal University, Tekirdag, Turkey*
[3] *Department of Chemistry, Faculty of Science and Arts, Namik Kemal University, Tekirdag, Turkey*
[4] *Department of Biology, Faculty of Science, Trakya University, Edirne, Turkey*

The genus *Genista* L. (*Fabaceae*) has been of interest for human beings since ancient times with its cosmopolitan distribution. Since α-amylase and α-glucosidase are the chief enzymes of diabetes mellitus, this study aims to study the α-amylase and α-glucosidase inhibitory potential and antioxidant activity of *Genista januensis* var. *lydia* grown in the Trakya region. To the best of our knowledge, there has been no study on *G. januensis* var. *lydia* up to date. The α-amylase/α-glucosidase inhibitory activity and antioxidant activity of the hexane extract of *G. januensis* var. *lydia* were studied by spectroscopic *in vitro* experiments to search the potential relationships of both activities.

Keywords: *Genista januensis*, antioxidant activity, α-amylase, α-glucosidase

INTRODUCTION

Genista genus (*Fabaceae*), which includes 140 species in total, has been used by mankind since ancient times owing to its cosmopolitan distribution. Some of the *Genista* genera have been used in folk medicine to treat respiratory diseases, rheumatic disorders, diabetes, and ulcers mainly in the Mediterranean. Moreover, the genus is also well known for its yellow pigment (color) [1] by the local people.

Nowadays medicinal plants and their isolated bioactive compounds have gained attention in the management of diabetes mellitus which has become a widespread disease all over the world. Antioxidants have important inhibition roles on tissue damage in various human diseases such as cancer, inflammation and atherosclerosis. The causal correlation between oxidative stress and type 2 diabetes has been explained through molecular mechanisms [2]. Therefore, overproduction of reactive oxygen species can create an imbalance in the amount of antioxidants in the body, ultimately leading to an oxidative stress associated with hyper glycemia. For that reason, providing antioxidants and α-amylase / α-glucosidase inhibitors due to nutriments is a potential and feasible method for managing type 2 diabetes.

Although some *Genista* species have been used for many purposes, including for their antidiabetic properties [3], to the best of our knowledge, no study was found on *G. januensis* var. *lydia*. Hence, the aim of this work was to investigate the antioxidant and antidiabetic properties of *Genista januensis* Viv. var. *lydia* (Boiss.) (*Fabaceae*) growing in the Trakya region.

EXPERIMENTAL

General experimental procedures

Spectrophotometric measurements were performed on a Hitachi spectrophotometer, model 121-002 for antioxidant assay. All chemicals were reagent grade and obtained from commercial suppliers. α-Amylase and α-glucosidase inhibitory activities of the hexane extract were measured by using a 96-well microplate reader, SpectraMax 340PC384 (Molecular Devices, Silicon Valley, California, USA). Softmax PRO v5.2 software (Molecular Devices, Silicon Valley) was used for calculations and measurements of the bioactivity data. α-Amylase (EC. 3.2.1.1, from porcine pancreas), sodium chloride (NaCl), starch, Lugol solution, acarbose, 4-N-nitrophenyl-α-D-glucopyranoside (PNPG), α-glucosidase (EC. 3.2.1.20, from *Saccharomyces cerevisiae*) were purchased from Sigma Chemical Co. (Sigma_Aldrich GmbH, Sternheim, Germany). Hydrogen chloride (HCl), methanol, hexane, sodium carbonate (Na_2CO_3) were purchased from E. Merck (Darmstadt, Germany). Analytical grade chemicals and solvents were preferred in this study.

Plant material and extractions

The plant was collected from Trakya region. The specimens (EDTU 16813) were identified by Dr. Necmettin Guler at Trakya University, Faculty of Science, Department of Biology. After being dried at room conditions and sliced into small pieces, the

plant was successively macerated using hexane, chloroform, ethyl acetate and methanol, respectively. The solvents were evaporated using a rotary evaporator, and the crude extracts were obtained.

Total phenolic / flavonoid content and antioxidant assay

The total phenolic content (TPC) was determined with Folin & Ciocalteu's phenol reagent and total flavonoid content (TFC) was determined by the $AlCl_3$-$NaNO_2$ method [4]. The ferric reducing power (FRAP), $ABTS^{•+}$ scavenging activity and DPPH radical scavenging activity of the *G. januensis* hexane extract were determined for assessing the antioxidant properties [4].

α-Amylase / α-glucosidase inhibitory assay

The α-amylase / α-glucosidase inhibitory activities of the hexane extract of *G. januensis* were determined spectrophotometrically [5, 6].

RESULTS AND DISSCUSSION

Total phenolic/flavonoid content

TPC of the hexane extract of *G. januensis* was found as 45.74±1.71 µg CAT mg extract^{-1}, while TFC was determined by the $AlCl_3$-$NaNO_2$ method (Table 1). Hanganu *et al.* [7] determined the content of total phenolics in a 70% ethanol extract of *G. tinctoria* and *G. sagittalis* species as 33.52±0.21 and 15.71±0.35 mg GAE/g, respectively.

Antioxidant assay

The evaluation of the antioxidant activity of *G. januensis* in hexane extract was carried out by using ABTS, FRAP and DPPH assays. According to analyses, DPPH radical scavenging activity increased depending on the concentration and EC_{50} values were determined as 0.112±0.04 mg mL^{-1} (Table 1, Fig.1).

Table 1. Total phenolic/flavonoid content and antioxidant assay.

Hexane extract of *G. januensis*	
TPC (µg CAT mg extract^{-1})*	45.74±1.71
TFC (µg CAT mg extract^{-1})*	Nd**
$ABTS^{•+}$(mmol Trolox mg extract^{-1})	0.357±0.19
FRAP (µmol Fe^{+2} g^{-1}extract^{-1})	520.54±3.84
EC_{50} values of DPPH capacity (µg mL^{-1})	112±0.04

*CAT: Catechin equivalent. **Nd: not determined. Data are expressed as the mean ± standard deviation (n ≥ 3).

Boubekri *et al.* [8] demonstrated remarkable results for the DPPH activity of the EtOAc and n-BuOH residues from the polar extract of *G. quadriflora* with a concentration dependence and the high antioxidant effect was attributed to the presence of phenolic compounds.
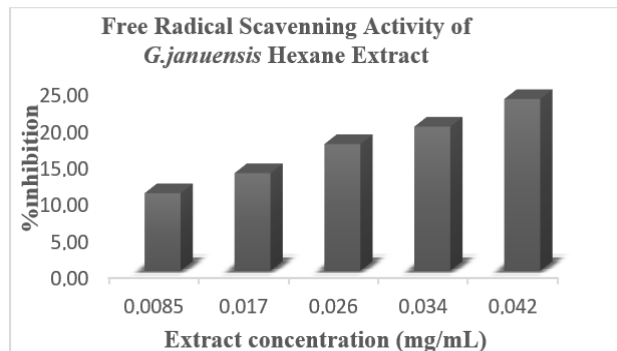
Fig. 1. DPPH radical scavenging activity of hexane extract of *G. januensis*.

α-Amylase / α-glucosidase inhibitory assay

The α-glucosidase and α-amylase enzyme inhibition activities were determined spectrophotometrically *in vitro*. According to the results, no significant activity was observed in hexane extract of *G. januensis* (Table 2).

Table 2. α -Glucosidase and α-amylase enzyme inhibition activities of *G. januensis*.

	α-Amylase Inhibitory Activity	α-Glucosidase Inhibitory Activity
Hexane extract of *G. januensis**	IC_{50} (µg/mL)	IC_{50} (µg/mL)
	> 400	> 400

*Values expressed herein are mean ± SEM of three parallel measurements, $p<0.05$.

This study is the first report on the antioxidant activitiy of the hexane extract of *G. januensis* and and on α-glucosidase and α-amylase enzyme inhibition.

Future research will be aimed at isolation of biologically active compounds such as flavonoids from *G. januensis*, as natural compounds for evaluation in pharmaceutical industry. Owing to their antioxidant activity they can benefit a good few disciplines.

REFERENCES

1. M. E. Grafakou, C. Barda, E. M. Tomou, H. Skaltsa, *Phytochemistry*, **181,** 112574 (2021).
2. F. Folli, D. Corradi, P. Fanti, A. Davalli, A. Paez, A. Giaccari, C. Perego, G. Muscogiuri, *Curr. Diabetes Rev*., **7,** 313 (2011).
3. A. P. Rauter, A. Martins, R. Lopes, J. Ferreira, L. M. Serralheiro, M. E. Araujo, C. Borges, J. Justino, F. V. Silva, M. Goulart, J. T. Oates, J. A. Rodrigues, E. Edwars, J. P. Noronha, R. Pinto, H. M. Filipe, *J. Ethno Pharm.*, **12,** 384 (2009).
4. T. Sabudak, H. Caliskan, H. H. Orak, M. Ozer, *Nat. Prod. Res.,* **35,** 1613 (2021).
5. J. S. Kim, C. S. Kwon, K. H. Son, *Biosci. Biotechnol. Biochem.*, **64,** 2458 (2010).
6. N. V. Quan, H. D. Tran, T. D. Xuan, A. Ahmad, T. D. Dat, T. D. Khanh, R. Teschke, *Molecules,* **24,** 482 (2019).
7. D. Hanganu, N.K. Olah, D. Benedec, A. Mocan, G. Crisan, L. Vlase, I. Popica, I. Oniga, *Pak. J. Pharm. Sci.,* **29,** 301 (2016).
8. N. Boubekri, Z. Belloum, R. Boukaabache, A. Amrani, N. Kahoul, W. Hamama, D. Zama, O. Boumaza, H. Bouriche, F. Benayache, S. Benayache, *Der Pharm. Lett.*, **6,** 1 (2014).

Stability investigation of PAA-BSA bioconjugate and PAA-Cu^{2+}-BSA ternary biocomplex at different pHs

B, Çakır[1], D, Şakar[1*], M, Karahan[2]

[1]Faculty of Arts and Sciences, Department of Chemistry, Yildiz Technical University, 34220 Esenler, Istanbul, Turkey
[2]Faculty of Health Science, Department of Nutrition and Dietetics, Uskudar University, Uskudar, Istanbul, Turkey

Polycomplexes containing polyelectrolyte (PE), metal and protein reveal strong immunogenecity and provide a high level of immunological protection. The solubility, composition, and stability of these polycomplexes depend on pH, metal/PE, and protein/PE ratios. Zetasizer parameters such as particle size, polydispersity, mobility and zeta potential are used to control the stability of solutions. These parameters are also very important for polyelectrolyte–protein binary conjugate and polyelectrolyte–metal-protein ternary complexes because of bioavailability, dissolution and immune toxicity of these complexes. Polyacrylic acid (PAA) is a polyanion polyelectrolyte and has been used in vaccine adjuvants due to its safety and lower toxicity. In the current study, PAA-BSA bioconjugate and PAA-Cu^{2+}-BSA ternary biocomplex were freshly synthesized according to two different procedures in the presence of acrylic acid (AA), copper (II) ions and bovine serum albumin (BSA). The stability of PAA-BSA bioconjugate and PAA-Cu^{2+}-BSA ternary biocomplex at different pHs was investigated by zetasizer measurements and the pH effect on the stability of PAA-BSA bioconjugate and PAA-Cu^{2+}-BSA ternary biocomplex was determined.

INTRODUCTION

Recently, synthetic polyelectrolytes (SPE) have been used quite frequently in biotechnological applications due to the enhancing immunoresponse to the immunizing antigen and provide an adjuvant effect. When SPEs are conjugated to microbial and viral antigens to obtain a stable complex, the immune response of the organism increases and provides immune protection. With this idea, artificial vaccines were started to be produced against infections that could not be controlled yet. SPEs can combine with antigen *via* metal (M) ion by means of activating the SPE surface. Thus, the synthetic vaccine model can be improved using SPE-M-protein ternary complexes. [1, 2] Polyanionic polymers have been used in vaccine adjuvants. Poly(acrylic acid) which is an effective adjuvant, is one of the linear polymers used as peptide carrier [3]. Poly(acrylic acid) is a polyanion in aquous solution and the structure of the PAA-M-protein ternary biocomplex is affected by pH and different salt concentrations [4]. Zetasizer measurements such as particle size, zeta potential give information about stability and charge of particles in solutions. Zeta potential parameter shows the degree of repulsion between the charged particles in the solution. High zeta potential values imply highly charged particles, which prevents aggregation of the particles due to electric repulsion. If the zeta potential is low, van der Waals attractive forces act upon particles and attraction between particles overcomes repulsion.

Thus, the particles in solution combine and aggregate. The zeta potential values bigger than −30 mV and +30 mV are accepted as optimum condition for good physical stabilization of solutions due to supplying sufficient repulsive force [5-8].

PAA-BSA bioconjugate and PAA-Cu^{+2}-BSA ternary biocomplex were freshly synthesized according to the method in reference [4]. The effect of different concentrations of NaCl salt on the stability of the PAA-BSA bioconjugate and the PAA-Cu^{2+}-BSA ternary biocomplex has been published [9]. In this study, the pH effect on the particle size, conductance, stability and charge of PAA-BSA bioconjugate and PAA-Cu^{2+}-BSA ternary biocomplex was examined.

EXPERIMENTAL

Materıals

Polyacrylic acid (Aldrich 523925), bovine serum albumin (BSA) (Sigma A 7030), copper sulfate (CuSO$_4$.5H$_2$0) (Merck 102788), 1-ethyl-3-(3-dimethylaminopropyl) carbodiimide hydrochloride (EDC) (Sigma) were used without any purification.

Preparation of BSA solution: BSA solution was prepared as 60 mg BSA/ 5 ml pure water. PAA- BSA bioconjugate was obtained by a conventional method.

Synthesis of PAA-BSA bioconjugate: Polyacrylic acid (1 mg) was dissolved in DMSO (0.1 ml) at room temperature and 1.9 mL of PBS solution was added to avoid micelle formation and to keep the organic

* To whom all correspondence should be sent:
E-mail: dsakar@yildiz.edu.tr

phase in total solution max 5%. EDC (4 mg) was added to this solution and the pH was adjusted to 4.7 at which is the highest EDC reactivity. After 3 h mixing of the solution, BSA was added to the reaction mixture (n BSA /n PAA : 2.0). Reaction pH was adjusted to 7 with 1 N NaOH and reaction mixture was stirred for 17 h.

Synthesis of PAA-Cu²⁺-BSA biocomplex (I method): PAA solution was prepared as 3mg/ml in PBS. CuSO₄.5H₂O solution was prepared in ultra pure water. BSA solution was prepared in PBS. PAA-Cu²⁺ bioconjugate was prepared with 3333 µl (9.999 mg) of PAA solution and CuSO₄.5H₂O. This solution was stirred overnight and pH was adjusted to 7 with NaOH solution. BSA solution was added to this bioconjugate solution and the PAA-Cu²⁺-BSA ternary biocomplex was obtained (blue colored solution, pH=7) ($n_{Cu^{2+}}/n_{PAA} = 0.4$; $n_{BSA} / n_{PAA} = 2$)

Synthesis of PAA-Cu²⁺-BSA biocomplex (II method): The pH of 3333 µl (9.999 mg) of PAA was adjusted to 6 and stirred overnight. BSA solution was slowly added to this solution and stirred overnight. After that, CuSO₄.5H₂O solution was added dropwise and the PAA-Cu²⁺-BSA ternary biocomplex was obtained (blue colored solution, pH 7)($n_{Cu^{2+}}/n_{PAA} = 0.4$; $n_{BSA} / n_{PAA} = 2$) (Scheme 1).

Zetasizer measurements

Zetasizer measurements of particle size, conductance, electrophoretic mobility and zeta potentials of BSA, PAA-BSA and PAA-Cu²⁺-BSA (I and II methods) at different pHs were performed *via* Brookhaven 90 Plus-Pals/BI-MAS (Multi Angle Particle Sizing) and zeta potential analyzer at 37ºC. The particle size and zeta potentials of BSA, PAA-BSA and PAA-Cu²⁺-BSA were obtained by calculating the average of 10 measurements.

RESULTS AND DISCUSSION

PAA-BSA binary bioconjugate and PAA-Cu²⁺-BSA ternary biocomplex were freshly prepared. The PAA-Cu²⁺-BSA ternary biocomplex changed color from blue to purple with changing pH (Fig. 1).

,
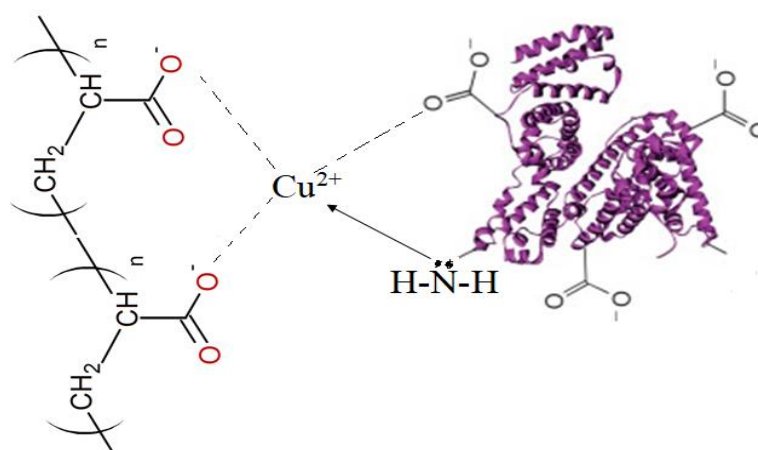
**Scheme 1.** Chemical structure of PAA-Cu²⁺-BSA ternary biocomplex
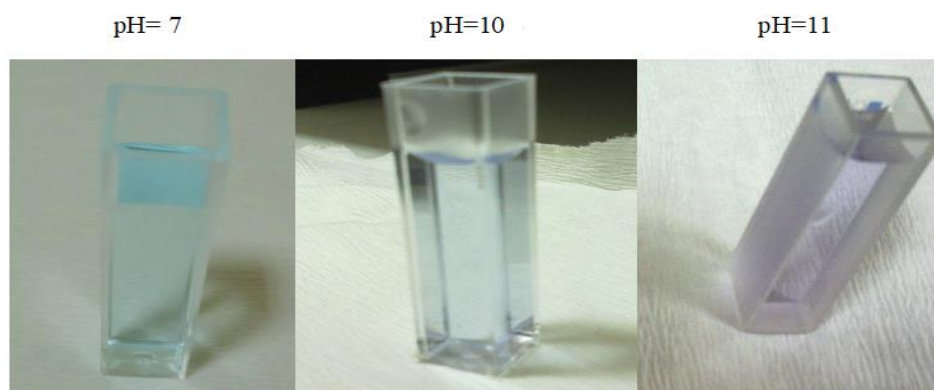
Fig. 1. Color change of PAA-Cu²⁺-BSA ternary biocomplex at different pHs

This color change shows that copper reacts with the protein. The color of the PAA- Cu^{2+}-BSA ternary biocomplex solution is blue between pH 7 and 9, this blue color converts to purple with increasing pH to 10 due to the biuret reaction between copper and protein [10].

The particle sizes of BSA, PAA-BSA and PAA-Cu^{2+}-BSA between pH 7 and 11 were measured by dynamic light scattering technique *via* a zetasizer. The results are shown in Table 1 and Fig. 2.

Table 1. Particle sizes (nm) of BSA, PAA-BSA binary bioconjugate and PAA- Cu^{2+}-BSA ternary biocomplex at different pHs

pH	BSA	PAA-BSA	PAA-Cu^{2+}-BSA	
			I Method	II Method
7	315	475	480	495
8	420	560	520	450
9	630	620	380	445
10	650	360	480	565
11	930	280	275	360
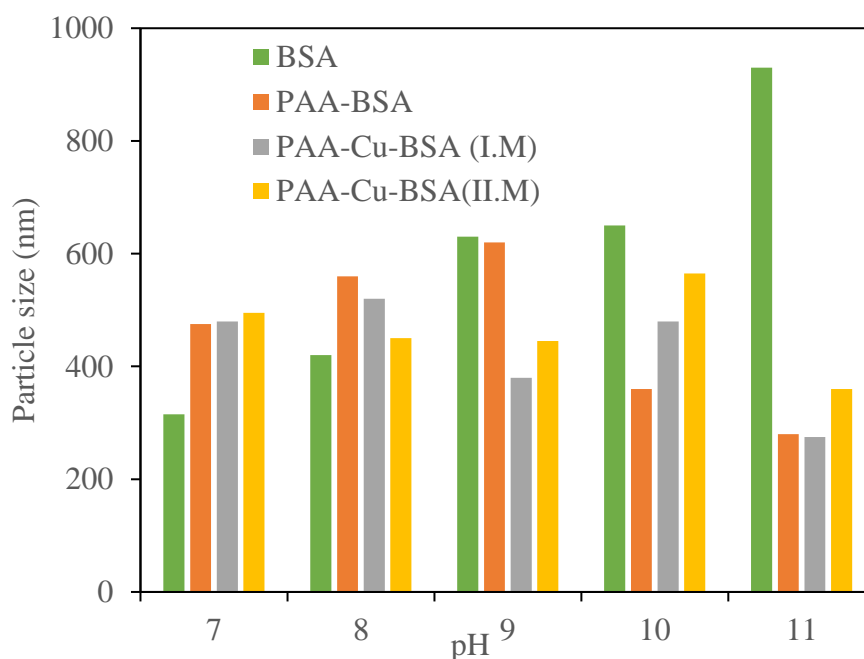
Fig. 2, Effect of pH on the particle size of BSA, PAA-BSA and PAA- Cu^{2+}-BSA (I and II M)

Table 2. Electrophoretic mobility (m^2/V.s) of BSA, PAA-BSA binary bioconjugate and PAA- Cu^{2+}-BSA ternary biocomplex at different pHs

pH	BSA	PAA-BSA	PAA-Cu^{2+}-BSA	
			I Method	II Method
7	-1.4	-2.1	-2.5	-2.9
8	-2.2	-2.6	-2.8	-2.9
9	-1.1	-2.0	-3.5	-2.1
10	-1.2	-2.6	-2.1	-2.8
11	-2.2	-2.7	-2.8	-2.7

Table 3. Zeta potentials (mV) of BSA, PAA-BSA binary bioconjugate and PAA-Cu^{2+}-BSA ternary biocomplex at different pHs

pH	BSA	PAA-BSA	PAA-Cu^{2+}-BSA	
			I Method	II Method
7	-21.7	-27.3	-31.7	-37.8
8	-28.6	-30.1	-36.4	-38.2
9	-14.8	-25.7	-30.6	-34.2
10	-18.3	-30.4	-34.8	-35.4
11	-28.0	-31.0	-35.8	-36.8
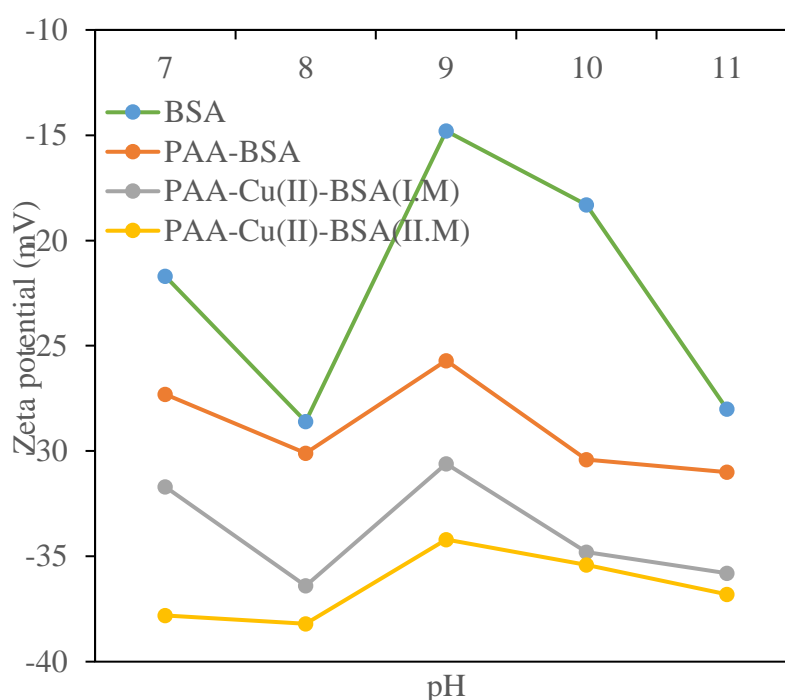
Fig. 3. Effect of pH on the zeta potentials (mV) of BSA, PAA-BSA and PAA- Cu^{2+}-BSA (I and II M)

Particle sizes of PAA-BSA and PAA- Cu^{2+}-BSA (I and II M), compared with BSA, increased at pH 7 and 8, but decreased in basic solutions. This trend suggests that the original closed structure of BSA is loosened after BSA binds with PAA and Cu ions at pH 7 and 8 while BSA structure shrinked between pH 9 and 11 [11].

The electrophoretic mobility and zeta potentials of BSA, PAA-BSA and PAA-Cu(II)-BSA between pH 7 and 11 were measured by phase analysis light scattering using a zetasizer. The results are given in Tables 2 and 3 and Fig. 3.

The electrophoretic mobility is proportional to zeta potential of solid particles in solution. Also, zeta potential indicates the surface charge property and stability of the solid particles in the solution. BSA protein contains many functionals such as amino group, carboxyl group and it can form complexes with polymers and metal ions and cause a change in surface charge.

It is noteworthy that the zeta potentials of BSA, PAA-BSA binary bioconjugate and PAA- Cu(II)-BSA ternary biocomplexes at different pHs were different. The zeta potential values of BSA were smaller than those of PAA-BSA and PAA-Cu^{2+}-BSA (I and II M) and all the samples had negative charge in the studied pH range. Comparing the stability of all samples, the most stable solution in the studied pH range was PAA-Cu^{2+}-BSA(II.M) The increase in negative zeta potential represents an electrostatic attraction between PAA-BSA and Cu(II) ions. The conductance of BSA, PAA-BSA and PAA-Cu^{2+}-BSA between pH 7 and 11 was measured by zetasizer. The results are given in Table 4 and Fig. 4.

Table 4. Conductance (µS) of BSA, PAA-BSA binary bioconjugate and PAA- Cu^{2+}-BSA ternary biocomplex at different pHs

pH	BSA	PAA-BSA	PAA-Cu^{2+}-BSA	
			I Method	II Method
7	440	6240	3330	2860
8	670	5830	4410	3300
9	1095	5580	3600	3065
10	2380	5210	3770	3450
11	9710	8400	7400	7090
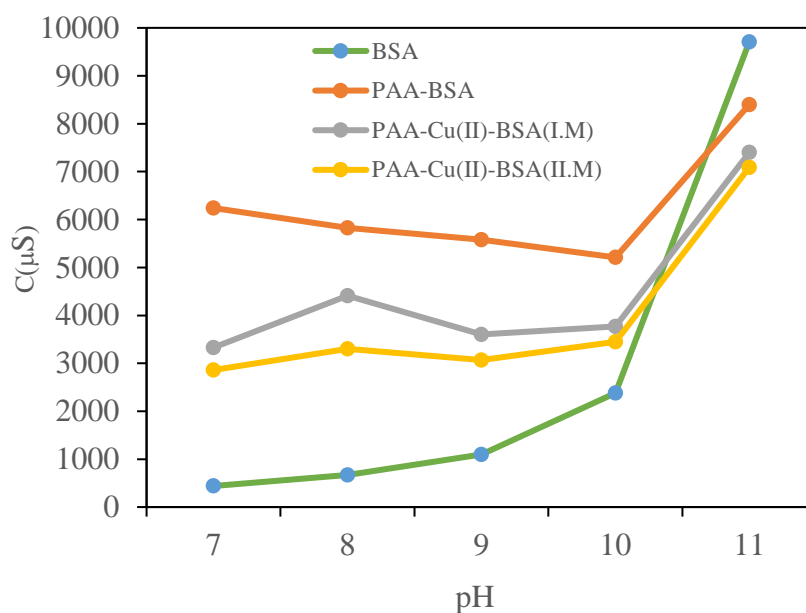
Fig. 4, Conductance change (µS) of BSA, PAA-BSA and PAA- Cu^{2+}-BSA (I and II M) as a function of pH

It was observed that the conductance of samples progressively increases with increasing pH. The conductance order of the samples was as follows: PAA-BSA> PAA-Cu^{2+}-BSA(I.M) > PAA- Cu^{2+}-BSA(II.M)>BSA. When the conductance of the samples was compared at increasing pH values, the highest conductance was registered for PAA-BSA. This increase in conductance of the PAA-BSA binary conjugate as a function of pH may be thought to be due to the exposure of more PAA ions with the solution.

CONCLUSION

In this study, PAA-BSA binary conjugate and PAA- Cu^{2+}-BSA ternary biocomplex were freshly synthesized according to two methods and their stability at different pHs was investigated *via* zetasizer measurements of particle size, zeta potential and conductance. The zeta potentials of BSA, PAA-BSA and PAA- Cu^{2+}-BSA (I and II M)

surfaces between pH 7 and 11 were at negative values and they preserved the stability at the studied pHs (zeta potentials >-30). According to the results, it was observed that the Cu metal ion had a reducing effect on the conductance of the biocomplexes. This was thought to be because the ternary structure was more stacked and stable in the presence of Cu metal, and PAA was all bound to BSA.

REFERENCES

1. A. Filenko, M. Demchenko, Z. Mustafaeva, Y. Osada, M. Mustafaev, *Biomacromolecules,* **2** (1), 270 (2001).
2. V. A. Kabanov, *Pure Appl. Chem.,* **76** (9), 1659 (2004).

3. M. Zhou, X. Li, Z. Wang, H. Zhou, X. Chen, S. Yang, Y. Li, *IOP Conf. Series: Materials Science and Engineering,* 772 (2020).
4. M. Karahan, Z. Mustafaeva, C. Ozeroglu, *Protein Journal*, **29**, 336 (2010).
5. R. J. Hunter, Zeta Potential in Colloid Science Principles and Applications, Applications of the Zeta Potential, Chapter 6, Academic Press, 1981, p. 219.
6. R. Shah, D. Eldridge, E. Palombo, I. Harding, *Journal of Physical Science*, **25** (1), 59 (2014).
7. S. Das, A. Chaudhury, *AAPS Pharmalogical Science and Technology,* **12** (1), 62 (2011).
8. C. Freitas, R. H. Müller, *International Journal of Pharmaceutics*, **168** (2), 221 (1998).
9. D. Sakar Dasdan, M. Karahan, F. Noyan Tekeli, G. Golbasi Simsek, *J. Indian Chemical Society*, **96**, 1195 (2019).
10. T. Peters, Jr., F. A. Blumenstock, *The Journal of Biological Chemistry*, **242** (7), 1574 (1967).
11. S. G. Yan, Y. He, G. Li, Y. Xiong, P. Song, R. M. Wang, *Journal of Chemical Science*, **128** (11), 1783 (2016).

Synthesis of zinc oxide nanoparticles using *Ficus thonningii* aqueous extract and evaluation of its anti-oxidant and anti-microbial activities

H. Umar[1,2*], D. Kavaz[1,2], A. L. Abubakar[3], M. R. Aliyu[1], N. Rizaner[1,2]

[1] *Bioengineering Department, Faculty of Engineering, Cyprus International University, Nicosia 98258, Via Mersin 10, Turkey*

[2] *Biotechnology Research Centre, Cyprus International University, Nicosia 99258, Via Mersin 10, Turkey*

[3] *Department of Biochemistry, Kano State University of Science and Technology, Wudil, Kano P.M.B 3244, Nigeria*

Zinc oxide nanoparticles (ZnO-NPs-AE) were synthesized using *Ficus thonningii* aqueous extract as an efficient stabilizing agent. Anti-microbial and anti-oxidant activity of the synthesized ZnO-NPs-AE were carried out using disc diffusion and DPPH (2,2-diphenyl-1-picryl-hydrazyl-hydrate) free radical method, respectively. Characterization of the synthesized ZnO-NPs-AE was achieved using UV-vis spectroscopy (UV-vis), Fourier-transform infrared spectroscopy (FTIR), X-ray diffraction (XRD), Scanning electron microscope (SEM), and energy-dispersive X-ray spectroscopy (EDX). Absorption peak in the range of 370 nm was observed using UV–vis following a color change from yellow to brown; both UV–Vis and FTIR spectra confirmed the formation of ZnO-NPs-AE, and SEM analysis result revealed spherical morphology with an average size of 18 nm. Anti-microbial analysis result of the biosynthesized ZnO-NPs-AE showed significant activity against *Escherichia coli* and *B. cereus* with lower concentrations. Moreover, the anti-oxidant activity result obtained using DPPH free radical scavenging method of the ZnO-NPs-AE revealed an IC_{50} value of 35 µg/mL. Biosynthesized ZnO-NPs-AE displayed anti-oxidant activity and anti-microbial potential against both gram-negative and gram-positive bacteria.

Keywords: Zinc oxide nanoparticles; Characterization; Antimicrobial; Antioxidant; *Ficus thonningii.*

INTRODUCTION

Nanotechnology is a rapidly expanding field of research that employs biosynthetic and environmentally friendly technology to create metallic oxide nanoparticles that are nontoxic, chemically stable, and biocompatible and could be used as drug carriers, anti-microbial, anti-oxidant, anticancer agents, and antidiabetics due to their novel physicochemical properties [1]. Among the recently studied nanoparticles, zinc oxide revealed specific properties that might be useful in biomedical engineering. Because of their hexagonal phase, n-type semiconductor, and wurtzite structure, ZnO NPs have recently attracted much attention [2]. Metal oxide NPs are synthesized using expensive and harmful physical and chemical techniques, with antagonistic compounds utilized as stabilizing agents [3]. Nanomaterials can be modified by replacing certain atoms, which improves the optical, mechanical, and electrical properties of materials by altering their chemical surface properties [4]. Zinc oxide is rapidly being used in personal care items including cosmetics and sunscreens due to its excellent UV absorption characteristics [5]. Furthermore, zinc is widely recognized as an essential trace element that can be found in all bodily tissues, including brain, muscles, bones, and skin

[2]. Apart from the biomedical application, zinc oxide can be utilized in a variety of different industries, such as concrete manufacture, photocatalysis, electronics, and electrotechnology [6]. Diarrhoea, urinary tract infections, diabetes mellitus, gonorrhea, respiratory infections, and mental problems are just a few of the diseases that *Ficus thonningii* is used to cure in African ethnomedicine [7]. *Ficus thonningii*, also known as the wild fig, is a multi-stemmed, evergreen or briefly deciduous tree with a dense, rounded to spreading crown that is primarily found in tropical and subtropical Africa's upland forests, at altitudes of 1,000–2,500 m, and thrives in light, deep, and well-drained soil [8]. The leaves are alternating or whorled, mid-dark green and sub-glossy above [9] and paler below, rounded or tapering, 4.5-12 cm long, hairless or finely hairy with a prominent midrib [10]. *Ficus thonningii* is a blooming tree that is pollinated by wasps who dwell in the syconium of its fruit in a symbiotic relationship. It is easily cultivated *via* seeds and cuttings [11].

The cost-effective green synthesis of ZnO-NPs-AE utilizing *Ficus thonningii* extract as a stabilizing agent is reported in this paper, as well as their characterization using several spectroscopic and microscopic techniques. Anti-oxidant potential of

* To whom all correspondence should be sent:
E-mail: humar@ciu.edu.tr

the synthesized ZnO-NPs-AE was studied using DPPH and anti-microbial activity using disc diffusion.

MATERIALS AND METHOD

Plant Materials

The stem bark of *Ficus thonningii* were obtained from Ajingi Local Government Area, Kano State, Nigeria and was authenticated at the Herbarium of the Department of Plant Biology, Bayero University Kano, Nigeria, and the specimen was given a voucher number BUKHAN 0110 and was deposited at the Herbarium of the institute.

Synthesis of Zinc Oxide Nanoparticles (ZnO NPs)

ZnO NPs using *Ficus thonningii* aqueous leaf extract were prepared using the method described by Huzaifa *et al.* with some minor modifications. Synthesis of ZnO NPs was carried out using $Zn(NO_3)_2 \cdot 6H_2O$ solutions in 90 mL of distilled water. *F. thonningii* extract (10 mL) was added dropwise to the mixture under constant stirring at 90°C for 8 hours and calcined for 3 hours at 300 ±10°C in a muffle furnace.

Characterization

The UV-vis spectrum of synthesized ZnO-NPs-AE was evaluated using a UV-vis spectrophotometer (Shimadzu UV-2450) to confirm the synthesis of the nanoparticles in a wavelength range between 300 and 800 nm at room temperature. Functional groups attached to the synthesized ZnO-NPs-AE were evaluated using Fourier transform infrared (FTIR) spectrometer at 4 cm^{-1} resolution and a frequency range of 4000–400 cm^{-1}. Crystalline structure of a powdered ZnO-NPs-AE sample was determined using a X-ray diffractometer (Rigaku ZSX Primus II) with CuKα radiation. Morphology of the synthesized ZnO NPs was determined using a scanning electron microscope (JOEL JSM 6335-F) with 150 kV acceleration voltage, and energy-dispersive X-ray spectroscopy (EDS Oxford Instruments AZTEC EDS).
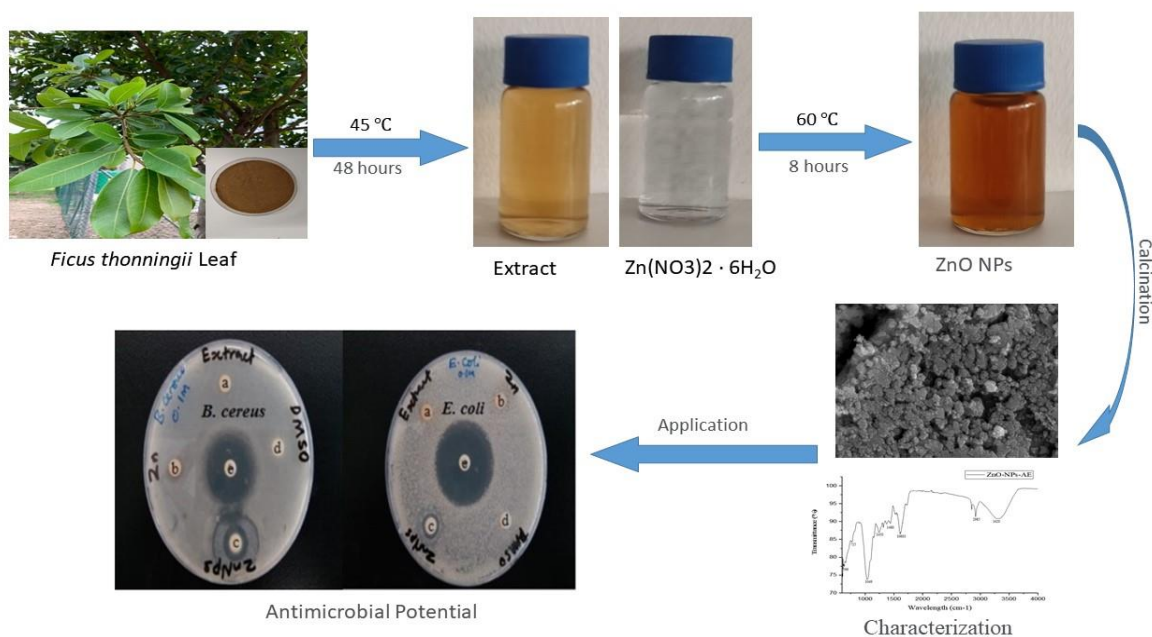
Figure 1. Overview of the synthesis of ZnO-NPs-AE, characterization and anti-microbial activity.

DPPH free radical scavenging activity

Blios (1958) method with minor modifications was utilized to determine the scavenging activity of synthesized ZnO-NPs and *Ficus thonningii* extracts using the 2,2-diphenyl-1-picryl hydrazyl (DPPH) free radical scavenging assay [12]. Different concentrations of *Ficus thonningii* extracts prepared in methanol (200, 150, 100, 75, 50, 37.5, 25, 17.5 g/mL) were combined with 3.0 mL of DPPH and incubated for 20 minutes at room temperature. The extracts' absorbance was measured at 517 nm using a UV-vis spectrophotometer and compared to that of a control sample (ascorbic acid).

The inhibition % of DPPH radical scavenging activity was estimated using the following equation:

DPPH free radicals (%) Ac $= (As/Ac)$ (1)

where the absorbance of the control is Ac, and the absorbance of the standard or sample is As.

The IC_{50} value was calculated as the sample concentration required to scavenge 50% of DPPH free radicals.

Experiments were done in triplicate, and the results were provided as mean ± standard deviation.

Anti-microbial activity

Anti-microbial activity of the sythesized ZnO-NPs-AE and *Ficus thonningii* extracts was determined on Muller Hinton agar using the method of Jorgensen and Turnidge (2015) with some modifications [13]. Inhibition zones were measured after incubation, and results were interpreted in accordance with the Clinical and Laboratory Standards Institute (CLSI) protocol, (2007), for anti-microbial testing. Experiments were done in triplicate and the results were provided as mean ± standard deviation.

Statistical Analysis

Data are given as means ± standard errors of the mean (SEMs). Statistical comparisons were performed using unpaired Student's t-test, ANOVA followed by Newman-Keuls *post hoc* analysis, where necessary using IBM SPSS Statistics version 21. All experiments were carried out in triplicate (*n* = 3). P < 0.05 was considered significant or P > 0.05 insignificant and P < 0.0001 was considered highly significant.

RESULTS

ZnO-NPs-AE were synthesized from zinc nitrate solution using *Ficus thonningii* leaves aqueous extract as a stabilizing agent. The synthesis was confirmed and characterized using various spectroscopic and microscopic techniques.

ZnO-NPs-AE were confirmed using UV-Vis spectroscopic technique due to the rapid color formation from yellow to dark brown as a result of surface plasmon vibration (Figure 1). The UV-vis spectrum of the synthesized ZnO-NPs-AE revealed an absorption peak at 370 nm in agreement with zinc oxide nanoparticle's absorption peak range (360-380) as reported by [14].

FTIR analysis was conducted at room temperature in a frequency range between 4,500 and 400 cm^{-1} and the result revealed the composition of bioactive molecules of *Ficus thonningii* and their distribution on the surface of the synthesized ZnO-NPs-AE. Broad absorption bands at 3420 cm^{-1} are associated with O-H bond from the water that was absorbed during the synthesis. In addition, bands were seen at 1450 and 1049 cm^{-1}, corresponding to C=CH stretching of methyl group and C=O of saturated alcohol, respectively. Presence of alcohol and methyl group is among the characteristics of the NPs ability to bind to metals which could prevent agglomeration [15].
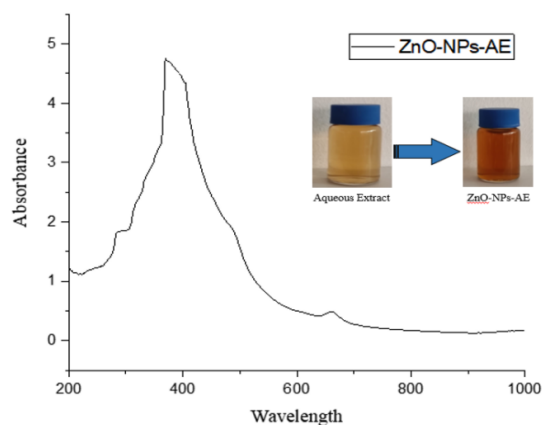

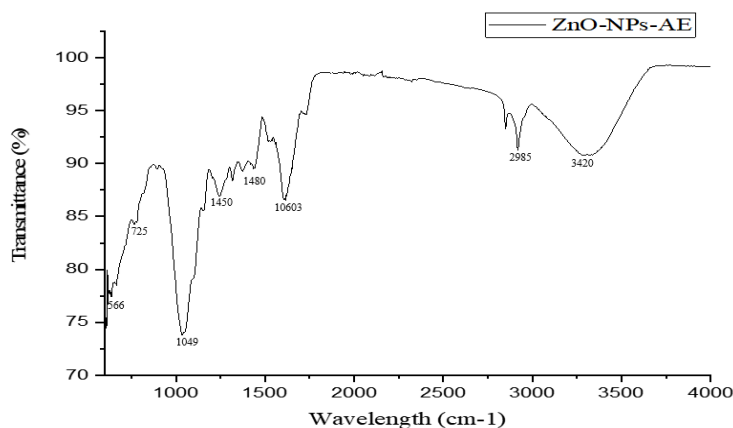**Figure 2.** UV–visible spectrum of the synthesized ZnO-NPs-AE

Figure 3. FTIR spectrum of the synthesized ZnO-NPs-AE

XRD pattern of the synthesized ZnO-NPs-AE revealed the various phase purity of the nanoparticles as shown in Fig. 4. Broad peaks obtained are 100, 002, 101, 102, 110, 103, 112, 004, and 104 corresponding to Bragg reflections with 2θ values of 31.70°, 34.34°, 36.16°, 47.54°, 56.48°, 62.78°, 67.66°, 72.53°, and 76.58°, respectively. In addition, this confirms the presence of purified ZnO-NPs. Nanostructures can be observed and confirmed from XRD pattern of the particles, and the patterns observed in our particles confirmed the crystalline structure of the particles [16].

SEM analysis of the synthesized ZnO-NPs-AE revealed agglomerated particles with sharp spherical morphology and average size of 18 nm which could be responsible for the stability and biomedical potential of the NPs (Figure 5). Studies have reported that the size of NPs plays an important role in the the properties of these nanoparticles and it could lead to change in the potential of the synthesized nanoparticles [17].

EDX spectra showed the surface chemical composition of the synthesized ZnO-NPs-AE. Various signals oe Zn and of oxygen appeared on the surface of the synthesized ZnO-NPs-AE, and the appearance of C, P, and Na also confirmed the plant extract's interference in the particle synthesis.

In vitro anti-oxidant potential of *Ficus thonningii*, ZnO-NPs-AE, and ascorbic acid (control) was determined. The result revealed the increased anti-oxidant potential of ZnO-NPs-AE when compared with the plant extract (Figure 6). The synthesized zinc oxide revealed an IC_{50} value of 35 µg/mL which is close to that of ascorbic acid with IC_{50} of 8 µg/mL. It has been observed that enzymes that use the metal ion (Zn) as a co-factor scavenge H_2O_2 free radicals and that the presence of Zn ion in the particles may be responsible for more vital H_2O_2 free radical scavenging activity than the plant [18]. In addition, phenolic chemicals found in plant extracts have consistently high anti-oxidant activity and play a vital role in the green manufacturing of nanoparticles [19].
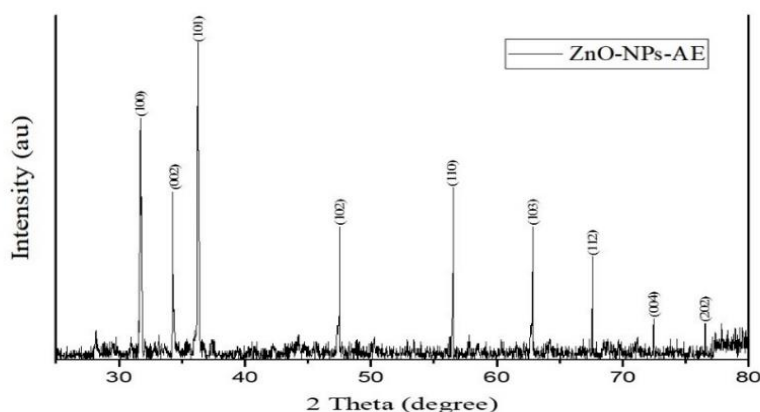

Figure 4. XRD pattern of the synthesized ZnO-NPs-AE
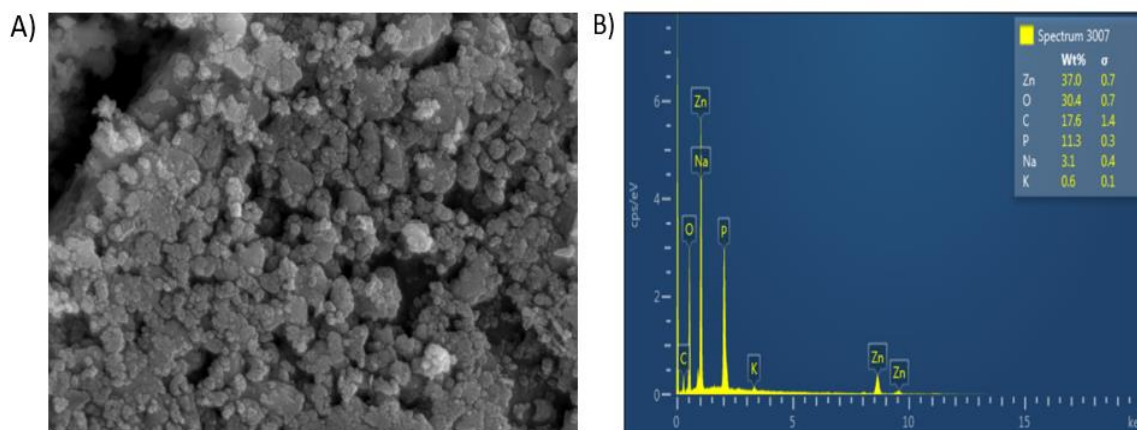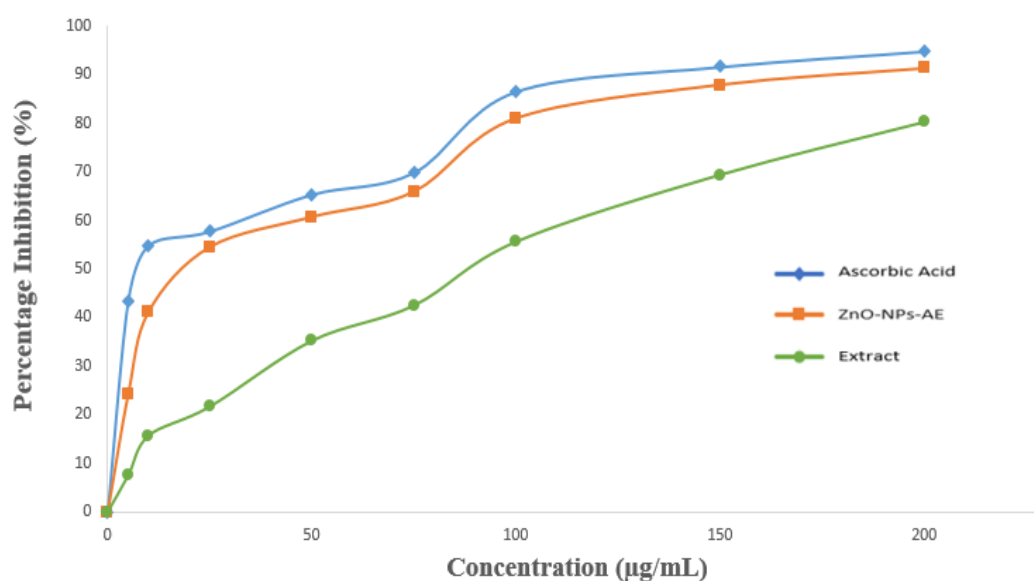

Figure 5. (A) SEM image of the synthesized ZnO-NPs-AE; (B) EDX spectrum of the synthesized ZnO-NPs-AE

Figure 6. DPPH free radical scavenging potential of the various concentrations of the synthesized ZnO-NPs-AE, *Ficus thonningii* extract, and ascorbic acid. Data are presented as mean ± SD of at least three replicates ($n \geq 3$).

The results of the anti-microbial activities of the synthesized ZnO-NPs-AE evaluated using the disc diffusion method against *Escherichia coli,* and *Bacillus cereus* revealed highly significant differences when compared with the control group (ciprofloxacin) and the plant extract ($P < 0.05$; $n \geq 3$; Table 1). The change in the anti-microbial potential of the synthesized ZnO-NPs-AE might result from increased stability and reactivity of the particles. When the particle size of ZnO is lowered to the nanometer range, it can interact with the bacterial surface or the bacterial core, where it enters the cell and exhibits unique bactericidal properties [20]. The anti-microbial activity revealed by the synthesized ZnO-NPs-AE conforms with several studies.

Table 1. Anti-microbial activity of synthesized ZnO-NPs-AE

	Zone of Inhibition (mm)	
Organism	*Escherichia coli*	*Bacillus cereus*
Standard ciprofloxacin (10 ug/disc)	11.33 ± 0.29	13.00 ± 1.00
Ficus thonningii extract	1.33 ± 0.58***	2.67 ± 0.58***
ZnO-NPs-AE	2.00 ± 0.50***	3.67 ± 0.58***

CONCLUSION

Overall, stable ZnO-NPs-AE were synthesized *via* the green route using *Ficus thonningii* as a stabilizing agent. Following characterization of the synthesized nanoparticles, FTIR research indicated that the extract functions as a reducing and stabilizing agent. An absorption peak in the region of 370 nm and agglomerated spherical morphology with an average size of 18 nm was discovered using UV–vis spectroscopy. Anti-oxidant and anti-microbial analysis results of the synthesized ZnO-NPs-AE revealed IC$_{50}$ values of 35 µg/mL and strong anti-microbial potential.

REFERENCES

1. V. P. Nguyen, Y. Li, J. Henry, T. Qian, W. Zhang, X. Wang, Y. M. Paulus, *Methods in Enzymology*, **657**, 443 (2021), doi: 10.1016/BS.MIE.2021.06.038.
2. V. G. L. Souza, C. Rodrigues, S. Valente, C. Pimenta, J. R. A. Pires, M. M. Alves, C. F. Santos, I. M. Coelhoso, A. L. Fernando, *Coatings, 10,* 110 (2020). https://doi.org/10.3390/coatings10020110
3. M. Gupta, S. Tomar Rajesh, K. K. Shuchi, M. Raghvendra, S. Divakar, *Frontiers in Microbiology*, **9,** 231 (2018), doi: 10.3389/fmicb.2018.02030.
4. D. Kavaz, H. Umar, S. Shehu, *Artificial Cells, Nanomedicine and Biotechnology*, **46** (3), S1193 (2018) doi: 10.1080/21691401.2018.1536060.
5. R. M. El-Gharbawy, A. M. Emara, S. E. S. Abu-Risha, *Biomedicine and Pharmacotherapy*, **84**, 810 (2016), doi: 10.1016/j.biopha. 2016.09.068.
6. H. J. Paek, Y. J. Lee, H. E. Chung, J. A Lee, M. K. Kim, J. Jeong, S. J. Choi. *Nanoscale*, **5**, 11416 (2013), doi: 10.1039/c3nr02140h.
7. R. Dangarembizi, K. H. Erlwanger, D. Moyo, E. Chivandi, *Afr. J. Tradit. Complement. Altern. Med.*, **10** (2), 203 (2012), doi: 10.4314/ajtcam.v10i2.4. PMID: 24146443; PMCID: PMC3746567.
8. P. Danthu, P. Solovier, A. Gaye, A. Sarr, M. Seck, I. Thomas, *Agrofor. Syst.*, **55**, 57 (2002).
9. G. N. Njoronge, J. W. Kibunga, *Afr. J. Ecol.*, **45**, 65 (2007).

10. D. Cousins, M. A. Huffman, *Afr. Study Monogr.,* **23**, 65 (2002).
11. S. Bah, D. Diallo, B. Dembele, S. Paulsen, *J. Ethnopharmacol.*, **105**, 387 (2006).
12. M. S. Blios, *Nature*, 1199 (1958).
13. H. Jorgensen, J. D. Turnidge, Manual of Clinical Microbiology, 11th edn., American Society of Microbiology, 2015, p. 1253.
14. N. Padmavathy, R. Vijayaraghavan, *Science and Technology of Advanced Materials*, **9**(3), 263 (2008) doi: 10.1088/1468-6996/9/3/035004.
15. H. Umar, D. Kavaz, N. Rizaner, *International Journal of Nanomedicine*, **14**, 87 (2019), doi: 10.2147/IJN.S186888.
16. D. Kavaz, H. Umar, T. Zimuto, *Hacettepe Journal of Biology and Chemistry,* **47** (4), 367 (2019), doi: 10.15671/hjbc.518593.
17. S. Sadhasivam, P. Shanmugam, K. S. Yun, *Colloids and Surfaces B: Biointerfaces,* **81** (1), 358 (2010), doi: 10.1016/j.colsurfb.2010.07.036.
18. Z. U. H. Khan, A. Khan, Y. Chen, N. S. Shah, N. Muhammad, A. U. Khan, K. T. Khan, S. A. Qaisarani, P. Wan, *Journal of Photochemistry and Photobiology B: Biology*, **173**, 150 (2017), doi: 10.1016/j.jphotobiol.2017.05.034.
19. H. R. Madan, S. C. Sharma, D. Suresh, Y. S. Vidya, H. Nagabhushana, H. Rajanaik, K. S. Anantharaju, S. C. Prashantha, P. Sadananda Maiya, *Spectrochimica Acta - Part A: Molecular and Biomolecular Spectroscopy*, **152**, 404 (2016), doi: 10.1016/j.saa.2015.07.067.
20. N. Wang, J. Y. H. Fuh, S. T. Dheen, A. S. Kumar, *Journal of Biomedical Materials Research - Part B Applied Biomaterials,* **109** (2), 1609 (2021), doi: 10.1002/jbm.b.34688.

BULGARIAN CHEMICAL COMMUNICATIONS

Instructions about Preparation of Manuscripts

General remarks: Manuscripts are submitted in English by e-mail or by mail (in duplicate). The text must be typed double-spaced, on A4 format paper using Times New Roman font size 12, normal character spacing. The manuscript should not exceed 15 pages (about 3500 words), including photographs, tables, drawings, formulae, etc. Authors are requested to use margins of 3 cm on all sides. For mail submission hard copies, made by a clearly legible duplication process, are requested. Manuscripts should be subdivided into labelled sections, e.g. **Introduction, Experimental, Results and Discussion**, *etc*.

The title page comprises headline, author's names and affiliations, abstract and key words.

Attention is drawn to the following:

a) **The title** of the manuscript should reflect concisely the purpose and findings of the work. Abbreviations, symbols, chemical formulas, references and footnotes should be avoided. If indispensable, abbreviations and formulas should be given in parentheses immediately after the respective full form.

b) **The author**'s first and middle name initials, and family name in full should be given, followed by the address (or addresses) of the contributing laboratory (laboratories). **The affiliation** of the author(s) should be listed in detail (no abbreviations!). The author to whom correspondence and/or inquiries should be sent should be indicated by asterisk (*).

The abstract should be self-explanatory and intelligible without any references to the text and containing not more than 250 words. It should be followed by key words (not more than six).

References should be numbered sequentially in the order, in which they are cited in the text. The numbers in the text should be enclosed in brackets [2], [5, 6], [9−12], etc., set on the text line. References, typed with double spacing, are to be listed in numerical order on a separate sheet. All references are to be given in Latin letters. The names of the authors are given without inversion. Titles of journals must be abbreviated according to Chemical Abstracts and given in italics, the volume is typed in bold, the initial page is given and the year in parentheses. Attention is drawn to the following conventions:

a) The names of all authors of a certain publications should be given. The use of "*et al*." in the list of references is not acceptable.

b) Only the initials of the first and middle names should be given.

In the manuscripts, the reference to author(s) of cited works should be made without giving initials, e.g. "Bush and Smith [7] pioneered...". If the reference carries the names of three or more authors it should be quoted as "Bush *et al*. [7]", if Bush is the first author, or as "Bush and co-workers [7]", if Bush is the senior author.

Footnotes should be reduced to a minimum. Each footnote should be typed double-spaced at the bottom of the page, on which its subject is first mentioned.

Tables are numbered with Arabic numerals on the left-hand top. Each table should be referred to in the text. Column headings should be as short as possible but they must define units unambiguously. The units are to be separated from the preceding symbols by a comma or brackets.

Note: The following format should be used when figures, equations, *etc*. are referred to the text (followed by the respective numbers): Fig., Eqns., Table, Scheme.

Schemes and figures. Each manuscript (hard copy) should contain or be accompanied by the respective illustrative material as well as by the respective figure captions in a separate file (sheet). As far as presentation of units is concerned, SI units are to be used. However, some non-SI units are also acceptable, such as °C, ml, l, etc.

The author(s) name(s), the title of the manuscript, the number of drawings, photographs, diagrams, etc., should be written in black pencil on the back of the illustrative material (hard copies) in accordance with the list enclosed. Avoid using more than 6 (12 for reviews, respectively) figures in the manuscript. Since most of the illustrative materials are to be presented as 8-cm wide pictures, attention should be paid that all axis titles, numerals, legend(s) and texts are legible.

The authors are asked to submit **the final text** (after the manuscript has been accepted for publication) in electronic form either by e-mail or mail on a 3.5'' diskette (CD) using a PC Word-processor. The main text, list of references, tables and figure captions should be saved in separate files (as *.rtf or *.doc) with clearly identifiable file names. It is essential that the name and version of

the word-processing program and the format of the text files is clearly indicated. It is recommended that the pictures are presented in *.tif, *.jpg, *.cdr or *.bmp format, the equations are written using "Equation Editor" and chemical reaction schemes are written using ISIS Draw or ChemDraw programme.

The authors are required to submit the final text with a list of three individuals and their e-mail addresses that can be considered by the Editors as potential reviewers. Please, note that the reviewers should be outside the authors' own institution or organization. The Editorial Board of the journal is not obliged to accept these proposals.

EXAMPLES FOR PRESENTATION OF REFERENCES

REFERENCES

1. D. S. Newsome, *Catal. Rev.–Sci. Eng.*, **21**, 275 (1980).
2. C.-H. Lin, C.-Y. Hsu, *J. Chem. Soc. Chem. Commun.*, 1479 (1992).
3. R. G. Parr, W. Yang, Density Functional Theory of Atoms and Molecules, Oxford Univ. Press, New York, 1989.
4. V. Ponec, G. C. Bond, Catalysis by Metals and Alloys (Stud. Surf. Sci. Catal., vol. 95), Elsevier, Amsterdam, 1995.
5. G. Kadinov, S. Todorova, A. Palazov, in: New Frontiers in Catalysis (Proc. 10th Int. Congr. Catal., Budapest, 1992), L. Guczi, F. Solymosi, P. Tetenyi (eds.), Akademiai Kiado, Budapest, 1993, Part C, p. 2817.
6. G. L. C. Maire, F. Garin, in: Catalysis. Science and Technology, J. R. Anderson, M. Boudart (eds), vol. 6, Springer-Verlag, Berlin, 1984, p. 161.
7. D. Pocknell, *GB Patent* 2 207 355 (1949).
8. G. Angelov, PhD Thesis, UCTM, Sofia, 2001.
9. JCPDS International Center for Diffraction Data, Power Diffraction File, Swarthmore, PA, 1991.
10. CA **127**, 184 762q (1998).
11. P. Hou, H. Wise, *J. Catal.*, in press.
12. M. Sinev, private communication.
13. http://www.chemweb.com/alchem/articles/1051611477211.html.

CONTENTS